DISSERTATION

DAMPING AND SWITCHING IN THIN FILMS AND HETERO-STRUCTURES OF MAGNETIC MATERIALS AND TOPOLOGICAL MATERIALS

Submitted by

Jinjun Ding

Department of Physics

In partial fulfillment of the requirements

For the Degree of Doctor of Philosophy

Colorado State University

Fort Collins, Colorado

Fall 2020

Doctoral Committee:

Advisor: Mingzhong Wu

Robert Camley
Stuart Field
Jacob Roberts
Matthew Shores

ABSTRACT

DAMPING AND SWITCHING IN THIN FILMS AND HETERO-STRUCTURES OF MAGNETIC MATERIALS AND TOPOLOGICAL MATERIALS

Yttrium iron garnet ($Y_3Fe_5O_{12}$, YIG) materials have been widely used in microwave devices and have also shown high potential for magnonics and spintronics applications. This is because the fact that YIG materials have very low intrinsic damping and is electric insulating. The development of YIG-based spintronics demands YIG films that have a thickness in the nanometer (nm) range and at the same time exhibit low damping comparable to single-crystal YIG bulk materials. In this dissertation, the demonstration of using magnetron sputtering to grow high-quality polycrystalline nm-thick YIG films on gadolinium gallium garnet ($Gd_3Ga_5O_{12}$, GGG) substrates is discussed in detail, which is of great technological significance as well as scientific research. The damping constant of the YIG films is the lowest among all the previous reports of nm-thick YIG films grown. Such demonstration of high-quality nm-thick YIG films proves the possibility of nanoscale patterning of YIG films and the future development of YIG-based nanoscale devices. Further, YIG thin films having a thickness of several nanometers and showing both strong perpendicular magnetic anisotropy (PMA) and low magnetic damping are realized in this dissertation.

The phenomenon of spin pumping refers to the transfer of spins from precessional moments in a ferromagnet to a non-magnetic material. In a ferromagnetic/non-magnetic bi-layered system, spin pumping manifests itself as two distinct effects: (1) an enhancement in the damping in the ferromagnetic layer and (2) a pure spin current in the non-magnetic layer. This dissertation

studies spin pumping effects in a ferromagnetic NiFe thin film associated with topological surface states (TSS) in a neighboring topological Dirac semimetal α-Sn thin film. Large damping enhancement due to the TSS of the Dirac semimetal α-Sn thin film is observed. Moreover, the spin current generated in the α-Sn film was utilized to switch a magnet through spin-orbit torque (SOT). The switching efficiency is comparable to that in topological insulators, which paves the way for the application of α-Sn thin films in future SOT-based magnetic memory.

When a topological insulator (TI) is interfaced with a magnetic insulator (MI), it may host the anomalous Hall effect (AHE) and the quantum AHE associated with Berry-phase curvature in momentum space. This dissertation reports a *bona fide* topological Hall effect (THE) in a single magnetic phase TI/MI heterostructure ($Bi_2Se_3/BaFe_{12}O_{19}$) where the electrical transport is exclusively confined to the TI layer. Experimental observations are consistent with a THE originating from skyrmions in $BaFe_{12}O_{19}$ that are formed due to interfacial Dzyaloshinskii–Moriya interaction.

ACKNOWLEDGEMENTS

I would like to thank my advisor, Professor Mingzhong Wu, for his inspiration, advice, and guidance throughout my Ph.D. program. He was always available, despite his busy schedule, to share his wisdom on anything from research to writing. This dissertation would not have been possible without his guidance and help.

I would like to thank Dr. Carl Patton and Dr. Boris Kalinikos for their sage advices on microwave and magnetism. I am grateful to Professor Kristen Buchanan, Professor Jose de la Venta and Professor Dylan Yost for valuable suggestions on the MOKE system. Thanks to Professor Stuart Field for providing insights in photolithography and Professor Hua Chen and Professor Jifa Tian for discussions on topological materials. My appreciation also extends to Robert Adame for his generous help at the machine shop. I would like to acknowledge the members of my dissertation committee for offering their time, support, and guidance throughout my research and review of this dissertation.

I am also grateful to all the colleagues I have had the pleasure to work with: Dr. Peng Li, Dr. Tao Liu, Dr. Chuanpu Liu, Dr. Vijaysankar Kalappattil, Dr. Rui Yu, Dr. Gen Yin, Dr. David Ellsworth, Dr. Praveen Janantha, Dr. Daniel Richardson, Dr. Houchen Chang, Dr. Josh Lauzier, Dr. August DeMann, Logan Sutton, Yuejie Zhang, Uppalaiah Erugu, Mike Ross, Weston Maughan, Adam Brandt, and Cory Rasor.

Lastly, I would owe my deepest thanks to my family for their unconditional love and support. Without their support, I would not be able complete my Ph.D. program.

TABLE OF CONTENTS

CHAPTER 1 OVERVIEW

1.1 Background and motivations

Yttrium iron garnet ($Y_3Fe_5O_{12}$, YIG) materials have been widely used in microwave devices and have also shown high potential for magnonics and spintronics applications.[1,2,3,4,5,6,7,8] This is because the fact that YIG materials have very low intrinsic damping[9] and are electrically insulating. The development of YIG-based spintronics demands YIG films that have a thickness in the nanometer (nm) range and at the same time exhibit low damping comparable to single-crystal YIG bulk materials. Previous work demonstrated pulsed laser deposition (PLD) of YIG thin films with relatively low damping.[10] 20-nm-thick PLD YIG films, for example, showed a Gilbert damping constant of $\alpha = 0.00023$, which is relatively low.[10] However, there are obstacles for PLD techniques to be applied to industry. These obstacles include small wafer deposition, low repeatability, instability of the system control, and so on. Magnetron sputtering as a physical vapor deposition (PVD) technique, on the other hand, is most widely used in industry such as Western Digital, Seagate Technology, Samsung Semiconductors Inc., and so on. It enables the production of large-size wafers with uniform properties. Other advantages of sputtering include convenient control of deposition parameters, high repeatability, and fast production. In this dissertation, the use of magnetron sputtering to grow high-quality polycrystalline nm-thick YIG films on gadolinium gallium garnet ($Gd_3Ga_5O_{12}$, GGG) substrates is explored in detail, which is of great technological significance for industrialization as well as scientific research. The GGG substrates are chosen because the lattice constant is very similar to that of YIG. The damping constant of the YIG films is the lowest among all the previous reports of nm-thick YIG films

grown by magnetron sputtering.[11] Such demonstration of high-quality nm-thick YIG films proves the possibility of nanoscale patterning of YIG films[12,13] and the future development of YIG-based nanoscale devices. Moreover, YIG thin films having a thickness of several nanometers and showing both strong perpendicular magnetic anisotropy (PMA) and low magnetic damping are realized in this dissertation.[14]

The phenomenon of spin pumping refers to the transfer of spins from precessional moments in a ferromagnet to a non-magnetic material.[15,16,17] In a ferromagnetic/non-magnetic bi-layered system, spin pumping manifests itself as two distinct effects: (1) an enhancement in the damping in the ferromagnetic layer and (2) a pure spin current in the non-magnetic layer. This dissertation studies spin pumping effects in a ferromagnetic NiFe thin film associated with topological surface states (TSS) in a neighboring topological Dirac semimetal α-Sn thin film.[18] It's found that the TSS in the layered structures can cause an extra damping that is more than 3 times bigger than the damping in the bare NiFe film. Such a large damping enhancement is not present in structures where the α-Sn film interfaces directly with the NiFe film and the TSS are thereby suppressed, or where the Sn film is a topologically trivial material. Moreover, the spin current generated in an α-Sn film is utilized to switch a magnet through spin-orbit torque (SOT).[19] The switching is mainly enabled by the TSS of the α-Sn, rather than spin-orbit coupling in the bulk of the α-Sn or electric current-produced heating effects. The switching efficiency is comparable to that in topological insulators.

When a topological insulator (TI) is interfaced with a magnetic insulator (MI), it may host the anomalous Hall effect (AHE) and the quantum AHE associated with Berry-phase curvature in momentum space. Such heterostructures can also display transport signatures consistent with a topological Hall effect (THE) arising from real-space Berry-phase curvature. However, a recent

study suggests that this behavior may arise from two coexisting magnetic phases, rather than a genuine THE.[20] This dissertation reports a *bona fide* THE in a single magnetic phase TI/MI heterostructure ($Bi_2Se_3/BaFe_{12}O_{19}$) wherein the electrical transport is exclusively confined to the TI layer. Experimental observations are consistent with a THE originating from skyrmions in the $BaFe_{12}O_{19}$ film that are formed due to interfacial Dzyaloshinskii–Moriya interaction (DMI).

1.2 Dissertation organization

This dissertation presents high-quality nm-thick yttrium iron garnet film development on gadolinium gallium garnet insulator substrates as well as substituted gadolinium gallium garnet insulator substrates through magnetron sputtering techniques. The spin current-to-charge current conversion in topological Dirac semimetal α-Sn films has been investigated through spin pumping effects. Room temperature magnetization switching utilizing topological surface states of α-Sn films grown on Si substrates were demonstrated. Topological Hall effect in magnetic insulator/topological insulator heterostructure was studied through electrical transport measurements.

Chapter 2 introduces the basics of magnetron sputtering techniques, including the mechanisms of plasma generation, the sputtering process, thin film formation, and the argon ion etching process. Some measurement techniques that are frequently mentioned in the following chapters are also discussed briefly.

Chapter 3 presents an introduction of topological materials including topological insulators and topological Dirac semimetals. Details about the crystal structure and electronic structure of α-Sn thin films under strain are discussed.

Chapter 4 reports the growth and magnetic properties of low-damping nm-thick YIG films by magnetron sputtering. Details on the sputtering and annealing optimization process, the

dependence of YIG film properties on annealing temperatures, and the magnetic properties of YIG thin films are discussed.

Chapter 5 presents nm-thick YIG thin films with both perpendicular magnetic anisotropy (PMA) and low damping. The static and dynamic magnetic properties of PMA YIG films are presented, and the origin of PMA are discussed in detail. SOT switching of PMA YIG films is studied as a demonstration of the application of the PMA YIG films on fundamental studies in spintronics.

Chapter 6 reports the study of spin pumping in a ferromagnetic thin film associated with TSS in a neighboring Dirac semimetal α-Sn thin film. The dynamic properties of NiFe/α-Sn heterostructures are studied and the TSS of Dirac semimetal α-Sn films are discussed.

Chapter 7 presents current-induced switching in a rectangular structure consisting of a 6-nm-thick film of topological Dirac semimetal α-Sn, a 2-nm-thick ferromagnetic CoFeB film, and a 2-nm-thick Ag spacer in-between the two films. Electric transport properties of topological Dirac semimetal α-Sn, the mechanism of switching, and the switching efficiency are discussed in detail.

Chapter 8 reports the observation of THE responses in a bi-layered structure that consists of a topological insulator Bi_2Se_3 thin film grown on top of a magnetic insulator $BaFe_{12}O_{19}$ thin film. Details about growth of $BaFe_{12}O_{19}$ thin films, temperature dependence of the THE, calculation of THE phase diagrams are discussed.

Chapter 9 includes a summary of the whole dissertation and the outlook for the future work.

CHAPTER 2 MATERIAL GROWTH AND CHARACTERIZATION TECHNIQUES

2.1 Magnetron sputtering techniques

Magnetron sputtering is a widely used physical vapor deposition (PVD) technique. It was created in 1930s when F. M. Penning described the trapping of electrons in certain electric and magnetic field configurations at room temperature.[21,22,23] This later led to the further development of the modern magnetron sputtering technique in the 1970s.[24,25,26] This technique has been widely used in thin film fabrication industries, including semiconductors, solar cells, optics, magnetic storage, and many others, because it allows for fast production, pre-surface sputter cleaning, easy control, and uniformity over a large size, among others.

Magnetron sputtering is a plasma vapor deposition (PVD) process in which a plasma is created, and positively charged ions (typically argon ions) from the plasma are accelerated by an electrical field superimposed on the negatively charged electrode or "target". The positive ions are accelerated by the electrical potential and strike the negative electrode with enough force to dislodge and eject atoms from the target. The ejected atoms will be condense on substrate surfaces that are placed in proximity to the magnetron sputtering cathode. In magnetron sputtering, plasma needs to be ignited and created before sputtering target materials to substrates. A plasma is a dilute ionized gas containing free electrons and positive ions. In a vacuum chamber, argon gas is filled in with low pressure, typically several mTorr. Then a positive voltage between the cathode (targets) and the anode (shutters or substrate holders) is applied (2-5 kV). If the voltage

is larger than a breakdown voltage, ionization of argon atoms happens. This makes the gas electrically conductive and then forms a plasma. This process is called glow discharge.

The breakdown voltage is critical for the plasma ignition. It can be described by Paschen's law, which was given by Friedrich Paschen in 1889.[27]

$$V_{BD} = \frac{Bpd}{\ln(Apd) - \ln(\ln(1+1/\gamma))} \tag{2.1}$$

In this equation, V_{BD} is the breakdown voltage, p is the pressure of the neutral gas, d is the gap distance between the cathode (the target) and the anode (the substrate), A is the saturation ionization in the gas at a particular electric field/pressure ratio, γ is the secondary electron emission coefficient at the cathode, and B is related to the excitation and ionization energies.

For the system used in Dr. Mingzhong Wu's laboratory, the distance d between the cathode and the anode is 6-10 cm, and the argon gas pressure is in the range of 4-20 mTorr. Using these parameters, one would expect the breakdown voltage V_{BD} monotonically decreases with pd in the parameters range normally used for sputtering. So, one needs to increase the distance d and/or the gas pressure in order to get a lower breakdown voltage to enable plasma ignition. Experimentally, it is often convenient to increase the gas pressure to enable the ignition. As the plasma is created and sustained by frequent collisions between electrons and argon atoms, argon ions with positive charges move to and collide with the target (the cathode) surface. Then, the free electrons fly to the substrates (the anode) due to the electric field.

Figure 2.1. Top view of a magnetron sputtering gun in Dr. Mingzhong Wu's laboratory. The outer bar magnets have their S poles all pointing up, and the center magnet has an opposite pole direction.

Figure 2.1 shows the top view of a modern magnetron gun. The center magnet has an opposite pole to the surrounding magnets. The target was mounted on top of the surface shown and an electric field (DC or RF) is applied vertically to the gun surface. The motion of electrons can be described as follows. In general, the area near the top surface of the target can be treated as two regions: the cathode dark space (CDS) region on top of the target surface and the negative glow region (NG) as shown in Fig. 2.2. Free electrons move mainly under the influence of the electric field in the CDS region and the magnetic field in the NG region. Free electrons located on the surface of the target are accelerated by the electric field in the CDS region, gain kinetic energy, and move to the NG region. Then, via the Lorentz force, the magnetic field bends the electron path so that the electrons move in a circle around the center axis, being confined in the NG region. As more electrons are confined, there are more collisions between the gas atoms and the electrons, which helps ionize the neutral argon atoms and sustain the plasma. Since the bending effect depends on the mass of particles, argon ions are far less affected than electrons. The exhausted electrons, after loss of kinetic energies due to multiple collisions with atoms and ions, fly away from the CDS region towards the anode region without breaking or heating up the substrate surface.

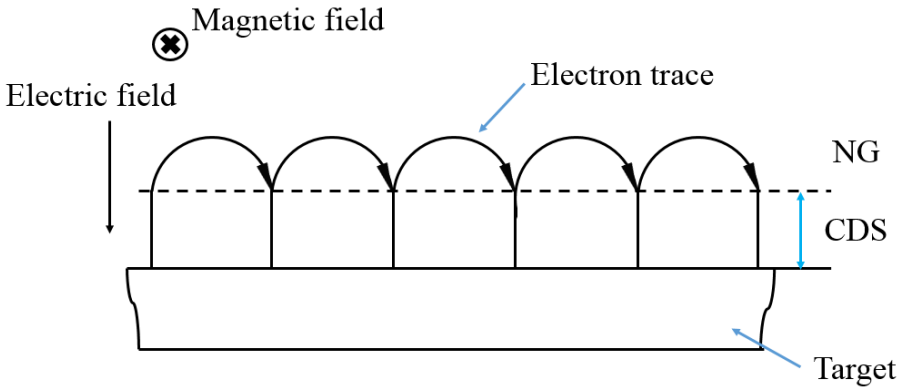

Figure 2.2. Illustration of field distribution and electron motion near the surface of the target. CDS and NG denote the cathode dark space and the negative glow regime, respectively.

On the other hand, argon ions are accelerated under the electric field and move towards the cathode target materials with an energy range from 100 eV to 2000 eV. The collision of argon ions and the atoms of the target surface can be modeled as hard sphere collisions in which the momentum transfer process dominates as the atoms hit the sputtering target. About 95% of the incident energy is transferred to heat in the target and only a small portion (about 5%) is absorbed by atoms (5–100 eV) on the surface. The atoms in the sputtering target will eject if the absorbed energy is larger than their binding energy. In a magnetron sputtering gun, chilling water is supplied on the back of the gun to remove excessive heat caused by the collision.

The magnetron sputtering system in Dr. Mingzhong Wu's laboratory has three chambers. One chamber is for metallic material deposition with three magnetron guns. The second chamber has a face-to-face setup for ceramic material deposition. The third chamber has no magnetron gun and is used as load lock for transferring samples to the two chambers with magnetron guns. A heating box is mounted on the back of the substrate holders for high-temperature (up to 800 ºC) deposition and in-situ annealing. In this dissertation, all the thin films were fabricated by using this magnetron sputtering system unless otherwise noted.

2.2 Measurement techniques

2.2.1 X-ray diffraction

X-ray diffraction techniques utilized x-ray to determine the atomic structure of crystals, either bulk or thin films. In a typical configuration, a fine focused monochromatic beam of x-rays is beamed at samples and scattered elastically, forming diffraction patterns. The angles and intensities of these diffraction patterns provide information on lattice constants, chemical bonds, lattice types, and others.

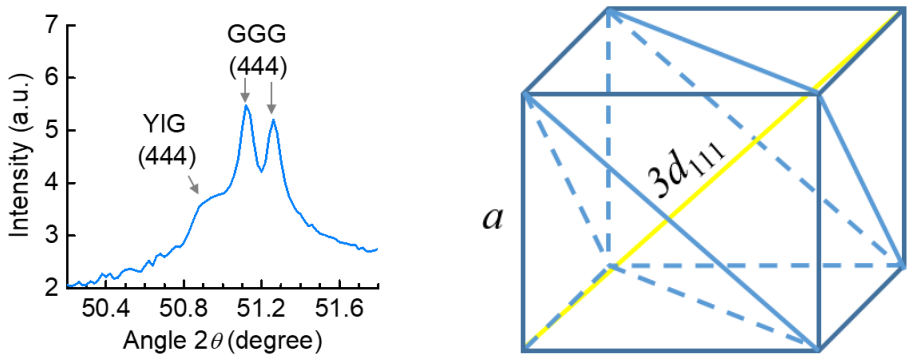

Figure 2.3. Left: X-ray 2θ scan spectrum of an 11-nm-thick YIG film grown on a GGG substrate. Right: illustration of the lattice constant a and the spacing d_{111} along <111>.

The left graph of Fig. 2.3 shows the YIG film and GGG substrate peaks of a typical X-ray 2θ scan with a Bruker D8 system at Colorado State University (CSU). The 2θ angle of the YIG (444) peak is 50.9°. The wavelength of the Cu X-ray source is 0.154 nm (K_α). Given these parameters, one can estimate the YIG lattice constant using the Braggs' law

$$2d \sin\theta = n\lambda \tag{2.2}$$

where d is the spacing between neighboring diffraction planes in the crystal, n is a positive integer indicating the Miller index, which is 4 here, and λ is the X-ray wavelength. One can calculate the lattice constant a as $a = 3d_{111}/\sqrt{3} = 3 \times (4\lambda/2\,sin\,\theta)/\sqrt{3} = 12.41$Å. This value is close

to the standard value of YIG materials, which is 12.376 Å at room temperature, and the perpendicular tensile strain is quite small.

2.2.2 Atomic force microscopy

Atomic force microscopy (AFM) is a widely used surface scanning technique because it supports resolution in sub-nanometer range. By measuring the atomic force between the probe tip and the sample, surface information such as height, friction, and magnetism can be detected and acquired.

Figure 2.4. Pictures of the AFM device in Dr. Mingzhong Wu's laboratory at CSU. The AFM tip is located under the objective lens and the sample holder is located under the AFM tip. The sample is put on the sample holder facing up for the AFM tip to detect the surface. The black knobs are for fine tuning the position calibration laser and the position of the stage.

Figure 2.4 shows the AFM device used in Dr. Mingzhong Wu's laboratory at CSU. The AFM system is from Vecco Innova Inc. The AFM system supports surface imaging with tapping and contact modes. A high-resolution microscopy on top of the probing block is for precise operations of tip mounting and laser beam alignment.

2.2.3 Vibrating sample magnetometry

Vibrating sample magnetometry (VSM) is a technique that measures magnetic properties of magnetic materials. Figure 2.5 shows the schematic of the core part of the VSM instrument. A

magnetic sample is attached to the end of a quartz rod, which is placed in the center of electromagnet. By vibrating the quartz rod up and down with a high frequency, the coil picks up a current signal from the changing magnetic field generated from the sample due to the Faraday's Law of Induction. By analyzing signal change with the external static magnetic field, the magnetic properties of the samples such as saturation induction and coercivity can be acquired. To enable high lock-in detection of the signal, a vibrating frequency of 50 kHz is used for the measurements in the dissertation.

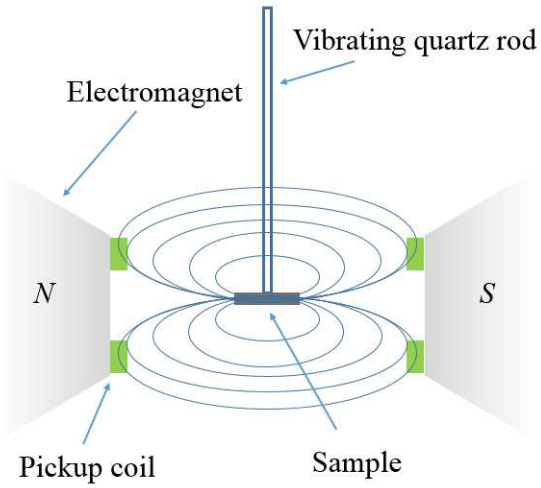

Figure 2.5. A schematic of the VSM instrument

2.2.4 Ferromagnetic resonance measurements

In a classical theory, a magnetic moment will precess about the net external magnetic field if it has a different orientation from the field. In real magnetic materials, this precessional motion cannot sustain without a continuous driving force. The interactions of magnon-phonon, magnon-electron, and magnon-magnon and other interactions can damp and decay the magnetization precession. This damping process is called magnetization relaxation.

Ferromagnetic resonance (FMR) is a method to measure magnetic properties by detecting the

precessional motion of the magnetization in a ferromagnetic material. From a macroscopic point of view, the applied static magnetic field H_0 causes the total magnetic moment to precess around the direction of the local field H_{eff}, before relaxation processes damp this precession and the magnetization aligns with H_{eff}. FMR techniques have been widely used to study the magnetization properties in magnetic materials. Measurements of FMR responses can provide information on magnetization dynamic properties, such as the Gilbert damping constant, as well as static magnetic properties, such as the saturation induction, anisotropy field, and absolute gyromagnetic ratio.

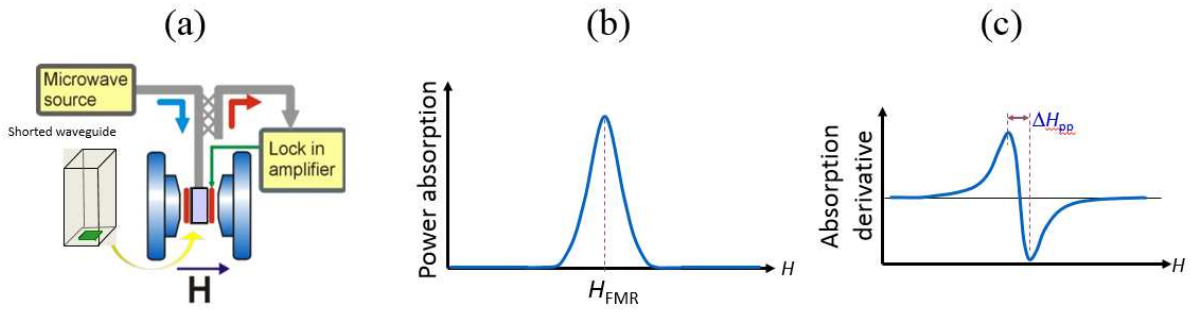

Figure 2.6. (a) Schematic for a typical FMR system using a rectangular waveguide, an electromagnet, and a lock-in amplifier. (b) A typical power absorption curve in an FMR measurement. (c) A typical curve of power absorption derivative in an FMR measurement. ΔH_{pp} represents the peak-to-peak FMR linewidth.

Figure 2.6(a) shows a schematic diagram of a typical FMR system. A sample is mounted at the end of a rectangular waveguide in which a microwave field propagates and drive the magnetic moments in the sample. The electromagnets supply a constant external magnetic field to saturate the sample. During the measurement, either the microwave frequency or the external field is swept continuously till the resonance condition is satisfied. When the resonance condition is satisfied, the power absorption reaches its maximum, and a dip arises in the reflected microwave signal which corresponds to a power absorption peak as shown in Fig. 2.6(b). A lock-in amplifier and modulation of field are utilized to enhance the signal-to-noise ratio. In this case, the detected signal

will be the derivative of the power absorption curve. The peak-to-peak linewidth shown in Fig. 2.6(c) reflects the relaxation process. Reference [28] elaborates much details on the setup, calibration, and modification of the FMR system.

In the following chapters, the magnetron sputtering technique will be used to prepare thin films and the FMR technique will be used to measure the damping constant of magnetic thin films.

CHAPTER 3 TOPOLOGICAL MATERIALS

3.1 Spin-orbit coupling

The spin-orbit coupling (SOC) is a fully relativistic interaction between a particle's spin and its translational motion. To understand it better, one can start with a hydrogen-like atom with atomic element number Z. The atomic orbitals of such an atom are solutions to the Schrödinger equation in a spherically symmetric Coulomb potential given by[29]

$$V = -\frac{1}{4\pi\epsilon_0}\frac{Ze^2}{r} \tag{3.1}$$

where ε_0 is the permittivity of the vacuum, Z is the number of protons in the nucleus, e is the elementary electronic charge, r is the distance of the electron from the nucleus. Since the energies are simply written as

$$E_n = -\frac{m_r c^2 \alpha^2 Z^2}{2n^2} \tag{3.2}$$

where m_r is the reduced mass of the system, c is the speed of light in vacuum, $\alpha \approx 1/137$ is the fine structure constant. In the core shell (first 1s orbital), the single electron moves around the nucleus at an average distance r_1 with an average velocity v_1 that are given by

$$r_1 = \frac{4\pi\varepsilon_0\hbar^2}{Ze^2 m_e} \text{ and } v_1 = \frac{ze^2}{4\pi\varepsilon_0\hbar} \cong \frac{z}{137}c \tag{3.3}$$

The heavier the element is (large Z), the smaller the radius of the atomic orbital becomes, the faster the electron circles around the nucleus, and the electric field felt by the electron is much stronger. This electric field E generated by the positively charged nucleus is proportional to Z^3 and can be written as

$$E = -\frac{1}{4\pi}\frac{ze^2}{r^2}e_r \tag{3.4}$$

The electron orbiting the nucleus in an atom naturally feels the nuclear electric field described above. But relative to the electron's rest frame, the proton orbits the electron and produces an additional magnetic field. This effective magnetic field comes from the Lorentz transformation in special relativity from the nuclear coordinate system to the moving electron coordinate system. It can also be simply seen semi-classically as a magnetic field generated by a current loop

$$\boldsymbol{B}_{eff} = \frac{\boldsymbol{E}\times\mathbf{v}}{c^2} \tag{3.5}$$

This additional magnetic field naturally couples to the moving electron via the spin, resulting in an interaction between the electron spin and the electric field. This interaction is the so-called spin-orbit coupling. Spin-orbit coupling plays an important role in modern physics. For example, the emergence of topological insulators requires strong spin-orbit coupling.

3.2 Topological insulators

In the past 15 years, topological insulators have attracted extensive interest in fundamental physics and materials science[30,31]. Topological insulators (TIs) are a kind of material with unique band structures. Figure 3.1(a) shows the band structure of a topological insulator.[32] Since there is a gap between the conduction band and the valence band, a TI is insulating in the bulk. In addition, a TI features strong spin-orbit coupling, which leads to an inverted band gap and a nontrivial topological order. As a result, there exist metallic surface states on its surfaces interfacing with trivial insulators, though it is insulating in the bulk. Such surface conducting states are called topological surface states (TSS), as shown schematically in Fig. 3.1(b). In most materials, these conducting surface states are very fragile. However, in a topological insulator, due to time reversal symmetry, the Hamiltonian describing the surface states is invariant to small perturbations, which makes the surface states topologically protected and stable under small perturbations.

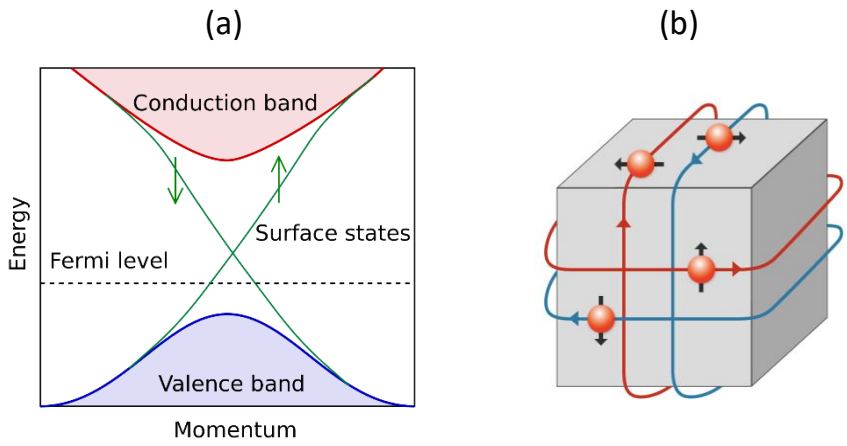

Figure 3.1. (a) Schematic of the dispersion relation in a topological insulator.[32] (b) Topological surface states in a topological insulator.

Because of the Rashba effect, the surface states on topological insulators are spin polarized. At the Fermi surface, the spins in the conducting channel are always at a right angle to their momenta. This phenomenon is called spin-momentum locking, which is a signature of TIs. Because of the spin-momentum locking, a TI has great potential in spintronics applications, such as magnetic spin-orbit torque memory devices.[33]

3.3 Topological Dirac semimetals

The TSS exist not only in TIs, but also in topological Dirac semimetals (TDSs). A TDS is a kind of three-dimensional material where the conduction and valence bands meet at points and are described by a three-dimensional Dirac equation. In a TDS, Dirac-like band crossings appear in momentum space and is protected by discrete symmetries. A schematic illustration of the electronic structure of a three-dimensional (3D) DSM is shown in Fig. 3.2.[34] BDP1 and BDP2 mark the positions of two bulk Dirac points.

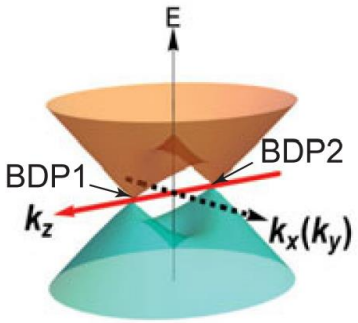

Figure 3.2. Schematic illustration of the electronic structure of a 3D TDS.[34]

TDS materials have attracted great interests since the first prediction by Young et al. in 2012.[35] Later, Wang et al. predicted that some 3D TDS family could include A_3Bi (A=Na, K, Rb) and Cd_3As_2.[36,37] Moreover, further experiments show that these materials can support nontrivial surface states.[38,39] The unusual electronic structure of TDSs leads to extraordinary physical properties, including giant linear magnetoresistance[40,41], chiral anomaly[42], novel quantum oscillations,[43] and so on. Till now, the TDS family includes the above-mentioned Na_3Bi, Cd_3As_2, and others.[38,39,44,45] Recently, α-Sn films under suitable strain was reported to be a new member in this family.[34,46] The properties of α-Sn films are introduced below.

3.4 α-Sn films

Tin (Sn) exists in two major crystalline forms: α and β, as shown in Fig. 3.3. Alpha-Sn is a zero-gap semiconductor with a face-centered diamond cubic crystal structure. At high temperature, α-Sn transforms into β-Sn that is metallic and has a body-centered tetragonal structure. For commercially pure α-Sn bulk materials, this phase transformation occurs at 13.2±0.1 °C.[47] For α-Sn thin films, however, the transformation temperature can be significantly higher and usually increases with a decrease in the film thickness. For example, previous work has demonstrated that α-Sn films of a thickness of 50 monolayers grown on (111) InSb substrates

are stable up to about 160 °C, while films of a thickness of 8 monolayers are stable up to about 200 °C.[48]

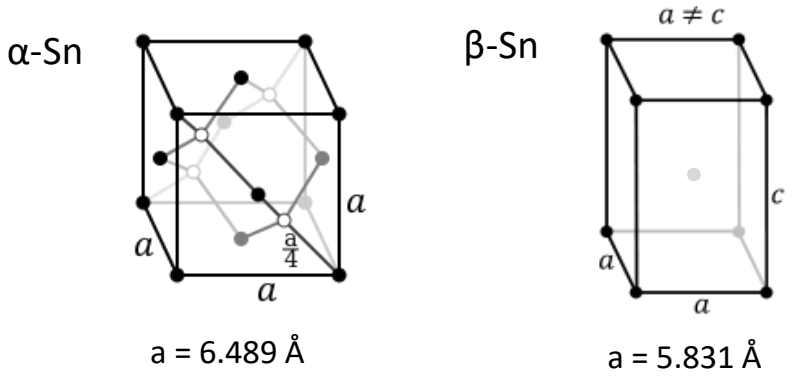

Figure 3.3. Crystal structure of α phase and β phase Sn.

Unstrained α-Sn is a gapless semiconductor in which the conduction and valence bands have a quadratic band touching at the Γ point near the Fermi level. This band touching is protected by the cubic symmetry of the α-Sn structure. If the cubic symmetry is broken by a tensile strain along the [001] or [111] direction, the two bands cross each other near the Fermi level, forming two Dirac points and giving rise to a topological Dirac semimetal (TDS) phase.[34,49,50] Such band crossing is protected by the rotational symmetry that remains unbroken by the tensile strain.

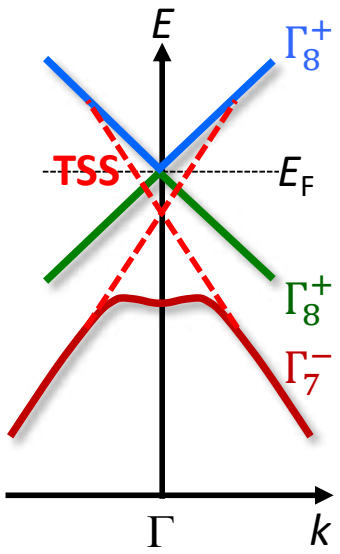

Figure 3.4. Schematic of the band structure in topological Dirac semimetal α-Sn thin films.

The TSS of the TDS α-Sn film concerned in this work originate from the band inversion – the conduction and valence bands (Γ_8^+) near the Fermi level are derived from *p* electrons while the *s* electron-derived band (Γ_7^-) is below the Fermi level, as sketched schematically in Fig. 3.4, unlike other group-IV semiconductors with the diamond structure such as Si and Ge. The Γ_7^- band is pushed below the Fermi level mainly due to the scalar relativistic effects that affect the *s* electrons.[51,52] The TSS bridge the Γ_8^+ conduction band and the Γ_7^- valence band,[49] as indicated by the red dashed lines in Fig. 3.4. The spin-momentum locking of these TSS in α-Sn has been previously confirmed via angle-resolved photoemission spectroscopy,[53,54] and its potential for efficient charge-to-spin conversion has been previously demonstrated via spin pumping experiments by Rojas-Sanchez *et al.*[55]

CHAPTER 4 SPUTTERING GROWTH OF LOW-DAMPING YTTRIUM IRON GARNET THIN FILMS

4.1 Introduction

Magnetic damping in yttrium iron garnet (YIG) $Y_3Fe_5O_{12}$ is lower than in any other magnetic material. As such, YIG materials have been widely used in microwave devices, including phase shifters, isolators, and circulators[56,57]. Recent years witnessed a strong interest in the use of YIG materials for spintronic and magnonic device applications. This interest derives mostly from the facts that the damping in YIG materials is two or three orders of magnitude lower than in ferromagnetic metals, and YIG-based devices may therefore enable faster domain wall motion, magnetization switching with lower currents, and more energy efficient information transfer than metal-based devices. In fact, there have been recent experimental demonstrations of spin-torque nano-oscillators[58] and logic gates[59] that take the advantage of nanometer-thick YIG films.

Spintronic and magnonic applications require YIG thin films with a thickness in the nanometer (nm) range, but it is challenging to grow YIG films that are nanometers thick yet exhibit a damping comparable to the bulk value. There have been rather significant efforts in using liquid phase epitaxy (LPE), pulsed laser deposition (PLD), and magnetron sputtering methods to grow nm-thick YIG films[5,10,59,60,61,62,63,64,65,66,67,68,69,70,71,72,73], but the Gilbert damping constants (α) of those films are still higher than the intrinsic damping in YIG single crystals, which is about $3\times10^{-}$

[5 82], and there is still room for the improvement of the damping of nm-thick YIG films. This chapter reports the development of nm-thick YIG films via sputtering at room temperature and post-annealing in O_2 at high temperature. The optimization of the annealing temperature enabled the realization of YIG films with $\alpha \approx 5.2\times10^{-5}$, which represents the lowest damping reported so far for magnetic films, either metallic or insulating, thinner than 200 nm.

4.2 Properties of yttrium iron garnet

Yttrium iron garnet ($Y_3Fe_5O_{12}$, YIG) was first discovered by Bertaut and Forrat in 1956.[74] YIG is a synthesized ferrimagnetic oxide insulator with nearly cubic symmetry. The lattice constant of bulk YIG material is 12.376 Å. One cubic unit cell consists of eight chemical formula units, with 24 Y^{3+} cations, 40 Fe^{3+} cations, and 96 O^{2-} anions.[75,76] Figure 4.1 presents the schematic diagrams for the iron and yttrium cations surrounded by oxygen anions in YIG materials. The Y^{3+} ion is located on a c-site and is surrounded by eight nearest oxygen anions which form a dodecahedron. Among the 40 Fe^{3+} cations, 40% are located on a-sites and 60% are located on d-sites. Six oxygen anions surround one a-site cation, forming an octahedron, while four anions are around one d-site cation and form a tetrahedron. Normally, Gadolinium gallium garnet ($Gd_3Ga_5O_{12}$, GGG) substrates are used for YIG thin film deposition. This is because the GGG single crystal has the identical crystal structure as that of the YIG crystal. The difference between the YIG and GGG lattice constants is as small as 0.01%.

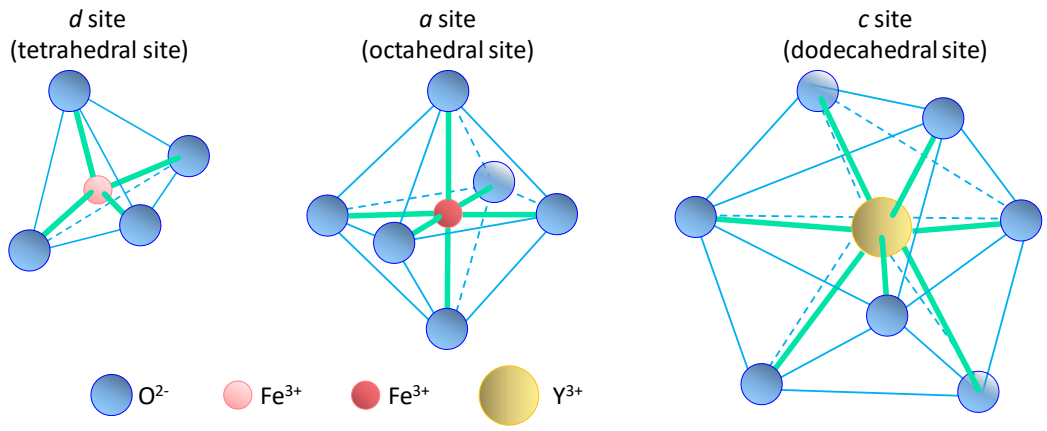

Figure 4.1. Schematic diagrams of three different sites occupied by cations in yttrium iron garnet.[9]

Figure 4.2 shows the cation placement in one octant of an YIG unit cell. The magnetization in YIG originates from super-exchange interaction[77,78] between a-site and d-site Fe^{3+} cations. The net magnetic moment of Y^{3+} cations is zero. Based on Anderson's theory[33], in magnetic ion – oxygen ion – magnetic ion bonds, the interaction is strongest with a bond angle near 180° and weakest for 90°. In the YIG crystal structure, the largest bond angle of 126.6° [79] occurs at "a-site Fe^{3+}" - O^{2-} - "d-side Fe^{3+}". This interaction leads to anti-paralleled magnetic moments between the a-site and d-site Fe^{3+} ions. Each Fe^{3+} ion contributes 5 Bohr magnetons (μ_B) and each unit cell in YIG material has a net magnetic moment of 40 μ_B (Bohr magneton). This leads to a theoretical saturation induction ($4\pi M_S$) value of 2470 G at 0 K, which is very close to the value (2463 G) measured for YIG thin films at 4.2 K in previous study.[80] At room temperature, the $4\pi M_S$ value is about 1750 G. Depending on the fabrication methods and defects in the film, the $4\pi M_S$ value may vary from 1450 to 2100 G.

The single-crystal yttrium iron garnet has weak cubic magneto-crystalline anisotropy with the easy axis along (111) direction. At room temperature, the first- and second-order cubit anisotropy constants are -6100 erg/cm^3 and -260 erg/cm^3, respectively,[81] which correspond to effective magnetic anisotropy fields of -87.6 Oe and -3.7 Oe, respectively, for a saturation induction of 1750

Oe. The negative sign of anisotropy constant indicates easy-plane anisotropy.

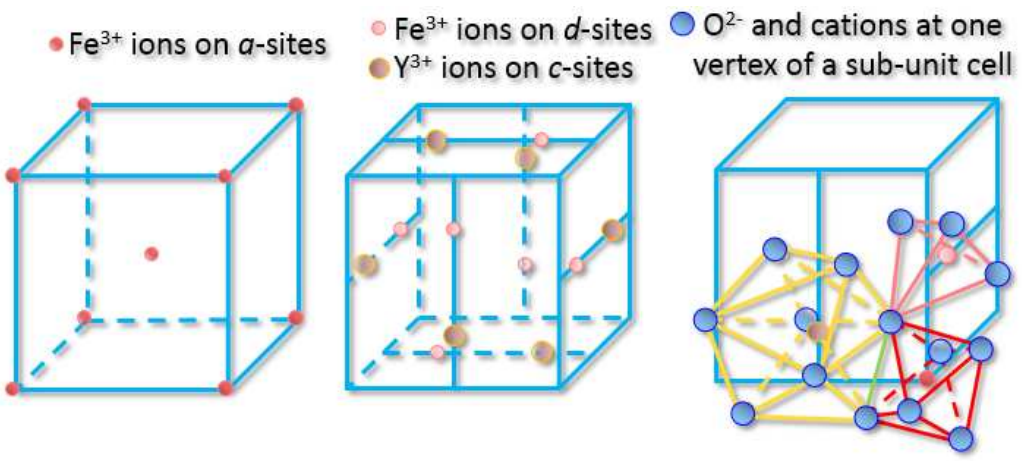

Figure 4.2. Cation arrangement in one octant of a YIG unit cell. A-site ions form a body-centered cubit (bcc) sub-unit cell. D-site and c-site cations are distributed symmetrically along the center lines of the cubic faces.[9]

The ferromagnetic resonance (FMR) linewidth originating from intrinsic damping in YIG single crystals is about 0.2 Oe at 10 GHz.[82,83] This leads to an intrinsic Gilbert damping constant α of about 3×10^{-5} assuming zero inhomogeneous linewidth broadening. This damping value is about one order of magnitude smaller than that in other magnetic insulators such as barium hexagonal ferrites[84] and two orders of magnitude smaller than that in ferromagnetic metals. The extremely small intrinsic magnetic damping makes YIG a good candidate for studies of spin waves as well as magnetic insulator-based spintronics applications. Structural and physical properties of single-crystal YIG are listed in Table 4.1. All values in the table are for room temperature unless specified.

Table 4.1. Properties of yttrium iron garnet.

Parameter	**Value**	**Reference**
Lattice constant *a* (273 K)	12.376±0.004 Å	75, 78
Lattice constant *a* (77 K)	12.361 Å	75

Lattice constant a (4 K)	12.359 Å	75
Thermal expansion coefficient (298 K)	8.3×10^{-6}	75
Thermal expansion coefficient (623 K)	11.0×10^{-6}	75
Density	5.17 g/cm^{-3}	80
Band gap	2.85 eV	80
Saturation induction $4\pi M_s$	1750 G	78
Saturation induction $4\pi M_s$ (4.2 K)	2463 G	79
Cubic anisotropy constant K_1	-6100 erg/cm^3	80
Cubic anisotropy constant K_2	-260 erg/cm^3	80
Curie temperature T_c	559 K	80
Exchange constant α	3×10^{-12} cm^2	80
Intrinsic damping constant α	3×10^{-5}	81
Faraday rotation (1.2 μm)	240 deg/cm	80
Dielectric constant (10 GHz)	14.7	85
Dielectric loss tangent (10 GHz)	0.0002	83

4.3 Sputtering growth and characterization of yttrium iron garnet thin films

The YIG films were grown on single-crystal (111) $Gd_3Ga_5O_{12}$ (GGG) substrates by radio-frequency sputtering. The GGG substrate is rinsed sequentially with acetone, isopropyl alcohol, and DI water, before being loaded into the sputtering chamber. A commercial YIG target is used that has a diameter of 2 inches and a thickness of 0.25 inches. The deposition is carried out at room temperature, at a rate of about 0.63 nm/min; prior to sputtering, the chamber system has a base pressure of 2.0×10^{-8} Torr. The deposited YIG film is then annealed at high temperature in a separate chamber. The major sputtering and post-annealing control parameters are summarized in Table 4.2. More details about the sputtering and annealing processes can be found in Refs. [61]

and [64].

Table 4.2. Sputtering and annealing parameters for YIG film fabrication.

Sputtering	Target-to-substrate distance	6.8 cm
	Sample holder rotation rate	25 rpm
	Ar pressure	20 mTorr
	Ar flow	4 sccm
	Sputtering power	75 W
	Sputtering time	120 min
Annealing	Heating rate	10 °C/min
	O_2 pressure	10 Torr
	Annealing temperature	800 - 1200 °C
	Annealing time	300 min
	Cooling rate	2 °C/min

For the YIG films presented in this letter, the surface morphological properties were analyzed through tapping-mode atomic force microscopy (AFM) measurements. The crystalline structure and film thickness were characterized through X-ray diffraction (XRD) and X-ray reflectivity (XRR) measurements, respectively. The static magnetic properties of the YIG films were measured by a vibrating sample magnetometer (VSM). The dynamic properties of the films were determined through ferromagnetic resonance (FMR) using X-band and K_u-band shorted rectangular waveguides and lock-in detection techniques. Shorted waveguide-based FMR approaches generally have lower signal-to-noise ratios and require the use of larger samples than microwave cavity-based FMR techniques, but they allow for measurements over a range of frequencies, in contrast to single-frequency measurements in the cavity FMR case. For the data presented below, the FMR frequency ranges from 8 GHz to 17 GHz, and the sample size is about

1.5 mm by 1.5 mm. The analyses of the FMR data yielded the FMR field (H_{FMR}) and linewidth (ΔH) values of the films. Note that the ΔH values presented below all refer to the peak-to-peak linewidths of the FMR power absorption derivative profiles.

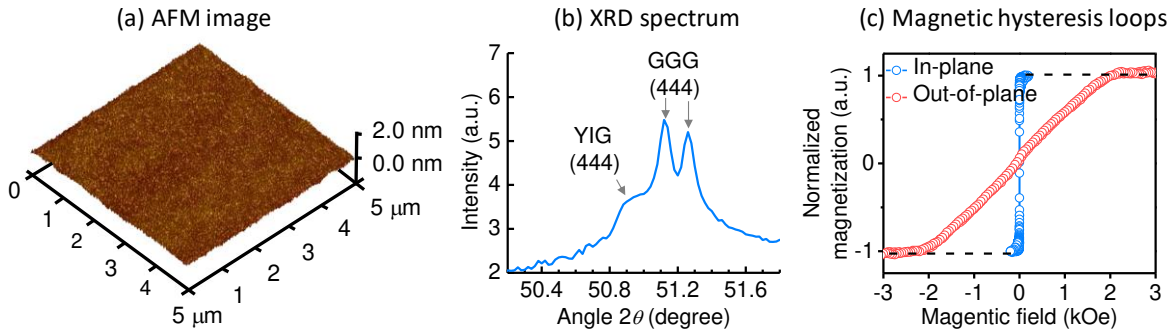

Fig. 4.3. Atomic force microscopy (AFM) surface image, X-ray diffraction (XRD) spectrum, and magnetization vs. in-plane and out-of-plane fieldresponses of a 75-nm-thick YIG film.

For the data presented below, the YIG films are all 75 nm thick. They were prepared at the same conditions except that they were annealed at different temperatures. The thickness was measured using X-ray reflection (XRR).

Figure 4.3 shows the representative data obtained for the YIG film that was annealed at 900 °C and shows the lowest damping. Figure 4.3(a) gives an AFM image which clearly indicates that the film has a very smooth surface; the analysis of the AFM data indicates a rms roughness of 0.08 ± 0.02 nm. Such smoothness allows for the fabrication of YIG-based bi-layered structures with sharp interfaces for spintronic and magnonic device applications. Note that the surface roughness values in this work were all determined by averaging over AFM measurements on five different 5 μm × 5 μm areas on the film, while the uncertainty for each roughness value is the corresponding standard deviation.

Figure 4.3(b) shows an XRD spectrum that indicates the (111) orientation of the YIG film. This is expected because (1) the GGG substrate is (111) oriented and (2) the YIG lattice almost perfectly matches the GGG lattice[9]. Note that the lattice constants of YIG and GGG materials

are 12.376 Å and 12.382 Å, respectively, at room temperature. Three important points should be made about the XRD spectrum. First, in Fig. 4.3(b) the YIG (444) peak appears as a relatively small hump on the left shoulder of the GGG (444) peaks; this hump can be much better resolved for other samples [see Fig. 4.5(a) and 4.5(b)]. Second, theoretically speaking the YIG (444) peak should be present on the right side of the GGG (444) peaks according to the Bragg's law, and the presence of the YIG (444) peak on the left side suggests that the YIG lattice has been expanded or enlarged vertically. The location of the YIG (444) peak on the wrong side of the GGG (444) peak has been previously reported[60,66,67]. Possible reasons include (1) lattice mismatching between the film and the substrate[65] and (2) small off-stoichiometry, such as oxygen deficiency, in the film[66]. For the YIG films in this work, it is believed that (2) is dominant over (1), because the YIG and GGG lattice constants are very close to each other, and the YIG films are also relatively thick and are therefore expected to be insensitive to the interfacial lattice mismatching. Third, the above-described lattice expansion may induce magneto-elastic anisotropy in the YIG film. For the films in this work, one can expect an easy-plane anisotropy, as discussed in detail in Ref. 14. This corresponds to $H_a<0$, if one defines H_a as the effective field of the uniaxial perpendicular anisotropy in the film.

Figure 4.3(c) presents magnetization vs. field (H) hysteresis loops measured with a VSM system at different field directions, as indicated. The analysis of the loop data measured with an in-plane (IP) field yields a saturation induction ($4\pi M_s$) of about 1778±15 G, which is very close to the bulk value (1750 G), and a coercivity of only about 0.18 Oe, which indicates the presence of weak anisotropy and very few defects in the film. These VSM results, together with the AFM and XRD results, clearly suggest that the film is of high quality and is therefore expected to show low damping. The damping properties are presented below.

4.4 Damping of yttrium iron garnet thin films

The left column in Fig. 4.4 shows the FMR data measured with an in-plane (IP) field. The blue circles in Fig. 4.4(a-i) show a representative FMR profile which was measured at a frequency (*f*) of 14.5 GHz. The red curve shows a fit to a derivative Lorentzian trial function. Figures 4.4(a-ii) and 4.4(a-iii) show H_{FMR} and ΔH, respectively, as a function of *f*. The dots show the experimental data obtained through the Lorentzian fitting, while the lines show numerical fits, which are explained below.

The line in Fig. 4.4(a-ii) is a fit to the Kittel equation

$$\omega = 2\pi|\gamma|\sqrt{H_{\mathrm{FMR}}(H_{\mathrm{FMR}} + 4\pi M_{\mathrm{s-eff}})} \tag{4.1}$$

where $\omega = 2\pi f$ is the angular frequency, $|\gamma|$ is the absolute gyromagnetic ratio, and $4\pi M_{\mathrm{s-eff}}$ denotes $4\pi M_{\mathrm{s}} - H_a$. H_a is the effective field of a perpendicular anisotropy in the YIG film; "$H_a > 0$" and "$H_a < 0$" correspond to an easy-axis anisotropy along the film normal direction and an easy-plane anisotropy in the film plane, respectively. One physical origin of H_a is the above-discussed magneto-elastic anisotropy associated with the lattice expansion in the YIG film[88]. The other is associated with the magneto-crystalline anisotropy in the YIG film. In brief, single-crystal YIG materials exhibit cubic magneto-crystalline anisotropy, with anisotropy constants K_1 = -6100 erg/cm^3 and K_2 = -260 erg/cm^3. For a (111)-oriented YIG film, such a crystalline anisotropy gives rise to an easy-axis anisotropy along the film normal direction that can be described by an effective field

$$H_a = \frac{2|K_1|}{M_s} + \frac{4|K_2|}{M_s} \tag{4.2}$$

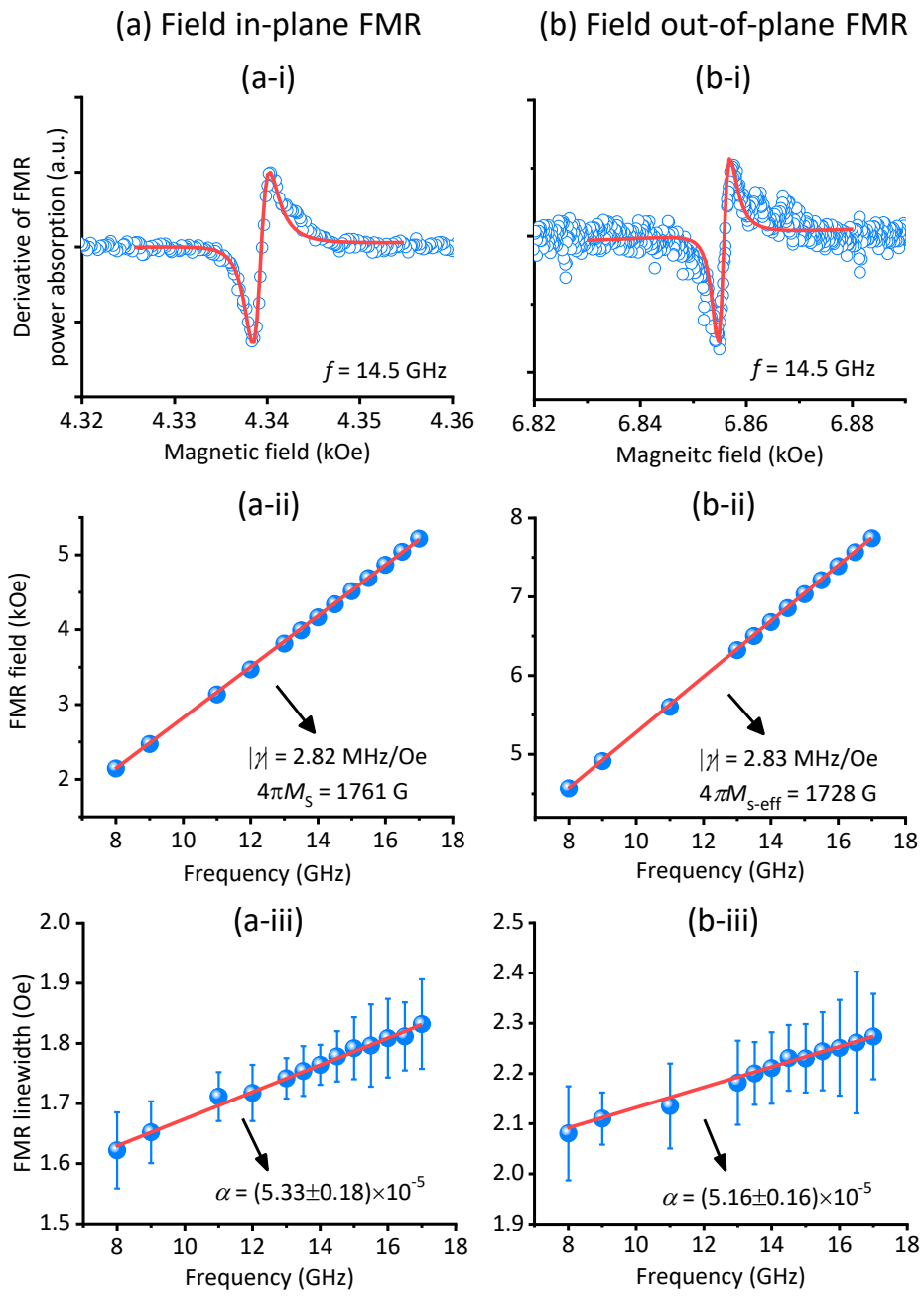

Figure 4.4. Ferromagnetic resonance (FMR) data on a 75-nm-thick YIG film. The left and right columns show the data for field IP and OOP FMR measurements, respectively. In each column, the first graph shows an FMR profile and a Lorentzian fit. The second and third graphs show the FMR field and linewidth data, respectively, which were obtained via the Lorentzian fitting. In all the graphs, the blue symbols show the data, while the red lines show the fits.

Taking $4\pi M_s$ = 1778 G presented above, one can use Eq. (4.2) to calculate and obtain $H_a \approx$ 94 Oe. Note that the actual H_a associated with the magneto-crystalline anisotropy in the YIG film should be smaller than 94 Oe because the film is not single-crystal. The linear fitting in Fig. 4.4(a-ii) yields $4\pi M_{s-\mathrm{eff}}$ = 1761 G, which indicates an anisotropy field of $H_a = 4\pi M_s - 4\pi M_{s-\mathrm{eff}} \approx 17$ Oe. A discussion about this H_a value is presented shortly. The fitting also yields $|\gamma|$ = 2.82 MHz/Oe, which is very close to the standard value (2.8 MHz/Oe).

The line in Fig. 4.4(a-iii) is a numerical fit to

$$\Delta H = \frac{2\alpha}{\sqrt{3}|\gamma|}\frac{\omega}{2\pi} + \Delta H_0 \tag{4.3}$$

where ΔH_0 denotes the line broadening due to the spatial inhomogeneity in the YIG film. The fitting gives $\alpha = (5.33 \pm 0.18)\times 10^{-5}$ and ΔH_0 = 1.46±0.06 Oe, which are key results of this work, as discussed shortly. It should be noted that the damping constant and its error were obtained through the mathematical least-square fitting of the mean values of ΔH excluding their error bars. The purpose of presenting the error bars of the ΔH data points in Fig. 4.4(a-iii) is to show the quality of the Lorentzian fitting of the FMR profiles, such as the fitting shown in Fig. 4.4(a-i).

It is known that if present, two-magnon scattering can contribute to ΔH and thereby change the slope of the ΔH vs. f response, making it bigger or smaller, or turn an otherwise linear response to a curve response[86,87,88,89]. As such, the above-presented α value may not represent the true damping in the film. To check this, FMR measurements were also carried out in an out-of-plane (OOP) field configuration in which there are no degenerate spin-wave modes at the FMR frequency and two-magnon scattering is therefore prohibited. The right column of Fig. 4.4 shows the data. The graphs are shown in the same format as those in the left column, to ease the comparison. The line in Fig. 4.4(b-ii) is a fit to

$$\omega = 2\pi|\gamma|(H_{\mathrm{FMR}} - 4\pi M_{s-\mathrm{eff}}) \tag{4.4}$$

while the line in Fig. 4.4(b-iii) is a fit to Eq. (4.3). The linear fitting in Fig. 4.4(b-iii) yields α = (5.16 ± 0.16)×10^{-5} and ΔH_0 = 1.92±0.07 Oe. This damping value is only about 3.2% smaller than the value from the IP FMR measurements. This nearly perfect agreement clearly confirms that the two-magnon scattering, if present, is very weak in the YIG film.

The fitting in Fig. 4.4(b-ii) yields $4\pi M_{\mathrm{s-eff}}$ = 1728 G, which indicates an anisotropy field of $H_a = 4\pi M_{\mathrm{s}} - 4\pi M_{\mathrm{s-eff}} \approx 50$ Oe. Thus, one can see the two H_a values (17 Oe and 50 Oe) from the FMR measurements are both positive and are both smaller than the value (94 Oe) expected according to Eq. (4.2). This result indicates that in the YIG film concerned here the magneto-crystalline anisotropy ($H_a > 0$) is stronger than the magneto-elastic anisotropy ($H_a < 0$). Further, one can see that the H_a values from the IP and OOP FMR measurements do not match with each other. Possible reasons for this mismatching include misalignment of the magnetic field during the FMR measurements and errors in the field measurements.

The above-presented α values represent the lowest value reported so far for magnetic films, either metallic or insulating, thinner than 200 nm. This low damping is associated with the high structural quality of the YIG film that is evidently indicated by the very small surface roughness, very small H_c, and similarity of both $4\pi M_{\mathrm{s}}$ and $|\gamma|$ to the standard values. In general, the damping in magnetic insulators may consist of an intrinsic contribution from magnon-phonon scattering and an extrinsic contribution from two-magnon scattering. In the YIG film concerned here, the two-magnon scattering process is very weak, as indicated by the linear behavior of the ΔH vs. f response over the entire 8-17 GHz range shown in Fig. 4.4(a-iii) and the consistency of the IP and OOP FMR measurements shown in Figs. 4.4(a-iii) and 4.4b(iii). This result is most likely because the density of the defects in the film is low. The very smooth surface suggests the absence of large imperfections on the film surface, while the very small coercivity and the

consistency of $4\pi M_S$ with the bulk value indicate the absence of high-density defects in the film bulk.

Table 4.3. Properties of YIG thin films reported previously.

Thickness (nm)	$4\pi M_S$ (G)	α ($\times 10^{-5}$)	Reference
9	1996	71	[57]
19	1670	23	[58]
20	1700	23	[60]
10.2	1770	103	[61]
100	1809	28	[62]
83	1294	70	[63]
22.3	1795	8.6	[64]
36.5	1606	91	[65]
23	1600	18	[66]
56	1795	6.2	[67]
79	1721	22	[68]
30	1715	80	[69]
106	1780	12	[70]
50	1721	140	[93]
18	1800	34	[71]
42	1724	9	[73]
110	1800	26	[94]
54	1800	24	[59]
50	1377	855	[72]
75	1778	5.2	This work

Table 4.3 compares the properties of the YIG film discussed above with those of some YIG films reported previously. One can see that the films showing relatively small damping values all exhibit a $4\pi M_S$ value relatively close to the bulk value. It should be noted that Table 4.3 serves to provide an overview of the properties of YIG thin films in recent studies, and a rigorous comparison of the listed α values may be inappropriate because the actual α values also depend

on (1) the FMR measurement techniques, and (2) the data analysis approaches, in particular, when multiple peaks appear in the FMR profiles.

Table 4.4. Static magnetic and ferromagnetic resonance (FMR) properties of nm-thick, low-damping YIG thin films reported previously.

Thickness (nm)	$4\pi M_S$ (G)	FMR field configuration	α ($\times 10^{-5}$)	ΔH (Oe) (FMR frequency)	ΔH_0 (Oe)	Reference
19	1670	In-plane	23	4.0 (15 GHz)	2.9	[59]
20	1700	In-plane	23	3.5 (15 GHz)	2.1	[60]
22.3	1795	Out-of-plane	8.6	6.9 (15 GHz)	6.4	[64]
23	1600	In-plane	18	2.4 (15 GHz)	1.2	[66]
56	1795	In-plane	6.2	1.4 (12 GHz)	1.1	[67]
79	1721	In-plane	22	2.5 (14 GHz)	1.5	[68]
106	1780	Out-of-plane	12	1.2 (14 GHz)	0.4	[70]
42	1724	Out-of-plane	9	1.8 (15 GHz)	1.5	[73]
75	1778	Out-of-plane	5.2	2.2 (15 GHz)	1.9	This work

In addition to the damping constant α, ΔH is also a relevant parameter for certain device applications. What's more, ΔH_0 is also a very useful parameter because it speaks about the spatial homogeneity of the films. In consideration of these facts, Table 4.4 compares the α, ΔH, and ΔH_0 values, as well as the thickness and $4\pi M_S$ values, of several YIG thin films with $\alpha \leq 2.3\times10^{-4}$. The third column indicates the direction of the static magnetic field relative to the film plane during the FMR measurements. The fifth column lists the ΔH values measured at or near 15 GHz. All the ΔH and ΔH_0 values are peak-to-peak linewidths.

One can see from the data in Table 4.4 that even though the YIG film in this work shows the lowest α value, its ΔH and ΔH_0 values are not the lowest. The 106-nm film, which was grown

by the LPE method, has both the lowest ΔH and ΔH_0 values[70], among all the films. For the films thinner than 100 nm, the 56-nm YIG film, which was grown by the PLD technique, shows the lowest ΔH and ΔH_0 values[67]. The fact that these two films exhibit smaller ΔH and ΔH_0 values than the YIG film in this work may suggest that LPE and PLD are better techniques than sputtering in terms of the realization of nm-thick, highly-homogeneous, low-ΔH YIG films. It may also result from the use of different FMR measurement techniques. The measurements in [67] and [70] were carried out using a strip line and a coplanar waveguide, respectively, with the help of a vector network analyzer. Depending on the widths of the strip line and the co-planar waveguide signal line, these FMR techniques may allow for measurements of film samples with size much smaller than the YIG sample in this work; in general, ΔH_0 is larger in films with larger dimensions.

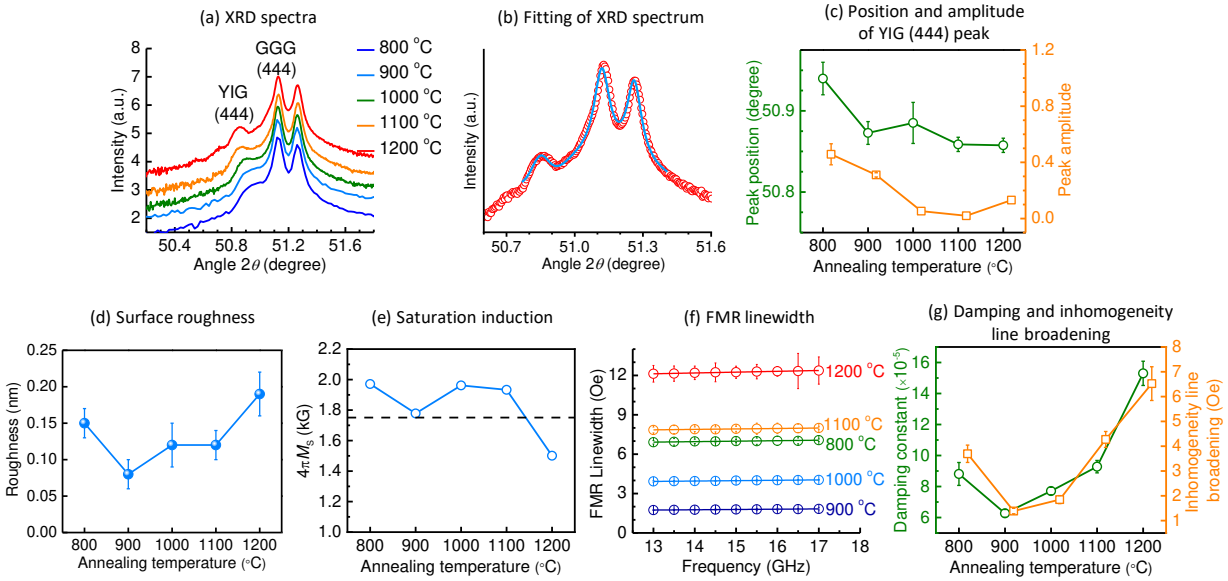

Figure 4.5. Effects of the post-annealing temperature on the properties of YIG thin films. In (b), the red circles show the experimental XRD data measured on the film annealed at 1200 °C, while the blue curve shows a fit. The data in (c) were obtained from fitting, such as that shown in (b). The error bars in (c), (d), (f), and (g) are the standard deviation values from the numerical analyses or fitting which are described in the text.

The above discussions indicate that the damping properties of a YIG film depend on the

structural properties of the film. This result is further elucidated by the data in Fig. 4.5, which were obtained on five YIG film samples annealed at different temperatures. Figure 4.5(a) gives the XRD spectra. Figure 4.5(b) illustrates the numerical fitting of the XRD profile. The red circles show the same profile as the red one in Fig. 4.5(a), while the blue curve shows a fit that consists of three Viogt functions: one for the YIG (444) peak and the other two for the GGG (444) peaks. Such fitting was performed for all the five profiles shown in Fig. 4.5(a); the fitting-yielded results are presented in Fig. 4.5(c), where the left and right axes show the position of the YIG (444) peak and the amplitude of the YIG (444) peak normalized by the amplitude of the dominant GGG (444) peak, respectively. Figures 4.5(d) and 4.5(e) show the surface roughness and $4\pi M_s$ as a function of the annealing temperature (T_a). Figure 4.5(f) gives ΔH vs. f responses for the five samples which were measured with IP fields. The symbols show the data, while the lines show fits to Eq. (4.3). The fitting-yielded α and ΔH_0 values are presented in Fig. 4.5(g).

The data in Fig. 4.5 indicate three important results. First, T_a plays a crucial role in the structural properties of the YIG thin films. This is evident from (i) the evolution of the YIG (444) peak with T_a, which is shown in Figs. 4.5(a) and 4.5(c), (ii) the change of the surface roughness with T_a, which is shown in Fig. 4.5(d), and (iii) the dependence of the film spatial inhomogeneity on T_a, which is indicated by the ΔH_0 data shown in Fig. 4.5(g). Second, there is a strong correlation between the T_a dependences of the roughness, $4\pi M_s$, α, and ΔH_0 data; the films with small α values show small roughness values, close-to-bulk-value $4\pi M_s$, and small ΔH_0, and vice versa. Third, among the five annealing temperatures, 900 °C appears to be the best in terms of the realization of a smooth, homogeneous, low-damping YIG film. These results together show that T_a critically affects the structural properties of the YIG films and thereby plays an essential role in the damping properties of the films.

4.5 Conclusions and outlook

Three final remarks are as follows. (i) Previous and ongoing efforts on YIG film growth utilize mainly LPE, PLD, and sputtering techniques, but sputtering is a much more industry-friendly approach. (ii) In order to clarify the role of T_a, the thicknesses of the YIG films were kept the same in this work, which is 75 nm. To realize low-damping films that are much thinner or thicker, one may need to use an annealing temperature other than 900 °C. (iii) The damping analyses in this work were based on the Gilbert model, which does not capture two-magnon scattering. As a result, if the two-magnon scattering is present, strictly speaking one cannot use Eq. (4.3) to fit the ΔH data measured under IP fields, even though it is appropriate to use it to fit the OOP ΔH data. In this work, however, Eq. (4.3) is approximately valid because the two-magnon scattering is very weak, which is indicated by the linear behavior of the ΔH vs. f response and the agreement of the α values from the IP and OOP FMR measurements.

There are several future works that are of great interest. (i) FMR linewidth in YIG thin films represents a complex subject. In addition to magnon-phonon scattering and two-magnon scattering, there are also valence-exchange, slowly-relaxing-impurity, and rapidly-relaxing impurity mechanisms that contribute to the FMR linewidth of YIG materials, in particular, at low temperature. It would be very interesting to separate the quantize the contributions of different mechanisms to the overall FMR linewidth in the nm-thick YIG films through comprehensive frequency-, temperature, and field angle-dependent FMR measurements. Such studies may enable further improvement in the damping of nm-thick YIG films. (ii) The YIG films in this work exhibits magneto-elastic anisotropy, which is uniaxial (along the film normal), and magneto-crystalline anisotropy, which is three-fold in the film plane. Future study is very interesting that takes advantage of field angle-dependent FMR measurements to determine the anisotropy axes

and constants in the films[90]. (iii) The YIG films in this work have weak anisotropy, but certain device applications, such as racetrack memory[91,92], may require YIG films with perpendicular anisotropy[88,93,94]. The development of such films is presented in the next Chapter.

This work is published on IEEE Magn. Lett. 11, 5502305 (2020). The full author list is Jinjun Ding, Tao Liu, Houchen Chang, and Mingzhong Wu. Tao Liu prepared the YIG films. Jinjun Ding performed FMR measurements on the films. Houcheng Chang helped with preparation of the film.

CHAPTER 5 NANOMETER-THICK YTTRIUM IRON GARNET FILMS WITH PERPENDICULAR ANISOTROPY AND LOW DAMPING

5.1 Introduction

Magnetic thin films with perpendicular anisotropy manifest themselves as core components in a wide variety of electronic devices that range from hard disk drives[95] to magnetic tunnel junction (MTJ)-based sensors[96,97],spin-transfer-torque (STT) memory[91,98], racetrack memory[99], spin-torque nano-oscillators (STNOs)[100,101], and spin-wave logics[102]. For magnetic films in such applications, perpendicular magnetic anisotropy (PMA) is essential because it dictates the thermal stability, reliability, scalability, density, and/or compatibility of the devices. On the other hand, low damping is also essential for many of those applications. To give a few examples, the critical current for switching in STT memory is proportional to the damping constant (α) in PMA films; the speed of domain wall motion in racetrack memory is generally inversely proportional to α; the threshold current for auto-oscillations in STNOs scales with α; and the spin-wave decay rate in spin-wave logic devices increases with α. As such, it is of great technological significance to search for magnetic thin films that exhibit (1) PMA and (2) low damping.

In terms of magnetic damping, yttrium iron garnet (YIG) is probably the most interesting material — α in YIG single crystals can be as low as 3×10^{-5}, which is lower than in any other known magnetic materials[9,82]. However, YIG thin films unfortunately do not show PMA, as

discussed in Chapter 4; magneto crystalline anisotropy in YIG materials is weaker than most magnetic materials. Nevertheless, several recent works suggest that one can realize PMA in YIG thin films through substrate lattice mismatching-induced epitaxial strain[65,103,104,105]. In fact, two of those works even succeeded in the realization of YIG thin films in which PMA is so strong that the hysteresis loops are nearly square[104,105]. Those works, though intriguing and enlightening, reported no results about the damping properties of the YIG films. Demonstration of YIG thin films that are nm-thick, show PMA, and exhibit low damping simultaneously, are still awaiting.

This chapter reports nm-thick YIG thin films with both PMA and low damping. The YIG films, with a thickness range of 4-30 nm, were deposited by magnetron sputtering at room temperature first and then annealed in O_2 at high temperature. The substrates are $Gd_3(Sc_2Ga_3)O_{12}$ that share the same crystalline structure as the YIG but have a lattice constant slightly larger than that of the YIG, resulting in an out-of-plane tensile strain and a PMA in the YIG film. The PMA was confirmed by vibrating sample magnetometer (VSM), magneto-optical Kerr effect (MOKE), anomalous Hall effect (AHE), and angle-dependent ferromagnetic resonance (FMR) measurements. The damping of the films was analyzed through frequency-dependent FMR measurements. As an example, an 8-nm-thick YIG film showed an effective PMA field of about 2800 Oe, a square-like hysteresis loop with a remnant-to-saturation magnetization ratio of 98 %, and a damping constant of about 4.2×10^{-4}. As an illustration of possible applications of such films, current-induced magnetization switching of PMA YIG films was demonstrated using YIG/Pt bi-layered devices.

5.2 Film growth and characterization

The YIG films were grown on single-crystal (111) gadolinium scandium gallium garnet $Gd_3(Sc_2Ga_3)O_{12}$ (GSGG) substrates by radio-frequency sputtering. The lattice constant of the

GSGG substrates is about 12.554 Å at room temperature. This constant is slightly larger than the lattice constant in YIG materials which is 12.359 Å at 4 K, 12.361 Å at 77 K, and 12.376 Å at 273 K. This lattice mismatching is crucial for the realization of PMA in the YIG films, as discussed shortly. The GSGG substrates are rinsed sequentially with acetone, isopropyl alcohol, and DI water, before being loaded into the sputtering chamber. A commercial YIG target is used that has a diameter of 2 inches and a thickness of 0.25 inches. The deposition is carried out at room temperature, at a rate of about 0.94 nm/min; before sputtering, the chamber has a base pressure of 2.0×10^{-8} Torr. The as-deposited YIG films are amorphous. To realize the crystalline structure, they are annealed in O_2 at high temperature in a separate chamber. The major sputtering and post-annealing control parameters are summarized in Table 5.1. More information about the sputtering and post-annealing processes can be found in Refs. [61,64].

Table 5.1. Sputtering and post-annealing control parameters for YIG film fabrication.

Sputtering	Target-to-substrate distance	4.8 cm
	Sample holder rotation rate	10 rpm
	Ar pressure	20 mTorr
	Ar flow	4 sccm
	Sputtering power	80 W
	Sputtering time	4-13 min
Annealing	Heating rate	5 °C/min
	O_2 pressure	25 Torr
	Annealing temperature	900 °C
	Annealing time	180 min
	Cooling rate	2 °C/min

As control samples, YIG thin films were also grown on single-crystal (111) gadolinium gallium garnet $Gd_3Ga_5O_{12}$ (GGG) substrates. The GGG substrates have a lattice constant (12.382

Å) very close to that in YIG materials, so they are the most common substrates for YIG film growth.

For the YIG films presented in this article, the surface morphological properties were analyzed through tapping-mode atomic force microscopy (AFM) measurements. The crystalline structure was characterized through X-ray diffraction (XRD) measurements. The film thicknesses were determined through X-ray reflectivity (XRR) and ellipsometry measurements.

The static magnetic properties of the YIG films were measured by a vibrating sample magnetometer (VSM) and a polar magneto-optical Kerr effect (MOKE) system. They were also examined through electric transport measurements on a Hall bar device made of a YIG/Pt bi-layered structure. The dynamic properties of the films were determined through (1) polar angle-dependent ferromagnetic resonance (FMR) measurements using an X-band rectangular microwave cavity with a resonance frequency of 9.5 GHz and (2) frequency-dependent FMR measurements using a broadband vector network analyzer FMR (VNA-FMR) spectrometer. For (1), field modulation and lock-in detection techniques were used to increase the sensitivity of the FMR measurements. For (2), a coplanar waveguide (CPW) was used to provide microwave magnetic fields to the YIG films.

This section describes the use of static and dynamic measurements, respectively, to characterize the PMA properties of the YIG films grown on GSGG substrates. Figure 5.1 shows representative hysteresis loops of the PMA YIG films. The first row presents the data obtained on a 6-nm-thick YIG film with three different measurement techniques. Specifically, graphs (a) and (b) show the data obtained with a VSM system, graph (c) presents the data measured with a polar MOKE system, and graph (d) gives the anomalous Hall effect (AHE) resistivity data obtained with a YIG/Pt Hall bar structure. The second row presents the data measured with the same technique, namely, the VSM method, but on four YIG films of different thicknesses, as indicated.

During the measurements, an external static magnetic field (H) was applied in the film plane for the data in graph (a), but was applied out-of-plane for the data shown in all other graphs.

The VSM data in graphs (a) and (b) clearly show that (1) the magnetization is relatively hard to saturate when the field is in-plane ((IP) but is much easier when the field is out-of-plane (OOP); (2) the coercive field (H_C≈4 Oe) is close to zero for the IP configuration; (3) the hysteresis loop is nearly square and shows a very high remnant-to-saturation magnetization ratio (M_r/M_s≈97 %) for the OOP configuration. These results are typical responses of magnetic thin films with PMA and thereby evidently confirm the presence of the PMA in the YIG film.

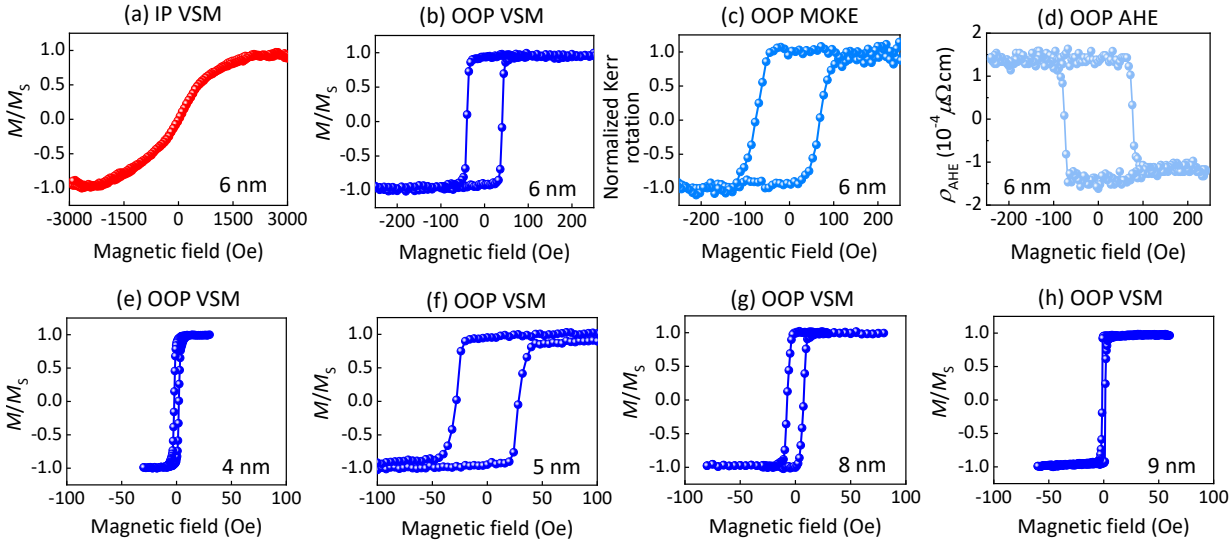

Figure 5.1. Magnetic hysteresis responses of YIG thin films grown on GSGG substrates. (a), (b), (c), and (d) show the hysteresis loops measured on a 6-nm-thick YIG film. The data in (a) and (b) were measured by a vibrating sample magnetometer (VSM) under an in-plane (IP) field and an out-of-plane (OOP) field, respectively. (c) and (d) show the magneto-optical Kerr effect (MOKE) data and the anomalous Hall effect (AHE) resistivity data, respectively, both measured with OOP fields. (e), (f), (g), and (h) show the VSM data measured with OOP fields on YIG films of different thicknesses, as indicated. Note that the data in (d) were measured with a YIG/Pt Hall bar structure.

Turn now to the comparison of three hysteresis loops in graphs 5.1 (b), (c), and (d) which were obtained on the same 6-nm film in the same field configuration but with different techniques. Five important results are evident. (1) The data all show square-like loops with near 100% M_r/M_s

ratios. Thus, the presence of PMA in the 6-nm YIG film is confirmed by three completely distinct measurement techniques. (2) The data in graph (b) were measured on a sample with a dimension of 10 mm by 10 mm, the MOKE data in graph (c) were obtained with a laser beam size of about 8 μm, and the AHE data in graph (d) were collected with a Hall bar structure that had a bar width of 10 μm. In spite of this size difference, the hysteresis loops are similar to each other, which indicates that the presence of the PMA is independent of the sample dimension. (3) The MOKE technique probes the entire thickness of the YIG film, while the AHE measurement examines only the magnetization at the YIG/Pt interface, as explained shortly. The consistency of the MOKE and AHE hysteresis loops indicates no major differences between the PMA in the bulk and that on the surface. (4) The comparison of the MOKE and AHE loops suggests that the growth of a Pt layer on top did not result in a notable degradation of the PMA in the YIG film. (5) From the VSM, MOKE, and AHE data, one can estimate H_c values to be 42 Oe, 73 Oe, and 76 Oe, respectively. One can see that the values from the MOKE and AHE loops agree with each other, but they are larger than the VSM value. This observation correlates with the sample size relation mentioned above. Specifically, the MOKE and AHE measurements were carried out on film areas (about 10×10 μm^2) substantially smaller than the samples used in the VSM measurements (about 10×10 mm^2). Because of this considerable difference in the sampling area, the magnetic domain nucleation processes in the MOKE and AHE measurements can be different from those in the VSM measurements. This could be the reason why a difference in the H_c values was observed.

It is worth highlighting that the above-presented results about the independence of the PMA from the film lateral dimension, the consistency between the bulk and surface properties, and the robustness of the PMA against the growth of a heavy metal capping layer are important in terms

of device applications of PMA YIG thin films.

It should also be explained that the AHE response usually occurs only in ferromagnetic metals and the AHE in the Pt layer of the YIG/Pt structure may originate (1) from the magnetic proximity effect, namely, magnetic ordering in the Pt layer induced due to the proximity to the YIG layer[106], (2) by the effects of the imaginary part of the spin-mixing conductance at the interface[107], or (3) due to the spin-dependent scattering of itinerant electrons in the Pt layer with the magnetic interface[108]. One can write the Hall resistivity in the Pt layer as

$$\rho_H = \rho_{OHE} + \rho_{AHE} = R_0 H + R_a M \tag{5.1}$$

where ρ_{OHE} denotes the ordinary Hall effect (OHE) resistivity in the Pt layer, M is the magnetization in the YIG film, and R_0 and R_a are constants. For the data shown in graph (d), the ρ_{OHE} component, scaling linearly with H, has already been subtracted. From Eq. (5.1), one can see that the ρ_{AHE} vs. H loop can evolve in the same or opposite manner as the M-H loop, depending on the sign of R_a. The opposite sign of the AHE and MOKE loops shown in Fig. 5.1 clearly indicates that R_a is negative in the YIG/Pt structure, which is consistent with the previous reports on the AHE responses in YIG/Pt[106,109] and $Tm_3Fe_5O_{12}$/Pt[110,111] bi-layered structures. Note that the data in graph (d) were measured at room temperature. The AHE resistivity loop can show an opposite evolution at low temperature, as reported previously[106].

Graphs (b), (e), (f), (g), and (h) present the hysteresis loops measured with the same technique, namely, the VSM, under the same field, namely, an OOP field, for five YIG films with different thicknesses (t), as indicated. The data clearly indicate that PMA and the resulting square-like loop exist in YIG films with a thickness ranging from 4 nm to 9 nm. Although not shown, the loop evolves gradually from a nearly square shape with a M_r/M_s ratio of 64.4% to a well tilted or sheared shape with a M_r/M_s ratio of only 0.3% when the film thickness t is increased from 10 nm

to 30 nm. This evidently shows the degradation of the PMA with an increase in t. The reason for this degradation is discussed in section 5.3.

The analyses of the VSM data, such as those shown in Fig. 5.1, can yield the H_c, saturation induction $4\pi M_s$, and effective PMA field H_k values of the YIG films. Table 5.2 lists such values for eight samples. The first column gives the nominal thickness values (t) of the YIG films, which were determined through the XRR and ellipsometry measurements. The second column lists the $4\pi M_s$ values estimated from the saturation magnetic moments obtained from the VSM measurements under OOP fields. The estimation assumed a 2-nm-thick interfacial layer with zero moments at the YIG/GSGG interfaces. This "dead" layer results from the interfacial diffusion of Y^{3+} ions in the YIG film and Gd^{3+} ions in the substrate. As Y^{3+} ions have no magnetic moments but Gd^{3+} ions do, the substitution of Y^{3+} by Gd^{3+} in this interfacial layer can result in antiferromagnetic coupling between the magnetization in this layer and that in the YIG bulk, as studied previously through magneto-optical spectroscopy[112], neutron reflectivity[113, 114], and energy-dispersive x-ray spectroscopy measurements[115]. The interfacial layer thickness reported previously ranges from about 1 nm to 7 nm; such a wide range may result from the use of different YIG film growth conditions. For the YIG films in this work, the estimation of the dead layer thickness (2 nm) was based on polarized neutron reflectometry measurements of the depth dependence of both the structure and the magnetism in the YIG films[116].

Table 5.2. Static magnetic properties of PMA YIG thin films.

Thickness (nm)	**$4\pi M_S$ (G)**	**H_k (Oe)**	**H_c (Oe)**
4	1206±11	2556±16	2.5±0.4
5	1243±8	2443±14	28±0.8
6	1218±6	3428±17	42±1.6
7	1319±9	2819±16	32±1.6
8	1427±4	2827±11	7.5±0.8
9	1491±8	2741±12	1.5±0.4
10	1663±12	2263±21	5.0±0.4
12	1758±13	2058±25	0.3±0.1

The third column in Table 5.2 lists the H_k values evaluated according to

$$H_s = H_k - 4\pi M_s = \frac{2K_u}{M_s} - 4\pi M_s \tag{5.2}$$

where H_s is the saturation field for the IP configuration and can be obtained from the IP VSM loops such as the one shown in Fig. 5.1(a). The last column in Table 5.2 gives the H_c values obtained from the OOP hysteresis loops, including those shown in Figs. 5.1(b), 5.1(e), 5.1(f), 5.1(g), and 5.1(h).

Note that each $4\pi M_s$ value in Table 5.2 was obtained by simply averaging the $4\pi M_s$ values measured with the positive and negative fields, while the corresponding error bar is the difference of the two $4\pi M_s$ values divided by two. The H_k and H_c values and the corresponding errors were obtained with the same method.

Three main results are evident from the data in Table 5.2. First, the $4\pi M_s$ value of the 12-nm YIG film almost perfectly agrees with that of the bulk value in YIG crystals, which is 1750 G, but the values for the thinner films are smaller than the bulk value; a general trend is present in which $4\pi M_s$ decreases with a decrease in t. These observations indicate that the very thin films

have low quality, possibly due to lattice mismatching and diffusion at the interfaces, and the film quality is gradually improved as t increases from 4 nm to 12 nm.

Second, the 6-nm YIG film shows the highest H_k, and H_k becomes smaller if t is either smaller or larger. This response likely results from the co-existence of two distinct effects: with an increase in t, the film quality becomes better as evident from the $4\pi M_s$ data in the second column, while the PMA becomes weaker due to strain relaxation. In other words, H_k is relatively small in very thin films (4-5 nm) because of the low film quality and is also small in relatively thick films (10-12 nm) due to the strain relaxation.

Third, the H_c data show the exact same trend as the H_k data, namely, that H_c is the largest for the 6-nm film and decreases if t is either reduced or increased. This consistency supports the validity of the observed H_k properties; in PMA films H_k generally dictates the domain nucleation and domain wall motion processes and thereby determines H_c.

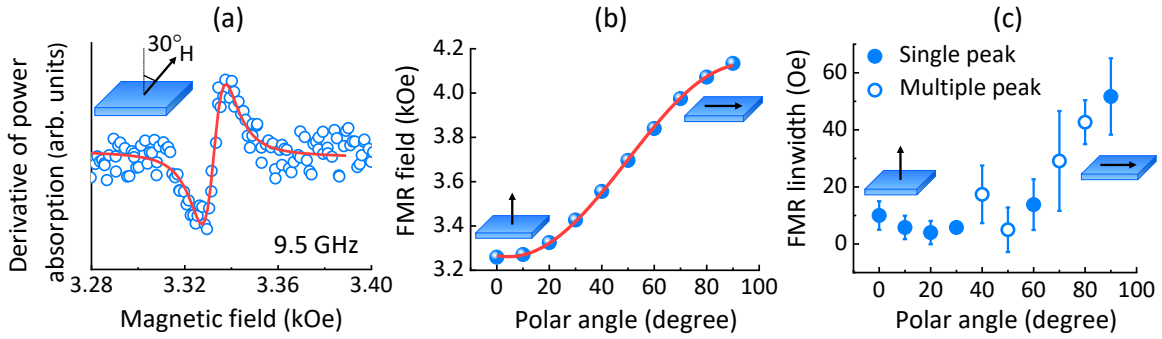

Figure 5.2. Polar angle (θ_H)-dependent ferromagnetic resonance (FMR) on a 10-nm-thick YIG film grown on a GSGG substrate. (a) An FMR profile measured at θ_H =30°. (b) FMR field as a function of θ_H. (c) FMR linewidth as a function of θ_H. The red curve in (a) is a fit to the derivative of a Lorentzian trial function. The red curve in (b) is a fit to Eq. (5.3).

Figure 5.2 presents the ferromagnetic resonance (FMR) data that further support the above-presented results on the PMA properties of the YIG films. The data were measured with a 9.5-GHz rectangular cavity on a 10-nm-thick YIG film for different field angles (θ_H) relative to the

film normal direction. Graph (a) shows a representative FMR profile measured at θ_H=30°. The blue circles show the data, while the red curve shows a numerical fit to the derivative of a Lorentzian trial function. The fitting yields the field (H_{FMR}) and peak-to-peak linewidth (ΔH_{pp}) of the FMR. At certain field angles, the FMR profiles consist of multiple resonances, rather than a well-defined single resonance; for such profiles, the fitting was carried out only for the narrow central portion of the main resonance. Graphs (b) and (c) show H_{FMR} and ΔH_{pp}, respectively, as a function of θ_H, which were obtained from the Lorentzian fitting. The red curve in graph (b) shows a fit to[117,118]

$$\left(\frac{f}{|\gamma|}\right)^2 = [H_{FMR}\cos(\theta_H-\phi_M)+(H_k-4\pi M_s)\cos(2\phi_M)]\cdot[H_{FMR}\cos(\theta_H-\phi_M)+(H_k-4\pi M_s)\cos^2(\phi_M)] \quad (5.3)$$

where $|\gamma|$ is the absolute gyromagnetic ratio, and ϕ_M is the angle of the equilibrium magnetization relative to the film normal direction that can be found according to

$$H_{FMR}\sin(\theta_H-\phi_M)-\frac{1}{2}(H_k-4\pi M_s)\sin(2\phi_M)=0 \quad (5.4)$$

The fitting yields H_{k}=2234.8±3.3 Oe and $|\gamma|$=2.80 MHz/Oe.

One can see two important results from the data in Fig 5.2. First, the fitting-yielded H_{k} value (2235 Oe) is consistent with the corresponding value (2263 Oe) in Table 5.2. This consistency evidently confirms the presence of the PMA in the film. Second, one has ΔH_{pp}≤10 Oe at low field angles. This suggests that the film has relatively low damping. The detailed discussions about the damping properties are presented in section 5.4.

In addition, one can also see that ΔH_{pp} increases with θ_H, which is likely due to the presence of two-magnon scattering in the YIG film. It is known that for magnetic thin films, two-magnon scattering is prohibited when θ_H=0, because of lacking degenerated spin-wave modes at the FMR

frequency (ω_{FMR}), but occurs and contributes to ΔH_{pp} when θ_H is nonzero and degenerated spin waves are present at ω_{FMR}[87,90] In principle, one can numerically fit the data in graph (c) to determine the contributions to ΔH_{pp} from the intrinsic damping and the two-magnon scattering process. Such an analysis, however, was not carried out in consideration of the presence of multiple FMR peaks for some field angles and the error bars being relatively large.

Two notes should be made about the data presented in Fig. 5.2. First, FMR measurements with microwave cavities are usually expected to yield FMR profiles with large signal-to-noise ratios (SNR), but the data in Fig. 5.2(a) appear to have a relatively small SNR. Possible reasons for this include the relatively low Q factor of the cavity and the aging of the diode detector used in the FMR measurements. Second, the presence of multiple FMR peaks is likely due to spatial inhomogeneity of the magnetic properties of the YIG films produced during the sputtering and annealing processes or induced by the strain.

5.3 Origin of PMA

The above-presented PMA originates from strain-induced magnetoelastic anisotropy, as discussed in Refs. [103,104,105]. Specifically, because the lattice constant of YIG materials (a_{YIG}=12.376 Å) is smaller than that of GSGG substrates (a_{GSGG}=12.554 Å), there exists a tensile strain in the (111) plane of a (111) YIG thin film grown on a (111) GSGG substrate. This in-plane (IP) tensile strain corresponds to an out-of-plane (OOP) compressive strain if one assumes that the volume of the YIG unit cells is conserved. Such interfacial lattice mismatching-produced strain can induce a perpendicular, uniaxial magnetoelastic anisotropy in the YIG film that can be described by Refs. [119]

$$K_u = \frac{3}{2}\lambda_{111}\sigma \tag{5.5}$$

where K_u is the anisotropy constant, λ_{111} is the magnetostriction constant along the (111) direction of the YIG, and σ is the uniaxial stress along the normal direction of the YIG film. Note that $\sigma > 0$ and $\sigma < 0$ correspond to a tensile stress and a compressive stress, respectively. The OOP compressive strain in the YIG films in this work gives rise to $\sigma < 0$. On the other hand, it is known that YIG materials have $\lambda_{111} = -2.4 \times 10^{-6}$ [104,105,120]. Thus, K_u is positive according to Eq. (5.5), and PMA is present in the YIG films grown on the GSGG substrates.

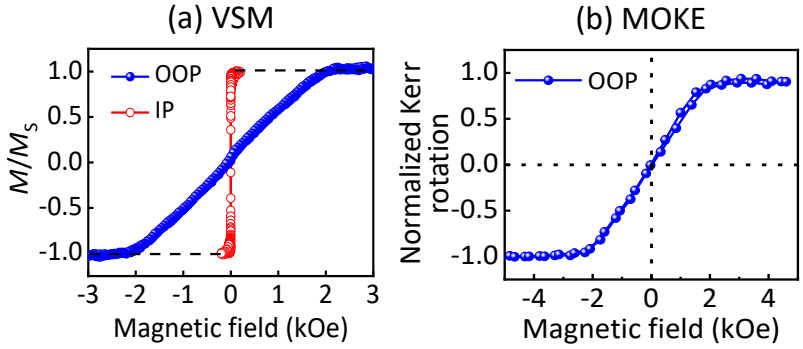

Figure 5.3. Magnetic hysteresis responses of a 6-nm-thick YIG film grown on a GGG substrate. (a) VSM data measured under an out-of-plane (OOP) field and an in-plane (IP) field. (b) Polar MOKE data measured under an OOP field.

Figures 5.3 and 5.4 present experimental data that support the above interpretation about the physical origin of the PMA in the YIG films. Figure 5.3 gives the VSM and MOKE data measured on a 6-nm-thick YIG film that was grown under the exact same conditions as the 6-nm YIG film cited in Fig. 5.1 and Table 5.2, but on a single-crystal (111) GGG substrate, rather than a GSGG substrate. The data show that the YIG film is much easier to magnetize for the field IP configuration than for the field OOP configuration. Further, the data for the OOP configuration show $H_c \approx 0.8$ Oe and $M_r/M_s \approx 0.3\%$, both substantially smaller than the corresponding values shown by the data in Fig. 5.1(b). These results are typical for YIG thin films grown on GGG substrates in which the lattice constants of the film and the substrate almost match each other, and lattice mismatching-produced strain is negligible. The comparison of the data in Fig. 5.3 with those in

Figs. 5.1(a), 5.1(b), and 5.1(c) evidently confirm that the substrate, rather than the growth condition or the film thickness, plays a critical role in the formation of the above-described PMA. Note that the field IP VSM data yield $4\pi M_s \approx 1722$ G, which is close to the bulk value of the YIG (1750 G).

Figure 5.4(a) presents the XRD spectra for five YIG thin films grown on GSGG substrates as well as a bare GSGG substrate. In each spectrum, the two main peaks are for the (444) peaks of the GSGG substrate. The appearance of the two (444) peaks results from the coexistence of the $K_{\alpha 1}$ and $K_{\alpha 2}$ components of the X ray. The vertical dashed line indicates the position or angle expected for the (444) peak of YIG crystals, while the short arrows indicate the actual positions of the (444) peaks of the YIG films.

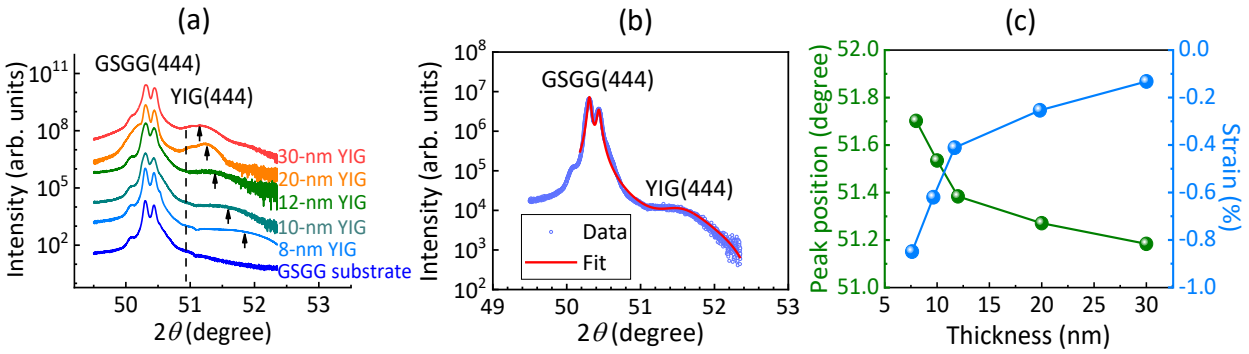

Figure 5.4. (a) X-ray spectra of YIG thin films grown on GSGG substrates. (b) X-ray spectrum of a 10-nm YIG film (blue circles) and its numerical fit (red curve). (c) Angles of (444) peaks (left axis) and out-of-plane strain (right axis) of YIG thin films grown on GSGG substrates.

The comparison of the spectra in Fig. 5.4(a) indicates that the YIG (444) peaks of the films appear on the right side of the dashed line. This result indicates the presence of an OOP compressive strain in the YIG films according to the Bragg's law for the XRD

$$2d \sin\theta = n\lambda \tag{5.6}$$

where d is the spacing between diffracting planes parallel to the film plane, θ is the incident angle of the X ray, n is an integer, and λ is the wavelength of the X ray. An OOP compressive strain

gives rise to a smaller d, while a decrease in d leads to an increase in θ, according to Eq. (5.6). In other words, a vertical compressive strain results in the appearance of the diffraction peak on the right side of the theoretical peak position.

The comparison of the XRD spectra in Fig. 5.4(a) also shows that the thicker the YIG film is, the closer the (444) peak is to the dashed line. This observation indicates that an increase in the film thickness gives rise to a weaker strain in the film. This result is consistent with the interfacial nature of the lattice mismatching-produced strain; such a strain relaxes partially as the film becomes thicker.

In fact, one can also use the XRD data in Fig. 5.4(a) to determine the (444) peak positions (2θ) of the YIG films and thereby estimate the strain (ε) in the YIG films. Figure 5.4(b) shows the numerical fitting of the XRD spectrum of the 10-nm-thick YIG film. The red curve is a profile that consists of three Viogt functions, one for the YIG (444) peak and the other two for the GSGG (444) peaks; the fitting yields $2\theta \approx 51.54°$ for the 10-nm film. Through such fitting, one can obtain 2θ values for all the YIG films.

Figure 5.4(c) presents the 2θ and ε values. The green symbols show 2θ as a function of the film thickness (t), while the blue symbols show the ε values as a function of t, evaluated according to

$$\varepsilon = \frac{d-d_0}{d_0} = \frac{\sin\vartheta_0 - \sin\vartheta}{\sin\vartheta_0} \tag{5.7}$$

where d_0 and θ_0 is the spacing and the peak position, respectively, expected for bulk YIG crystals. One can see that ε is negative, confirming the compressive nature of the strain in the YIG films. One can also see that the amplitude of ε decreases with an increase in t. This result, together with Eq. (5.5), suggests that the PMA in the YIG film should become weaker if t is increased. This trend is consistent with the overall trend shown in Table 5.2, namely, that both H_k and H_c decreases

when t is increased from 6 nm to 12 nm.

Three notes should be made about the above discussions. First, in addition to the magnetoelastic anisotropy described by Eq. (5.5), the YIG thin films are also expected to exhibit cubic magneto crystalline anisotropy. For YIG crystals, the cubic anisotropy constants are K_1=-6100 erg/cm^3 and K_2=-260 erg/cm^3. For a (111)-oriented YIG film, such a crystalline anisotropy gives rise to an easy-axis anisotropy along the film normal direction that can be described by an effective anisotropy field

$$H_k = \frac{2|K_1|}{M_s} + \frac{4|K_2|}{M_s} \tag{5.8}$$

If one takes the 6-nm YIG film as an example and uses the $4\pi M_s$ value presented in Table 2, one obtains an anisotropy field of about 135 Oe, which is only about 4% of the corresponding H_k value in Table 5.2. Thus, strictly speaking H_k in Eqs. (5.2) and (5.3) have two origins, a strain-induced magnetoelastic anisotropy and an intrinsic magneto crystalline anisotropy, but the latter is substantially smaller than the former and is therefore neglected in the analyses. The magneto crystalline anisotropy is also neglected in the discussions in the following sections for the same reason.

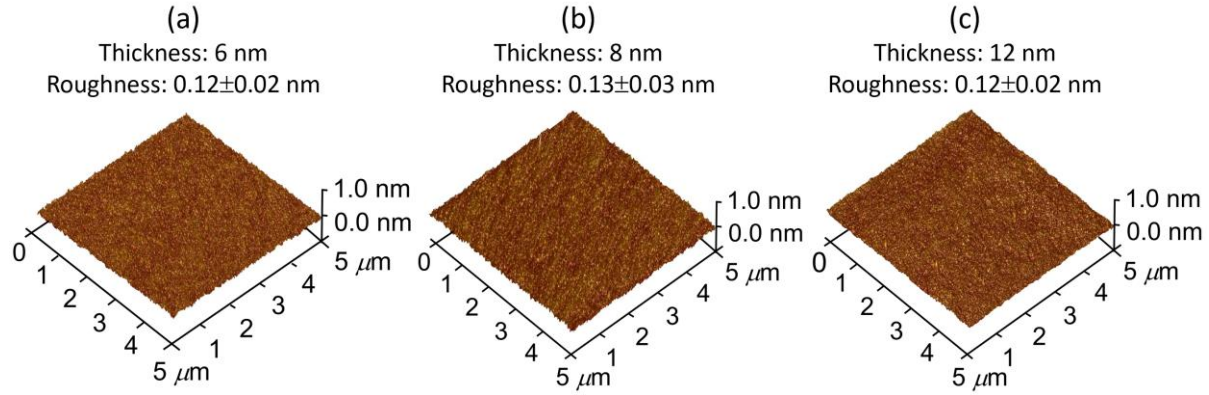

Figure 5.5. Atomic force microscopy surface images of YIG thin films of different thicknesses, as indicated. The films were grown on GSGG substrates.

Second, in spite of the strong dependence of ε, H_k, and H_c on t, all the PMA YIG films show smooth surfaces, with a rms surface roughness range of 0.11-0.13 nm. This result is important from the point of view of applications of PMA YIG thin films in spintronic devices. Figure 5.5 presents representative AFM images obtained on films of different thicknesses, as indicated. The roughness values given in the figure were obtained by averaging over AFM measurements on five different 5 μm × 5 μm areas on the YIG film, while the uncertainty for each roughness value is the corresponding standard deviation. One can see that the films all show smooth surfaces.

Finally, it should be mentioned that in the XRD spectra shown in Fig. 5.4(a) the YIG (444) peaks appear as broad, weak humps on the right shoulder of the strong GSGG (444) peaks. Those YIG peaks are clearly defined for thicker films (20-30 nm), are less defined for thinner films (8-12 nm), and cannot be detected for very thin films (4-6 nm). Future work is of interest that makes use of high-resolution XRD measurements and reciprocal space mapping analyses or high-resolution scanning transmission electron microscopy measurements to confirm the crystalline structure and analyze the strain properties in ultrathin PMA YIG films.

5.4 Damping constant of PMY YIG films

The dynamical properties of the PMA YIG films were determined through broadband vector network analyzer (VNA)-based FMR measurements. Figure 5.6 shows the measurement and analysis approaches. Figure 5.6(a) sketches the experimental setup, which consists mainly of a VNA and a coplanar waveguide (CPW). The CPW structure has a 50-μm-wide signal line and a signal line-to-ground spacing of 25 μm; its nominal impedance is 50 Ω. The PMA YIG sample, shown as a red disk in Fig. 5.6(a), is placed on the CPW with the YIG film side facing the CPW structure and the GSGG substrate side facing up. An external static magnetic field (H), shown as a blue arrow in Fig. 5.6(a), is applied perpendicular to the film plane to either magnetize the YIG

film to saturation or enable VNA-FMR measurements. The major measurement and data analysis procedures are as follows:

(i) Magnetize the YIG film to saturation with a large perpendicular magnetic field. For the data presented below, this field is 5 kOe.

(ii) Measure the transmission coefficient (S_{21}) of the CPW/YIG structure as a function of H at a fixed microwave frequency (f). Figure 5.6(b) presents representative S_{21} profiles measured on an 8-nm-thick YIG film at f=14 GHz.

(iii) Fit the S_{21} data with the theoretical S_{21} profiles[121,122] to determine the FMR field (H_{FMR}) and the FMR linewidth (ΔH). The curves in Fig. 5.6(b) show such fits. Note that ΔH here refers to "full width at half maximum" rather than the peak-to-peak linewidth.

(iv) Repeat (i)-(iii) for different microwave frequencies over 7-26 GHz.

(v) Plot H_{FMR} vs. f and then numerically fit the data using the Kittel equation

$$f = |\gamma|(H_{FMR} + H_k - 4\pi M_s) \tag{5.9}$$

as shown in Fig. 5.6(c). Note that in Fig. 5.6(c), the symbols show the data, while the line shows the fit. The fitting yields two values, $|\gamma|$ and $(H_k - 4\pi M_s)$, as indicated in Fig. 5.6(c).

(vi) Plot ΔH vs. f and then numerically fit the data using

$$\Delta H = \frac{2\alpha}{|\gamma|} f + \Delta H_0 \tag{5.10}$$

as shown in Fig. 5.6(d). In Eq. (5.10), α is the effective damping constant, and ΔH_0 denotes line broadening due to the spatial inhomogeneity of the YIG thin film. Note that in Fig. 5.6(d), the symbols show the data, while the line shows the fit. The fitting yields α and ΔH_0, as indicated in Fig. 5.6(d).

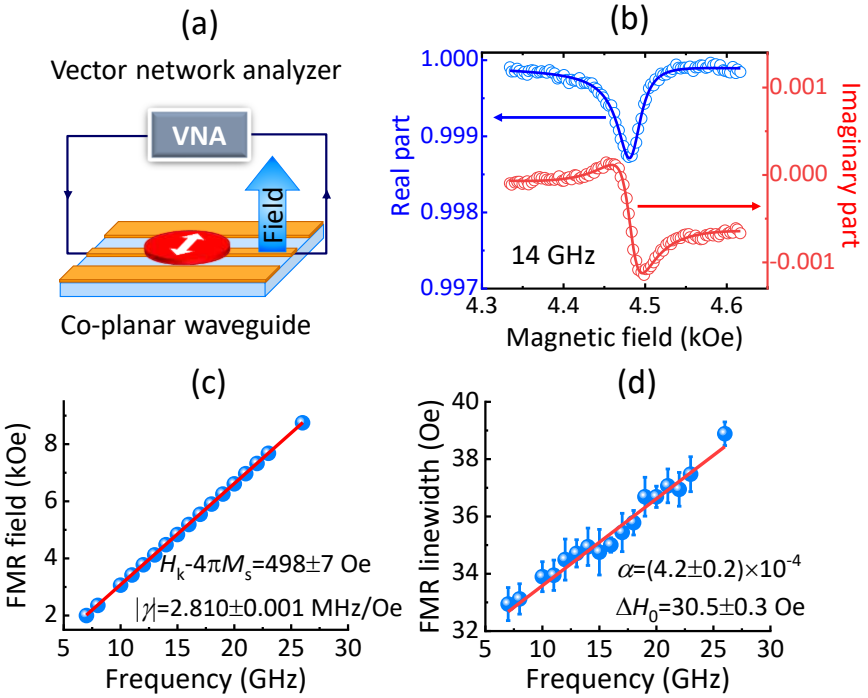

Figure 5.6. Vector network analyzer ferromagnetic resonance measurements on YIG thin films grown on GSGG substrates. (a) Experimental configuration. (b) Representative transmission coefficient (S_{21}) profiles, (c) FMR field as a function of microwave frequency (f), and (d) FMR linewidth as a function of f, measured on an 8-nm-thick YIG film. In (b)-(d), the symbols show the experimental data, while the curves and lines show numerical fits.

Two notes should be made about the FMR data shown in Fig. 5.6. First, the FMR profiles shown in Fig. 5.6(b) were obtained after averaging over five field-swept measurements. Second, only the ΔH data over 7-26 GHz were analyzed; the FMR measurements were also carried out at lower frequencies, but ΔH does not follow the linear trend shown in Fig. 5.6(d) and increases with a decrease in f. This linewidth enhancement at low frequencies results from the so-called "low-field loss" associated with demagnetization effects in not fully saturated films or propagation of "slow" electromagnetic waves along interfaces between magnetic thin films and non-magnetic substrates[123,124,125].

Table 5.3 presents the data obtained through the above steps. The first column lists the thicknesses (t) of the PMA YIG films. The second column gives the $H_k - 4\pi M_s$ values, which

are obtained from the numerical fitting such as that shown in Fig. 5.6(c). The third and fourth columns give the α and ΔH_0 values, respectively, obtained from the fitting such as that shown in Fig. 5.6(d).

Table 5.3. VNA-FMR data of PMA YIG thin films grown on GSGG substrates

Thickness t (nm)	**H_k-$4\pi M_s$ (Oe)**	**Damping constant α ($\times 10^{-3}$)**	**Inhomogeneity line broadening ΔH_0 (Oe)**
4	234.4 ±1.3	1.16 ± 0.02	10.4 ± 0.2
6	511.0 ± 2.1	0.47 ± 0.06	41.4 ± 0.6
7	372.4 ± 0.2	0.45 ± 0.09	13.6 ± 0.6
8	498.4 ± 7.1	0.42 ± 0.02	30.6 ± 0.3
12	440.8 ± 2.8	0.73 ± 0.02	39.1 ± 0.4

One can see three important results from the data in Table 5.3. First, the films with t=6-12 nm all exhibit relatively low damping, with α<0.001. The 4-nm film shows the largest damping, which is likely because the film has relatively low quality due to lattice mismatching and diffusion at the YIG/GSGG interface. Second, $H_k - 4\pi M_s$ is positive for all the films, which confirms the presence of strong PMA in the films. Third, there exists a correlation between $H_k - 4\pi M_s$ and ΔH_0, namely, that the films with low $H_k - 4\pi M_s$ values also exhibit low ΔH_0 values, vice versa. This suggests that the line broadening is mostly due to the spatial inhomogeneity of H_k, rather than $4\pi M_s$, in the YIG films.

Two notes should also be made about the data in Table 5.3. (1) The $H_k - 4\pi M_s$ values in Table 5.3 do not match those calculated using the data in Table 5.2. The major reason for this mismatching lies on the fact that the GSGG substrates for the YIG films cited in the two tables were obtained from different sources and thereby showed different lattice constants, resulting in a

difference in the strength of lattice mismatching-produced strain in the YIG films. Other possible reasons include errors in the field measurements and field misalignments during the measurements. (2) The 6-nm, 7-nm, and 8-nm films show very similar α values, but the 12-nm film shows a value which is about 60% higher. The reason for this difference is currently unknown.

Table 5.4 compares the lowest α value in Table 5.3 with the α values of other PMA thin films reported previously[65,126,127,128,129,130,131,132,133]. These values were all measured with OOP fields, namely, θ_H=0. The OOP field configuration was taken for two considerations: (1) two-magnon scattering is prohibited in the presence of an OOP field, but it can occur and contribute to ΔH, and thereby complicate the FMR data analysis if the field is not perpendicular to the film plane and (2) the OOP configuration is relevant for most device applications of magnetic films with perpendicular anisotropy.

Table 5.4. Summary of the damping constants (α) of PMA thin films reported previously.

Material	**Damping constant**	**Reference**
CoGd	0.1	[125]
Co	0.13	[126]
Co_2FeAl	0.008	[127]
$(Co/Ni)_n$	0.02	[128]
CoFeB	0.011	[129]
$Eu_3Fe_5O_{12}$	0.024	[130]
$Tm_3Fe_5O_{12}$	0.013	[131]
$Tm_3Fe_5O_{12}$	0.02	[132]
$Dy_{3-x}Ce_xFe_{5-y}Al_yO_{12}$	0.23	[133]
$Y_3Fe_5O_{12}$	0.00042	This work

It is evident from the data in Table 5.4 that the PMA YIG films have a damping constant lower

than other PMA films. This observation clearly suggests the merit of PMA YIG films for applications where low damping is essential. Specifically, α in the PMA YIG film is more than 20 times smaller than that in CoFeB thin films[129] and more than 40 times smaller than that in $(Co/Ni)_n$ superlattices[128]. Note that CoFeB and $(Co/Ni)_n$ films are both among the most common PMA thin films in previous studies.

Two points should be mentioned about the data shown in Table 5.4. First, the table serves to provide an overview of the damping properties of various PMA thin films in recent studies, and a rigorous comparison of the listed α values may be inappropriate because the actual α value also depends on (1) the FMR measurement technique, and (2) the data analysis approach, in particular, when multiple peaks appear in the FMR profiles. Second, a recent article reported $\alpha=3\times10^{-4}$ for a Bi-doped YIG PMA film[93], which is not included in Table 5.4 since only un-doped YIG films are included in the table. This α value was obtained only for a particular field angle, which is $\theta_H\approx60°$; in the presence of an OOP field, the film showed $\Delta H \approx1600$ Oe ($\Delta H_{pp}\approx950$ Oe), which is notably larger than many of the values reported previously for PMA thin films[127,128,129,130,131,132].

5.5 Spin-orbit-torque-induced magnetization switching

The above-presented YIG films with both PMA and low damping may find broad applications in spintronic devices. As an example, this section demonstrates spin-orbit torque (SOT)-induced switching of magnetization in a YIG/Pt bi-layered Hall bar device. The purpose of this demonstration is to illustrate the device application possibility of the YIG films described in the prior sections, while the switching mechanism is exactly the same as in previous works on YIG/Pt[105], $BaFe_{12}O_{19}$/Pt[134], and $Tm_3Fe_5O_{12}$/Pt[110] bi-layered structures.

Figure 5.7 shows the experimental configuration and representative experimental data.

Figure 5.7(a) presents a photo of the measurement device and the electrical measurement configuration. The core component is a Hall bar structure made of an YIG(6 nm)/Pt(5 nm) bi-layer. The Pt layer was grown on the YIG film by DC sputtering at room temperature. The Hall bar device was fabricated through photolithography and argon ion milling processes. The central area of the Hall bar is 30 μm long and 10 μm wide. The contact leads of the Hall bar are made of a 200-nm-thick Au film; prior to the deposition of the Au film, a 4-nm-thick Ti adhesion layer was deposited. As for the Pt layer, both the Ti and Au layers were grown by DC sputtering at room temperature. The connections to the Au leads were made through wire bonding using Au wires under a microscope. The configuration shown in Fig. 5.7(a) allows for the measurement of the Hall resistivity (ρ_H) of the YIG/Pt Hall bar device. Figures 5.7(b) and 5.7(c) present the measured ρ_{AHE} vs. H hysteresis responses for an out-of-plane (OOP) field and an in-plane (IP) field, respectively. For the OOP configuration, ρ_H has two components, ρ_{OHE} and ρ_{AHE}. Figure 5.7(b) shows only ρ_{AHE}; ρ_{OHE} scales linearly with H and has already been subtracted. Figure 5.7(c) also shows ρ_{AHE} only; ρ_{OHE} is zero in the IP configuration. Note that the data in Fig. 5.7(b) are the same as those in Fig. 5.1(d).

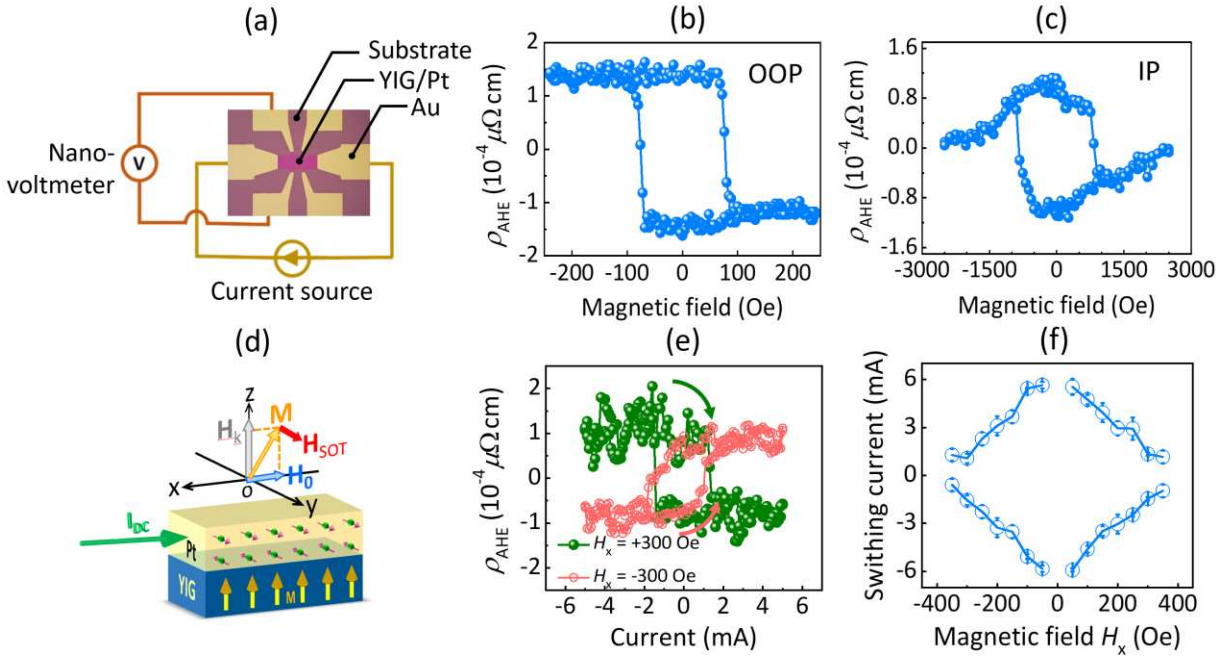

Figure 5.7. Spin-orbit torque (SOT)-induced magnetization switching in a YIG(6nm)/Pt(5nm) bi-layered structure. (a) Experimental configuration. (b) Anomalous Hall effect (AHE) resistivity (ρ_{AHE}) measured as a function of an out-of-plane (OOP) field using the configuration shown in (a). (c) ρ_{AHE} measured as a function of an in-plane (IP) field using the configuration in (a). (d) A schematic diagram for SOT switching in the YIG/Pt structure. (e) ρ_{AHE} as a function of the DC current (I_{DC}) in the Pt layer for two different external fields (H_x), as indicated. (f) A switching current vs. in-plane external field phase diagram.

The data in Figs. 5.7(b) and 5.7(c) clearly show that the AHE response differs for different field configurations. This is because ρ_{AHE} in the Pt layer scales with the perpendicular component ($M_\perp$) of the magnetization in the YIG film. Note that the origin of ρ_{AHE} in the non-magnetic Pt layer is discussed in section 5.3. In the OOP configuration, a sweep in H results in a switching between $M_\perp>0$ and $M_\perp<0$, giving rise to a square-like loop response shown in Fig. 5.7(b). In contrast, in the IP configuration, $|M_\perp|$ takes the maximum when H=0, due to PMA, but it gradually reduces to zero when the IP field is increased and gradually rotates the magnetization vector from the perpendicular direction to the plane of the YIG film, giving rise to a distorted loop with $\rho_{AHE}\approx0$ at high fields, as shown in Fig. 5.7(c). Note that the fields at which ρ_{AHE} takes zero in Fig. 5.7(c) are almost the same as the fields at which the magnetization takes the saturation

value in Fig. 5.1(c). Thus, it is evident that one can probe the magnetization status in the YIG film, namely, $M_\perp>0$ vs. $M_\perp<0$, by simply measuring ρ_{AHE} in the Pt layer.

Figure 5.7(e) presents the ρ_{AHE} data that demonstrate current-induced magnetization switching. The data were measured as a function of a DC current (I_{DC}) applied to the Pt layer of the Hall bar. The duration of the DC current is 1 ms. Right after the DC current is switched off, a small alternating current of 0.4 mA is applied to the Hall bar and a Hall voltage is measured, using the measurement configuration shown in Fig. 5.7(a). During the measurements, an IP field was applied along the x axis. This field (H_x) serves to ensure deterministic switching, as in previous work[110,134,135,136]. The field also assists SOT switching, as discussed shortly. The two sets of data in Fig. 5.7(e) were obtained with opposite H_x fields, as indicated.

The data in Fig. 5.7(e) clearly show that a sweep in I_{DC} leads to a flip in the sign of ρ_{AHE}, which indicates current-induced magnetization switching. The data also show that the hysteresis loop evolves in an opposite manner when the IP field (H_x) flips its sign. This result has been observed previously and is a common feature of the SOT switching[110,134,135,136].

The switching mechanism is illustrated schematically in Fig. 5.7(d). As a charge current flows in the Pt layer, it generates, via the spin Hall effect[137,138], a pure spin current that flows along the Pt thickness direction or the z axis and is polarized along the y axis. This spin current in the Pt layer can transfer spin into the YIG film via so-called *s-d* exchange interactions at the YIG/Pt interface. The net effect is a torque, often called a spin-orbit torque (SOT), and a corresponding effective field ($\mathbf{H}_{SOT}$) that exert on the magnetization vector ($\mathbf{M}$) in the YIG film and switch it between the up and down directions. For the diagram shown in Fig. 5.7(d), $\mathbf{M}$ is initially pointing up; the SOT field, with the help of the external field ($\mathbf{H}_0$), rotates $\mathbf{M}$ from the up direction to the down direction, resulting in a switching of $\mathbf{M}$. This switching manifest itself as a change in the

sign of ρ_{AHE}, as shown in Fig. 5.7(e).

Based on the ρ_{AHE} data in Fig. 5.7(e), one can also determine the switching current, which is about 1.35 mA. This current corresponds to a current density of about 4.5 MA/cm^2. Previous works reported current densities of 10.9 MA/cm^2 for $BaFe_{12}O_{19}$/Pt[134], 18 MA/cm^2 for $Tm_3Fe_5O_{12}$/Pt[110], and 30 MA/cm^2 for YIG/Pt[105]. A rigorous comparison of these switching current densities is not very meaningful as the switching current strongly depends on the strength of PMA in the magnetic layer, the thicknesses of the magnetic and Pt layers, and the magnitude of the IP field (H_x), but the fact that those densities share the same order of magnitude indicates that the interfacial spin transfer in the YIG/Pt system in this work is as efficient as in the bi-layered systems reported previously[105,110,134].

Figure 5.7(f) gives the switching phase diagram where the vertical and horizontal axes show the switching current and the IP field, respectively, both along the *x* axis, as shown in Fig. 5.7(d). The data were obtained through the switching measurements similar to those described above for the data in Fig. 5.7(e). This phase diagram tells the charge current (or the magnetic field) required to switch **M** in the YIG film when a constant field (or a constant current) is applied. Note that each point in Fig. 5.7(f) shows the average over ten measurements, and the error bars in Fig. 5.7(f) show the corresponding uncertainties for the averaging. One can see that if a higher field is applied, a smaller current is required to realize the switching. This is consistent with the above-described switching mechanism.

Several remarks should be made about the SOT switching presented in Fig. 5.7. First, it is believed that the above-discussed switching was realized through domain wall motion, rather than magnetization rotation, as in previous switching studies[110,134,136]. This is because the device dimension (30 μm×10 μm) is relatively large compared with the exchange coupling length of

CoFeB (about 5 nm). Future work is of interest that uses a MOKE microscopy technique[92,139,140] to confirm this. Second, it is generally accepted that the damping of a PMA film does not affect the current density needed for SOT-induced rotational magnetization switching in the PMA film. In this work, however, the damping is relevant because the switching is realized through domain nucleation and domain wall motion, as mentioned above. Third, the ρ_{AHE} values in Fig. 5.7(e) are smaller than those in Fig. 5.7(b). This observation likely results from the fact that the external field was applied IP for the measurements of the data shown in Fig. 5.7(e) but was applied OOP for the measurements of the data in Fig. 5.7(b). Finally, the switching response shown in Fig. 5.7(e) for H_x=-300 Oe seems to be less sharp than that for H_x=-300 Oe. This difference is unexpected, and one possible reason is that the AHE in the YIG/Pt bilayer is weak and the AHE signals are noisy.

5.6 Conclusions and outlook

In summary, the work presented in this chapter demonstrates the feasibility of development of YIG thin films that are nm-thick, exhibit strong PMA, show nearly square magnetic hysteresis loops, and have a damping constant lower than other PMA thin films.

The films in the 4-9 nm thickness range showed (1) smooth surfaces, with an rms surface roughness of about 0.12 nm, (2) strong PMA, with an effective PMA field in the range of 2400-3400 Oe, and (3) square-like hysteresis loops, with a remnant-to-saturation magnetization ratio in the range of 86-98%. The growth of a heavy metal layer on the top of a YIG film and patterning of mm-sized YIG films into μm-sized elements did not result in the degradation of PMA in the film.

The comparison of the structural and magnetic properties of the PMA YIG films with those of the control samples clearly indicates that the PMA originates mainly from magnetoelastic

anisotropy associated with a compressive strain along the film thickness direction; such a strain is induced by the lattice mismatching between the YIG films and the GSGG substrates. There exists also cubic magneto crystalline anisotropy in the YIG films, but its contribution to the PMA is considerably smaller than the strain-induced magnetoelastic anisotropy.

The films showed a damping constant (α) lower than other PMA thin films. For the films with a thickness of 6-8 nm, α ranges from $(4.2\pm0.2)\times10^{-4}$ to $(4.7\pm0.6)\times10^{-4}$. These values represent the lowest damping constants measured on magnetic nm-thick films with perpendicular anisotropy under perpendicular fields.

Current-induced switching of the magnetization in PMA YIG thin films was realized with a YIG/Pt Hall bar structure. The switching made use of a spin-orbit torque (SOT) that was produced through the spin Hall effect in the Pt layer. This work demonstrates the feasibility of the use of spin currents in a neighboring material, such as a heavy metal or a topological insulator, to manipulate the magnetization in PMA YIG films.

The low-damping PMA YIG films demonstrated in this work may have important applications in spintronic devices. It should be highlighted that the films were deposited by sputtering, which is an industry-friendly thin film growth technique. In terms of potential device applications of PMA YIG films, the following future works are of great, immediate interest. (1) Optimization of the growth processes for the realization of PMA YIG films with even lower damping. The work presented in the last chapter demonstrates the development of nm-thick YIG films with sputtering that showed a damping constant as low as about 5.2×10^{-5} [11], which indicates the possibility of sputtering growth of PMA YIG films with $\alpha<4.2\times10^{-4}$. (2) Measurements of speed of SOT-induced domain wall motion in PMA YIG thin films. In general, the speed of domain wall motion is inversely proportional to α[141], so domain walls in YIG thin films are expected to move faster

than in other PMA thin films. This work is of significance for the development of racetrack memory. (3) SOT-induced precessional motion or switching of magnetization in nanoscale PMA YIG elements with single domains. Such studies will provide important implications for potential applications of PMA YIG films in spin-torque nano-oscillators and STT memory.

This work is published on Physical Review Applied 14, 014017 (2020). The full author list is Jinjun Ding, Chuanpu Liu, Yuejie Zhang, Uppalaiah Erugu, Zhiyong Quan, Rui Yu, Ethan McCollum, Songyu Mo, Sheng Yang, Haifeng Ding, Xiaohong Xu, Jinke Tang, Xiaofei Yang, and Mingzhong Wu. Jinjun Ding prepared the YIG films. Chuanpu Liu performed FMR measurements. Yuejie Zhang performed XRD measurements. Uppalaiah Erugu helped with AHE measurements. Zhiyong Quan preformed X-ray reflectivity (XRR) and ellipsometry measurements, Rui Yu helped with optimization of sputtering process, Ethan McCollum helped with VSM measurements, Songyu Mo and Sheng Yang helped with MOKE measurements.

CHAPTER 6 TOPOLOGICAL SURFACE STATES-CAUSED LARGE DAMPING ENHANCEMENT IN DIRAC SEMIMETAL-FERROMAGNETIC METAL LAYERED STRUCTURES

6.1 Introduction

The phenomenon of spin pumping refers to the transfer of spins from precessional moments in a ferromagnet to a non-magnetic material.[16,17] The origin of spin pumping is the magnon-electron interaction at the interface of the bilayer. In a ferromagnetic/non-magnetic bi-layered system, spin pumping manifests itself as two distinct effects: (1) an enhancement in the damping in the ferromagnetic layer and (2) a pure spin current in the non-magnetic layer. These effects are usually weak if the non-magnetic layer is a metallic thin film with weak spin-orbit coupling (SOC), such as Cu and Al, as there exists a strong spin backflow. The effects, however, can be very strong if the non-magnetic layer is a heavy metal thin film with strong SOC, such as Pt and W, because such a film can work as a spin sink, giving rise to a very weak spin backflow. [4,142,143] The effects can be even stronger if the non-magnetic component is a topological insulator (TI), such as Bi_2Se_3 and SmB_6; a TI can efficiently convert a spin current to a charge current and thereby serve as a very efficient spin absorber due to the intrinsic spin-momentum locking of the

topological surface states.[55,144,145,146,147]

Topological surface states (TSS) should also be present in other topological materials, such as Dirac semimetals and Weyl semimetals, when being interfaced with topologically trivial materials, due to the difference in the band topologies of the two types of materials. These TSS are also expected to exhibit spin-momentum locking due to the broken inversion symmetry at the interface. As such, one may also expect strong spin pumping in layered Dirac semimetal/ferromagnet systems.

This chapter reports on the experimental observation of strong spin pumping in a ferromagnetic thin film due to TSS in a neighboring Dirac semimetal α-Sn thin film. Unstrained α-Sn is a zero-gap semiconductor in which the conduction and valence bands have quadratic band touching at the Γ point at the Fermi level. This band touching is protected by the cubic symmetry of the α-Sn structure. When the cubic symmetry is broken by a tensile strain along [001] or [111], the two bands cross each other near the Fermi level, forming two Dirac points and giving rise to a topological Dirac semimetal (TDS) phase.[34,49,50] Such band crossing is protected by the rotational symmetry that remains unbroken by the strain.

In this work, TDS α-Sn thin films are realized using InSb substrates. The lattice constant of α-Sn (a=6.489 Å) is slightly larger than that of InSb (a=6.479 Å), and this lattice mismatching gives rise to an in-plane compressive strain or a perpendicular tensile strain in the α-Sn films.[148,149] The work made use of layered α-Sn(6nm)/Ag(2nm)/NiFe(20nm) structures where the NiFe film is ferromagnetic, and the non-magnetic Ag layer works as a spacer to physically separate α-Sn and NiFe and thereby avoid the suppression of TSS in α-Sn by the magnetic ordering in NiFe. The damping in these structures is found to be about a factor of 4.8 bigger than in the bare NiFe film. Measurements on control samples indicate that this damping enhancement is mostly due to the

TSS in the α-Sn, rather than the bulk of the α-Sn film or the Ag spacer; it is absent in β-Sn(6nm)/Ag(2nm)/NiFe(20nm) where the Sn film is topologically trivial.

Three important points should be highlighted. First, the topological Dirac semimetal (TDS) is a relatively newly-discovered topological phase; in comparison with other known TDS materials,[150,151,152,153] α-Sn is more appealing because (i) it is a single-element material and is therefore relatively easy to grow and (ii) it can transform into other topological phases, such as a TI and a Weyl semimetal, under certain strains or magnetic fields. Second, this work suggests that TDS materials may be as promising as TI materials in terms of applications in spintronics. For example, they can be used to achieve efficient magnetization switching, as presented in Chapter 7. Third, the α-Sn films in this work were grown by sputtering, which is an industry-friendly thin film growth technique.

6.2 Growth of α-Sn thin films

The α-Sn films were grown on single-crystal (001) InSb substrates by DC sputtering. The InSb substrates are rinsed sequentially with acetone, isopropyl alcohol, and DI water, before being loaded into the sputtering chamber. Prior to sputtering, the chamber has a base pressure of 2.0×10^{-8} Torr; substrate biasing is performed that includes several cycles of Ar ion sputtering of the substrate surface and post annealing of the substrate at 250 °C. The film deposition is carried out at room temperature, at a rate of about 2 nm/min. The sputtering power is set to as low as 15 W, in order to minimize the heating effect during the deposition. The film thickness is determined through X-ray reflection and atomic force microscopy (AFM) measurements. The major substrate biasing and sputtering control parameters are summarized in Table 6.1.

Table 6.1. Substrate biasing and sputtering control parameters for Sn film growth.

Substrate biasing	Ar ion sputtering	30 W, 2 min
	Annealing	250 °C, 60 min
	Cycles	3
Sputtering	Target-to-substrate distance	6.8 cm
	Sample holder rotation rate	10 rpm
	Ar pressure	6 mTorr
	Ar flow	6 sccm
	Sputtering power	15 W

6.3 Surface morphological and structural properties

Tin (Sn) exists in two major crystalline forms: α and β. α-Sn is a zero-gap semiconductor with a face-centered diamond cubic crystal structure. At high temperature, α-Sn transforms into β-Sn that is metallic and has a body-centered tetragonal structure. For commercially pure α-Sn bulk materials, this phase transformation occurs at 13.2±0.1 °C.[47] For α-Sn thin films, however, the transformation temperature can be significantly higher and usually increases with a decrease in the film thickness. For example, previous work has demonstrated that α-Sn films of a thickness of 50 monolayers grown on (111) InSb substrates are stable up to about 160 °C, while films of a thickness of 8 monolayers are stable up to about 200 °C.[48] This enhanced stability is due to the substrate. Specifically, α-Sn has a cubic structure with a lattice constant close to that of the (111) InSb substrate, while β-Sn has no threefold rotation axis. As a result, the growth of an α-Sn thin film on a (111) InSb substrate is more favorable, although β-Sn is generally more stable at room temperature.

Figure 6.1 shows the X-ray diffraction spectra of an InSb/Sn(8 nm) sample and an InSb/Sn(18 nm) sample, which were prepared under the same conditions. One can clearly see that the α-Sn (400) peak is much more resolved in the 8-nm film than in the 18-nm film, indicating that the α phase in the 8-nm film is more dominant than that of β phase. This difference is associated with the above-described, substrate-enhanced stability.

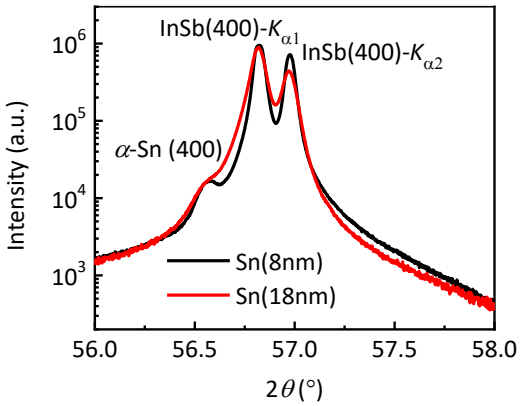

Figure 6.1. X-ray diffraction spectra of InSb/Sn(8 nm) and InSb/Sn(18 nm).

Figure 6.2 presents the structural properties of an 8-nm-thick α-Sn film. Figures 6.2(a) and 6.2(b) give a wide-angle X-ray diffraction (XRD) spectrum and a fine-scan XRD spectrum, respectively. The dotted and dashed lines in Fig. 6.2(b) indicate the expected positions for the α-Sn (400) and InSb (400) peaks, respectively. The red curve in Fig. 6.2(b) is a fit that consists of three Viogt functions: one for the α-Sn (400) peak and the other two for the InSb (400) peaks. Figure 6.2(c) shows an AFM surface image; the indicated roughness value is determined by averaging over the AFM measurements on five different 5 μm × 5 μm areas; the uncertainty is the corresponding standard deviation.

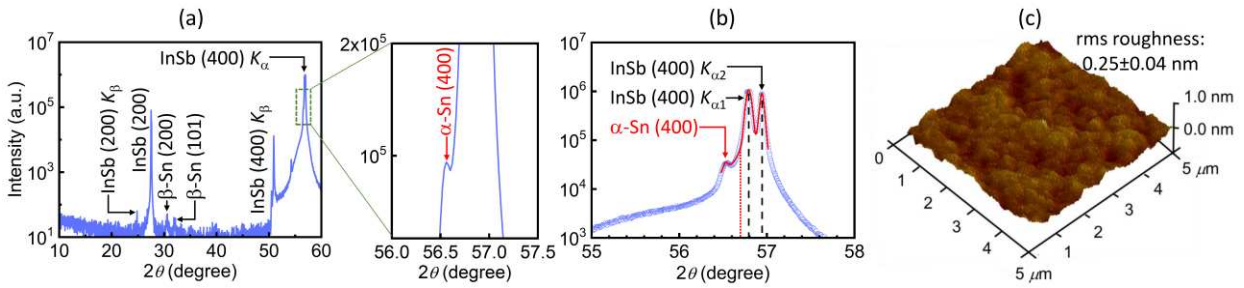

Figure 6.2. Properties for a 8-nm-thick α-Sn film grown on a (100) InSb substrate. (a) X-ray diffraction spectrum (XRD). (b) Fine-scan XRD spectrum. (c) Atomic force microscopy surface image.

Four results are evident from the data in Fig. 6.2. (1) Although α-Sn and β-Sn coexist, the α phase is overwhelmingly dominant than the β phase; the α-Sn (400) peak has an intensity three orders of magnitude stronger than the β-Sn (200) peak. (2) There is only one peak for the α-Sn, indicating the highly epitaxial growth of the film. (3) The α-Sn (400) peak appears on the left side of the expected peak position, which indicates the presence of a perpendicular tensile strain in the film. This is consistent with the expectation — the α-Sn film grown on the InSb substrate should exhibit an in-plane compressive strain because the lattice constant of α-Sn is slightly larger than that of InSb. [148,149] The Viogt fitting yields a=6.489±0.005 Å for the α-Sn film, which corresponds to a tensile strain of (0.27±0.08)%. Such a strain makes the α-Sn film a TDS. (4) The film has a very smooth surface, which facilitates the fabrication of layered heterostructures with high-quality interfaces for spin-pumping studies.

6.4 Damping enhancement in α-Sn/Ag/NiFe layered structures

The TSS of the TDS α-Sn film concerned in this work originates from the band inversion – the conduction and valence bands (Γ_8^+) near the Fermi level are derived from p electrons while the s-derived band (Γ_7^-) is below the Fermi level, as sketched in Fig. 6.3(a), unlike other group-IV semiconductors with the diamond structure such as Si and Ge. The Γ_7^- band is pushed below

the Fermi level mainly due to the scalar relativistic effects that affect the *s* electrons.[51,52] The TSS bridge the Γ_8^+ conduction band and the Γ_7^- valence band, as indicated by the red dashed lines in Fig. 6.3(a).

Figure 6.3 shows the main results of this work. Figure 6.3(a) illustrates the spin-pumping process in an α-Sn/Ag/NiFe tri-layered structure. In brief, a microwave magnetic field (**h**) can drive the magnetization (**M**) in the NiFe film to precess around the static field (**H**); this precession can pump a spin current that flows across the Ag spacer and then enters the α-Sn film.[15,16,17] Due to spin-momentum locking of the TSS, the α-Sn film can work as a highly-efficient spin absorber, leading to a very weak spin backflow; the net effect is an additional damping to the damping (α_0) of the NiFe film. Such damping enhancement is evidently indicated by the ferromagnetic resonance (FMR) data in Figs. 6.3(b), 6.3(c), and 6.3(d).

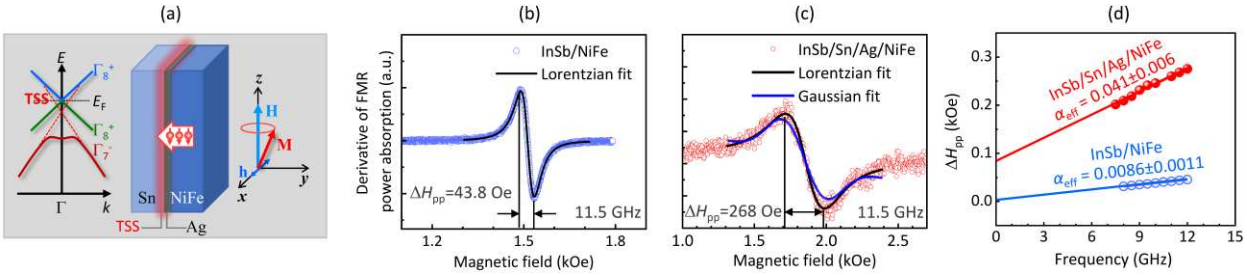

Figure 6.3. TSS-enhanced spin pumping in α-Sn/NiFe structures. (a) Conceptual diagram. (b) FMR profile of InSb/NiFe(20nm). (c) FMR profile of InSb/α-Sn(6nm)/Ag(2nm)/NiFe(20nm). (d) FMR linewidth as a function of frequency for the two samples.

Figures 6.3(b) and 6.3(c) show the FMR data measured on an InSb/NiFe(20nm) sample and an InSb/α-Sn(6nm)/Ag(2nm)/NiFe(20nm) sample, respectively, at a frequency of f=11.5 GHz with a X-band shorted waveguide. The symbols show the data, while the curves are fits to Lorentzian and Gaussian functions. The fitting-yielded peak-to-peak FMR linewidth (ΔH_{pp}) values are indicated. Note that the NiFe films in this work are 20-nm thick $Ni_{80}Fe_{20}$ alloy films; they were

grown with the same sputtering process.

The data in Figs. 6.3(b) and 6.3(c) show that the FMR in InSb/α-Sn/Ag/NiFe is significantly broader than that in InSb/NiFe. Specifically, ΔH_{pp} in InSb/α-Sn/Ag/NiFe is more than six times larger than that in InSb/NiFe. Further, Fig. 6.3(c) shows that the Lorentzian function fits the data much better than the Gaussian function, which indicates that the film inhomogeneity contribution to ΔH_{pp} is relatively small.[89] These results together suggest that a significant damping due to spin pumping is present in the sample with an α-Sn layer, as discussed shortly.

To confirm the above-discussed, α-Sn-produced linewidth broadening, the FMR measurements were repeated at nine different frequencies (f). The resulting ΔH_{pp} vs. f responses are shown in Fig. 6.3(d). One can see that ΔH_{pp} in the sample with α-Sn is larger at all frequencies, confirming the result shown in Figs. 6.3(b) and 6.3(c). The lines in Fig. 6.3(d) show fits to

$$\Delta H_{pp} = \frac{2\alpha_{eff}}{\sqrt{3}|\gamma|} f + \Delta H_0 \tag{6.1}$$

where α_{eff} is the effective damping constant, $|\gamma|$=2.8 MHz/Oe is the absolute gyromagnetic ratio, and ΔH_0 denotes the inhomogeneity-caused line broadening. The fitting-yielded α_{eff} values are indicated in the figure. One can see that α_{eff} in the sample with α-Sn is about 380% larger than that in the one without α-Sn.

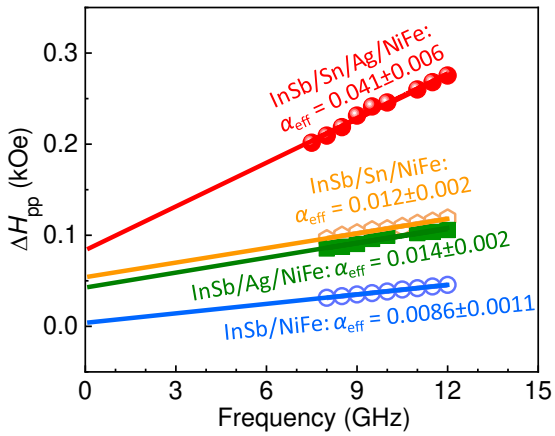

Figure 6.4. Comparison of FMR linewidth vs. frequency responses measured on four different samples, as indicated.

A strong damping enhancement in InSb/α-Sn/Ag/NiFe is evident from the data in Fig. 6.3. However, it is not solely due to the α-Sn film but also includes a contribution from spin absorption in the Ag spacer. Approximately, the damping in InSb/α-Sn/Ag/NiFe can be written as

$$\alpha_{eff} = \alpha_0 + \alpha_{Ag} + \alpha_{Sn} \tag{6.2}$$

where $\alpha_0 = 0.0086\pm0.0011$ is the damping in the NiFe film, and α_{Ag} and α_{Sn} denote the extra damping in the NiFe film due to the spin absorption in the Ag and Sn layers, respectively. From Eq. (6.2), one obtains $\alpha_{Ag} + \alpha_{Sn} \approx 0.0324$, but the weight of α_{Sn} in the overall damping enhancement is unclear.

In order to determine α_{Sn}, a control sample InSb/Ag(2nm)/NiFe(20nm) was fabricated using the exactly same substrate, targets, and sputtering process as for the InSb/α-Sn(6nm)/Ag(2nm)/NiFe(20nm) sample, and the same FMR measurements were conducted on this control sample. The green symbols in Fig. 6.4 show the measured data. The fitting yields $\alpha_{eff} = 0.014\pm0.002$. If one considers $\alpha_{eff} = \alpha_0 + \alpha_{Ag}$ in this sample, one obtains $\alpha_{Ag} \approx 0.0054$.

With α_{Ag} being determined, one can now use Eq. (6.2) to find $\alpha_{Sn} \approx 0.027$. Thus, one can

see that α_{Ag} is relatively small in comparison with α_0 in the NiFe film. This is consistent with the expectation, namely, that the Ag layer works as a poor spin sink or a good spin conductor because it has relatively weak SOC. It is for the same reason that Ag is chosen as a spacer material in this work. Note that the spin Hall angle in Ag is about 0.0068 only, while the spin diffusion length in Ag is about 700 nm,[154] which is much bigger than the Ag thickness in this work. In a stark contrast, α_{Sn} is remarkably bigger — it is more than 3 times bigger than α_0 and about 5 times bigger than α_{Ag}. This clearly indicates the presence of very strong SOC in the α-Sn film.

It is believed that the above-determined large α_{Sn} is mostly due to the two-dimensional TSS at the α-Sn/Ag interface, but there is also a possibility that α_{Sn} is associated with the SOC in the bulk of the α-Sn film. To check this possibility, a control sample InSb/α-Sn(6nm)/NiFe(20nm) was prepared using the exact same growth conditions as the InSb/α-Sn(6nm)/Ag(2nm) /NiFe(20nm) sample. It is expected that the α-Sn TSS in this control sample are suppressed or damaged due to direct physical contact with the NiFe film. Previous experimental and theoretical works have shown that the magnetic ordering in a ferromagnetic metal can significantly modify and even completely suppress TSS in a neighboring TI.[155,156,157,158]

The orange symbols in Fig. 6.4 present the ΔH_{pp} vs. f data measured on the InSb/α-Sn/NiFe control sample in which TSS are expected to be absent. The fitting yields $\alpha_{eff} = 0.012 \pm 0.002$, which indicates $\alpha_{Sn} \approx 0.0034$. Thus, one can see that α_{Sn} in InSb/α-Sn/NiFe (0.0034) is only about 13% of that in InSb/α-Sn/Ag/NiFe (0.027). This big difference evidently shows that the large α_{Sn} in InSb/α-Sn/Ag/NiFe is mostly due to the TSS, while the bulk contribution is relatively small.

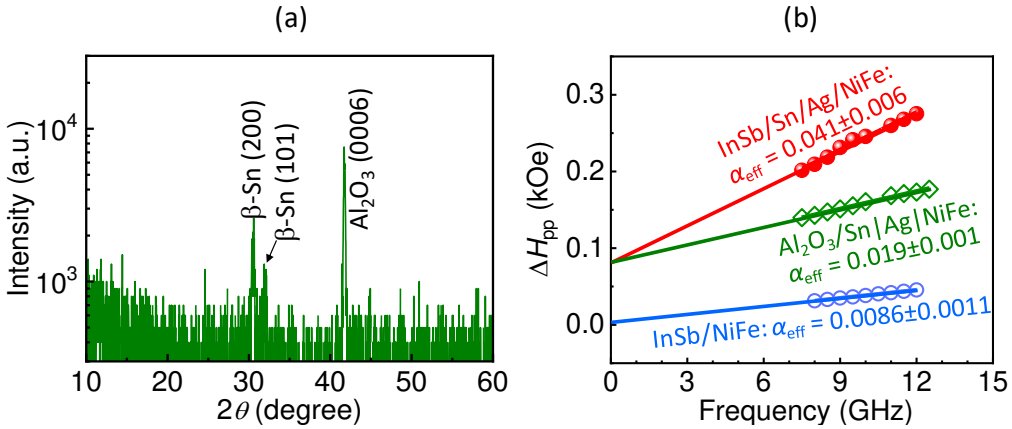

Figure 6.5. (a) XRD spectrum of an 8-nm-thick β-Sn film grown on a (0001) sapphire substrate. (b) Comparison of the FMR linewidth vs. frequency responses of the Al_2O_3/Sn(6nm)/ Ag(2nm)/NiFe(20nm) sample and the other two samples.

It should be highlighted that the topological nature of the α-Sn film plays a critical role in the above-presented strong damping enhancement. To demonstrate this role, a control sample Al_2O_3/Sn(6nm)/Ag(2nm) /NiFe(20nm) was fabricated using the exact same targets and sputtering conditions as for the InSb/α-Sn(6nm)/Ag(2nm)/NiFe(20nm) sample, but with a different substrate. Figure 6.5 shows the data on this control sample. The XRD spectrum in Fig. 6.5(a) shows that the Sn film grown on a (0001) sapphire substrate has β phase, rather than α phase. This results from the fact that the sapphire has a crystalline structure very different from the α-Sn, and the β-Sn film on the sapphire is more stable at room temperature. In Fig. 6.5(b), the green symbols show the ΔH_{pp} data of the Al_2O_3/Sn/Ag/NiFe sample. The fitting yields $\alpha_{eff} = 0.019 \pm 0.001$. Based on this value and Eq. (6.2), one obtains $\alpha_{Sn} \approx 0.005$. One can see that α_{Sn} in the sample with β-Sn is only about 17% of that in the sample with α-Sn. This agrees with the expectation — β-Sn is a topologically trivial material[159] and there exist no spin-momentum-locked TSS at the β-Sn/Ag interface, giving rise to weak spin absorption in the β-Sn.

In order to describe more quantitatively the strong spin absorption in α-Sn/Ag/NiFe, one can

define an effective spin mixing conductance $g_{\uparrow\downarrow}^{eff}$ as[160,161]

$$\mathrm{Re}\left(g_{\uparrow\downarrow}^{eff}\right) = \frac{4\pi M_s d}{g\mu_B}\left(\alpha_{eff} - \alpha_0\right) \tag{6.3}$$

where "Re" denotes the real part of $g_{\uparrow\downarrow}^{eff}$, $4\pi M_s \approx$ 7.84 kG is the saturation induction of the NiFe film, d=20 nm is the NiFe thickness, g=2.02 is the Landé factor, and μ_B is the Bohr magneton. The calculation using Eq. (6.3), $\alpha_0 = 0.0086$, and $\alpha_{eff} = 0.041$ yields $\mathrm{Re}\left(g_{\uparrow\downarrow}^{eff}\right)$ =2.7×10^{16} cm^{-2}. This value is about one order of magnitude larger than the values in systems where spin absorption is attributed to SOC in heavy metals[160] or at Rashba interfaces.[161] This large value is mostly due to the large spin absorption associated with the spin-momentum-locked TSS of the α-Sn. Note that a part of this large value may come from the film inhomogeneity. The presence of inhomogeneity-caused FMR linewidth broadening makes the extraction of $g_{\uparrow\downarrow}^{eff}$ challenging; it cannot be excluded that areas with slightly different $4\pi M_s$or anisotropy lead to different FMR fields and thereby make the derivation of $g_{\uparrow\downarrow}^{eff}$ from the slopes of the ΔH_{pp} vs. f responses less precise.

6.5 Magnetic properties of the magnetic films

Figure 6.6 presents in-plane (IP) and out-of-plane (OOP) magnetic hysteresis responses for five different samples: InSb/NiFe(20 nm), InSb/α-Sn(6 nm)/Ag(2 nm)/NiFe(20 nm), InSb/Ag(2 nm)/NiFe(20 nm), InSb/α-Sn(6 nm)/NiFe(20 nm), and Al_2O_3/Sn(6 nm)/Ag(2 nm)/NiFe(20 nm). All the data were measured at room temperature by a vibrating sample magnetometer (VSM). Table 6.2 summarizes the saturation induction $4\pi M_s$ values and saturation field H_s values of the

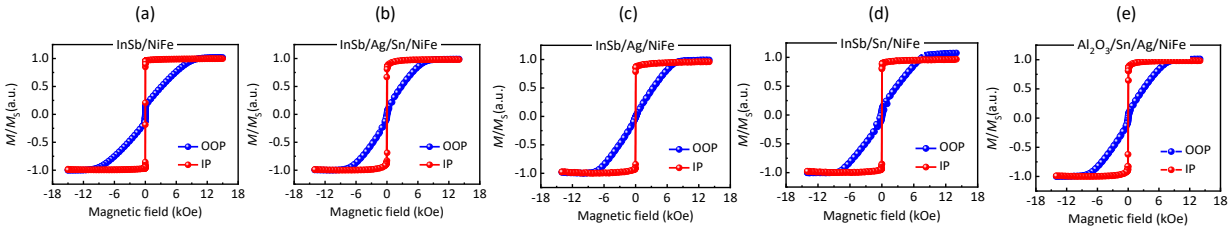

Figure 6.6. Magnetic hysteresis loops of five different samples, as indicated. The red and blue symbols present the data measured by an in-plane (IP) field and an out-of-plane (OOP) field, respectively.

five samples. The $4\pi M_s$ values were determined through dividing the IP saturated magnetic moment of each sample by the volume of the NiFe film. The H_s values were determined from the OOP hysteresis responses.

Table 6.2. Saturation induction ($4\pi M_s$) and saturation field (H_s) values of five samples.

Samples	**$4\pi M_s$ (G)**	**H_s (Oe)**
InSb/NiFe	9490±13	8596±199
InSb/Sn/NiFe	9065±31	7615±169
InSb/Ag/NiFe	7757±31	7007±202
Al_2O_3/Sn/Ag/NiFe	7875±86	7015±235
InSb/Sn/Ag/NiFe	7839±66	6780±241

In addition to the ΔH_{pp} values, the Lorentzian fitting shown in Figs. 6.3(b) and 6.3(c) also yield the ferromagnetic resonance (FMR) fields (H_{FMR}), which are presented in Fig. 6.7(a). The curves in the figure show the fits to the Kittel equation

$$f = |\gamma|\sqrt{H_{FMR}\left(H_{FMR} + 4\pi M_{eff}\right)} \tag{6.4}$$

where $4\pi M_{eff}$ denotes the difference between the saturation induction $4\pi M_s$ and the effective anisotropy field H_a of the NiFe film, namely, $4\pi M_{eff} = 4\pi M_s - H_a$. Note that $H_a > 0$ and $H_a < 0$ correspond to the presence of a perpendicular uniaxial anisotropy and an easy-plane

anisotropy, respectively. The fitting-produced $4\pi M_{eff}$ values are given in Fig. 6.7(b). Also presented in Fig. 6.7(b) are the $4\pi M_s$ values measured by a vibrating sample magnetometer

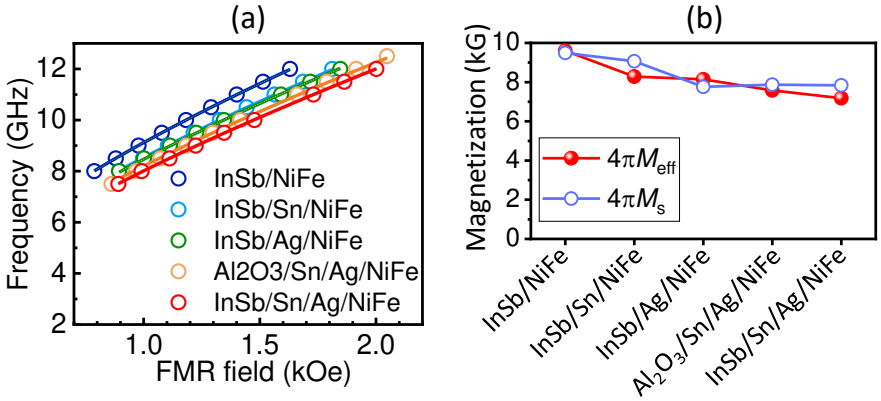

Figure 6.7. (a) Frequency vs. FMR field responses for five different samples. (b) Comparison of the $4\pi M_{\text{eff}}$ values from FMR measurements and the $4\pi M_{\text{s}}$ values from VSM measurements.

(VSM) under an in-plane field (see Table 6.2). The data indicate similar trends for $4\pi M_{eff}$ and $4\pi M_s$ — they both decrease from the left to the right. This suggests that the difference in the f vs. H_{FMR} responses of the different samples shown in Fig. 6.7(a) is mostly associated with the $4\pi M_s$ difference of the NiFe films and is therefore probably not due to the difference in the SOC strength in the non-magnetic layers adjacent to the NiFe films. With the data in Fig. 6.7(b), one can evaluate $H_a = 4\pi M_s - 4\pi M_{eff}$. The obtained H_a values are less than 9% of $4\pi M_s$. These values may suggest the presence of anisotropy in the NiFe film but may also result from the $4\pi M_s$ errors due to, for example, errors in estimating the volumes of the NiFe films. Future work is of interest that makes use of much thinner ferromagnetic films and angle-dependent FMR measurements to explore possible α-Sn-induced changes in H_{a}.

6.6 Conclusions and outlook

Two notes should be made about the data presented in Figs. 6.3-6.5. First, the damping in the NiFe film (0.0086) is only slightly larger than the intrinsic damping in NiFe thin films (0.008).[162,163] This fact indicates the high quality of the NiFe thin films in this work. Second, the data in Figs. 6.4 and 6.5(b) for InSb/NiFe and InSb/α-Sn/NiFe are the same as those shown in Fig. 6.3(d). They are included to ease comparison between the different samples.

Four important final remarks should be made. First, the α-Sn films in this work are all 6-nm thick. In thicker films, the β phase may be dominant over the α phase, as discussed in the previous section 6.3. On the other hand, with reduced α-Sn thicknesses, the quantum confinement effect may turn a TDS to a TI or a quantum spin Hall insulator.[164,165,166,167] Second, previous work has shown that interfacing a TI with a ferromagnetic metal can damage or suppress the TSS in the TI. [155-158] The comparison between the damping properties of InSb/α-Sn/Ag/NiFe and InSb/α-Sn/NiFe in Fig. 6.4 evidently suggests that this is also the case for the TSS in the TDS α-Sn. Third, TDSs should also host topological Fermi arc surface states;[39,168] in the case of TDS α-Sn, such states are expected to exist on surfaces parallel to the uniaxial tensile axis, namely, the four side surfaces of the α-Sn film in this work. Future studies on spin pumping effects associated with these Fermi arc states are very interesting. Finally, this work suggests that SOC in the bulk of α-Sn films and in the β-Sn films is no stronger than that in Ag. Future work that measures the bulk SOC strength, such as the spin Hall angle, in α-Sn and β-Sn films is of great interest.

This work has been presented in a manuscript entitled “Topological Surface States-Caused Large Damping Enhancement in Dirac Semimetal-Ferromagnetic Metal Layered Structures”. The full author list is Jinjun Ding, Chuanpu Liu, Rui Yu, Uppalaiah Erugu, Jinke Tang, Haifeng Ding, Hua Chen, and Mingzhong Wu. Jinjun Ding prepared the samples and performed FMR

measurements. Chuanpu Liu helped with data analysis. Rui Yu helped with magnetron sputtering. Uppalaiah Erugu helped with XRD measurements.

CHAPTER 7 MAGNETIZATION SWITCHING USING SURFACE STATES IN A TOPOLOGICAL DIRAC SEMIMETAL

7.1 Introduction

Spin-orbit torque (SOT) refers to the torque exerted on magnetic moments in a magnet, by a spin current generated in a neighboring material. In addition to being fundamentally intriguing, the SOT phenomenon enables the use of electric currents to manipulate nanoscale magnets and is therefore of great technological significance.

Earlier work has focused on layered hetero-structures based on heavy metals, such as Pt, Ta, and W.[169,170] Strong SOC in heavy metals has allowed for experimental demonstrations of SOT-driven magnetization switching,[134,169,170] domain wall motion,[171] and magnetization precession.[172] Such demonstrations have fueled considerable ongoing efforts on the development of SOT-based energy-efficient spintronic devices, including memory, logic, and microwave and terahertz oscillators.

Very recent work, however, shows that SOT devices with even higher efficiency can be achieved if one replaces heavy metals with topological insulators (TIs). Due to intrinsic spin-momentum locking of the topological surface states (TSS), a TI can convert a charge current into a spin current at an efficiency that is substantially higher than in a heavy metal. In particular, efficient magnetization switching has already been realized in a good number of TI/magnet bi-layered structures where the TI materials ranged from Bi_2Se_3 to $(Bi_{1-x}Sb_x)_2Te_3$ to $Bi_{0.9}Sb_{0.1}$ to

SmB_6, while the magnetic components included ferromagnetic metals, ferrimagnetic alloys, ferrimagnetic insulators, and magnetically doped TIs.[173,174,175,176,177,178,179,180]

In principle, topological surface states (TSS) are also present at the interface between a topological Dirac semimetal and a topologically trivial material, because of different band topologies of the two materials. These TSS are also expected to exhibit spin-momentum locking, due to the broken inversion symmetry at the interface. As such, topological Dirac semimetal (TDS) materials may have a charge-to-spin conversion efficiency as high as in TIs and therefore may also be used to effectively manipulate magnets. Such possibilities, however, have not been explored yet. This chapter reports on the experimental observation of efficient switching in a ferromagnetic thin film enabled by SOT from a neighboring TDS α-Sn thin film.

Three important points should be highlighted. First, the TDS is a relatively newly-discovered topological phase; in comparison with other TDS materials,[149,150,151,152] α-Sn is more attractive because (i) it is a single-element material and is therefore relatively easy to grow and (ii) it can transform to other topological phases, such as a TI or a Weyl semimetal, under certain strains or magnetic fields.[48,49] Second, this work demonstrates that TDS materials may be as promising as TI materials in terms of applications in spintronics, which significantly broadens the range of SOT materials available for energy-efficient devices. Third, this work may have transformative impact on the ongoing industrial development of SOT devices, because (i) the α-Sn thin films were grown on Si, a common industrial substrate, by sputtering, an industry-friendly film growth technique, and (ii) switching was demonstrated at room temperature (RT), rather than low temperature, in the absence of external fields.

7.2 Growth of α-Sn thin films

The α-Sn thin films were grown on single-crystal (111) Si substrates by DC magnetron

sputtering. The substrates are rinsed sequentially with acetone, isopropyl alcohol, and DI water, before being loaded into the sputtering chamber. Prior to sputtering, the chamber has a base pressure of 2.0×10^{-8} Torr; substrate biasing is performed that includes several cycles of Ar ion sputtering of the substrate surface and the post-annealing of the substrate at 250 °C. The Ar ion sputtering process is aimed at removing the thin oxidized layer on the top of the substrate, while the post-annealing process is to remove the moisture adherent on the substrate surface. After removing the oxidized layer and the surface moisture, the α-Sn deposition is then carried out at room temperature, at a rate of about 2 nm/min. The sputtering power is set to a low value of 15 W, in order to minimize the heating effect during the deposition. The film thicknesses are determined through X-ray reflection and atomic force microscopy (AFM) measurements. The major substrate biasing and sputtering control parameters are summarized in Table 7.1. The Si substrates are either n-type or undoped and have an electric resistivity larger than 1 kΩ·cm.

Table 7.1. Substrate biasing and sputtering control parameters for Sn film growth.

Substrate biasing	Ar ion sputtering	30 W, 2 min
	Annealing	250 °C, 60 min
	Cycles	3
Sputtering	Target-to-substrate distance	6.8 cm
	Sample holder rotation rate	10 rpm
	Ar pressure	6 mTorr
	Ar flow	6 sccm
	Sputtering power	15 W

The surface roughness of the substrates is smaller than 0.5 nm.[181] The lattice constant of α-Sn (a=6.489 Å) is larger than that of Si (a=5.4307 Å); this lattice mismatch gives rise to a perpendicular tensile strain in the α-Sn films and therefore makes the films a TDS phase.[49,50] The

TDS properties of the α-Sn films were characterized through electric transport measurements and analyses. The switching experiment was carried out with a micron-sized rectangular element made of an α-Sn(6 nm)/Ag(2 nm)/CoFeB(2 nm) tri-layered structure; the magnetization in CoFeB favors alignment along the length directions of the rectangular element. Field-free, current-induced switching of the magnetization between the length directions was observed at room temperature, with a switching current density (J_c) of about 4.7×10^6 A/cm^2. The analysis of J_c yielded a SOT efficiency of 2.2 in the α-Sn film, which is comparable to that in TIs and is substantially higher than that in heavy metals. Control measurements indicate that the switching is enabled mostly by the TSS in the α-Sn film, rather than by SOC in the bulk of the α-Sn film or current-produced heating effects in the structure.

The representative structural and morphological properties of the films are presented in Fig. 7.1. Figure 7.1(a) gives the X-ray diffraction (XRD) spectra of a 4-nm-thick Sn film (blue) and an 8-nm-thick Sn film (green), which were both capped by a 3-nm-thick Si_3N_4 protection layer. Figure 7.1(b) shows a fine-scan XRD spectrum of the 4-nm Sn film. The red profile is a fit to a Gaussian trial function, while the vertical dashed line indicates the theoretically expected position of the α-Sn (111) peak. Figure 7.1(c) presents an atomic force microscopy (AFM) surface image; the roughness value indicated is determined by averaging over the AFM measurements on five different 5 μm × 5 μm areas; the uncertainty is the corresponding standard deviation.

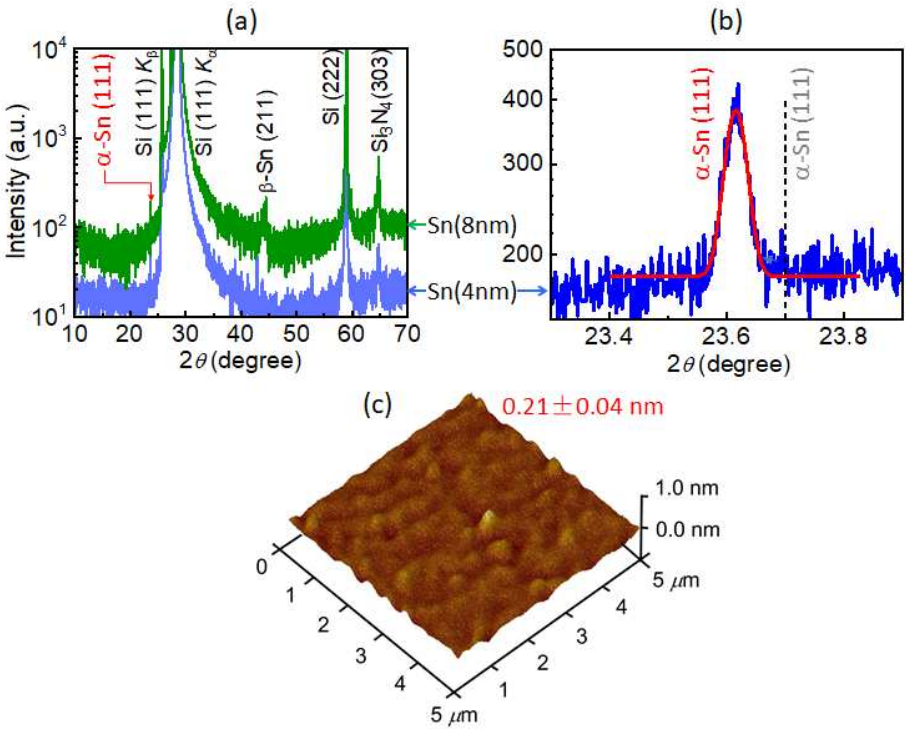

Figure 7.1. Structural and morphological properties of α-Sn thin films. (a) XRD spectra of a Si/Sn(4nm)/Si_3N_4(3nm) sample and a Si/Sn(8nm)/Si_3N_4(3nm) sample. (b) Fine-scan XRD spectrum of the Si/Sn(4nm)/Si_3N_4(3nm) sample. (c) AFM surface image of a Si/Sn(4nm) sample.

Four results are evident from the data in Fig. 7.1. (1) α-Sn and β-Sn coexist in the 8-nm film, but in the 4-nm film the α phase is more dominant than the β phase. As shown in Fig. 7.1(a), for the 4-nm film the α-Sn (111) peak has an intensity that is more than two times stronger than the β-Sn (211) peak, although both peaks are very weak in comparison with the Si and Si_3N_4 peaks. (2) There is only one peak for the α-Sn in the 4-nm film, possibly indicating the quasi-epitaxial growth of the α-Sn film. (3) As shown in Fig. 7.1(b), the α-Sn (111) peak appears on the left side of the theoretically expected peak position, which indicates the presence of a perpendicular tensile strain or an in-plane compressive strain in the film. This is consistent with the expectation that an α-Sn film grown on a Si substrate should exhibit an in-plane compressive strain because the lattice constant of α-Sn is larger than that of Si. The fitting in Fig. 7.1(b) yields a lattice constant

of about 6.519Å for the 4-nm film, which corresponds to a perpendicular tensile strain of ~0.46%. Such a strain makes the α-Sn film a TDS.[49,50] (4) The film has a very smooth surface, which facilitates the fabrication of layered hetero-structures with high-quality interfaces for switching experiments.

7.3 Electric transport properties of α-Sn thin films

In order to measure the electric transport properties of α-Sn thin films, a Hall bar device was fabricated through photolithography and argon ion milling processes. Figure 7.2(a) illustrates the Hall bar structure and the experimental configuration for the measurements of electric transport properties of α-Sn thin films. The central area of the Hall bar is 300 μm long and 100 μm wide.

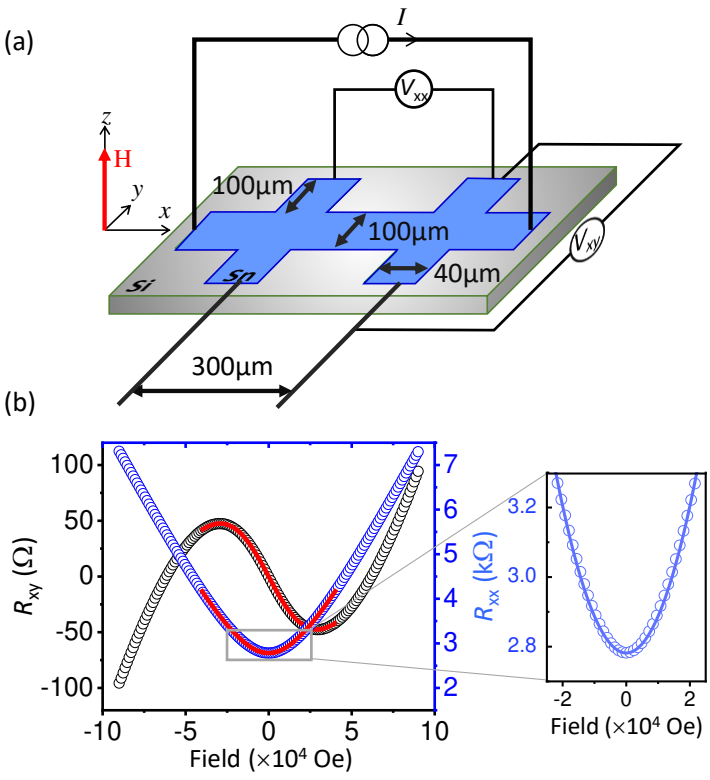

Figure 7.2. Electric transport properties of α-Sn thin films. (a) Measurement configuration. (b) Hall resistance (R_{xy}, left) and longitudinal resistance (R_{xx}, right) of a Si/α-Sn(6nm)/Si_3N_4(3nm) sample measured as a function of the magnetic field (H). The circles show the experimental data, while the curves show numerical fits.

Figure 7.2 presents the transport data that show the features of TDS materials. Figure 7.2(a) illustrates the measurement configuration. Figure 7.2(b) gives the Hall resistance (R_{xy}) and longitudinal resistance (R_{xx}) of a Hall bar structure made of Si/α-Sn(6 nm)/Si_3N_4(3 nm) measured as a function of a perpendicular magnetic field (H) at RT.

The data in Fig. 7.2 show three important results. (1) The R_{xy} vs. H response is strongly nonlinear, as shown by the black circles in Fig. 7.2(b). This result clearly indicates the existence of parallel conduction channels in the α-Sn film, which is common in TDS materials.[182] In contrast, β-Sn thin films show usual linear R_{xy} vs. H responses. (2) The R_{xx} vs. H data show a quadratic field dependence at low fields (H<20 kOe), as indicated by the quadratic fit (blue curve) in the right graph in Fig. 7.2(b). This quadratic response is common for non-magnetic systems, including TDS materials,[182,183,184,185] and is believed to arise from the Lorentz deflection of the carriers in the α-Sn film. (3) The R_{xx} vs. H data show non-saturating linear magnetoresistance at high fields (H>50 kOe). This is an important property of TDS materials, although its physical origin is still under debate.[40,41,186,187,188,189]

The above results together clearly indicate that the 6-nm Sn film is a semimetal, rather than a metal. In other words, the films are dominated by the α-Sn phase, not the β-Sn phase. This conclusion is further supported by the fact that the resistivity of the α-Sn films in this work (5.6×10^{-4} Ω·cm) is more than one order of magnitude higher than in metallic β-Sn films grown on Si substrates (1.5×10^{-5} Ω·cm). These results, together with the strain property indicated by the XRD data in Fig. 7.1(b), suggest that the 6-nm film in this work is a TDS.

In addition to the above qualitative results, one can also achieve a more quantitative understanding on the properties of the α-Sn films by numerically fitting the $R_{xx}(H)$ and $R_{xy}(H)$ data in Fig. 7.2, as in previous works.[182, 190, 191] The two red curves in Fig. 7.2(b) show the

simultaneous fits of $R_{xx}(H)$ and $R_{xy}(H)$ to a three-channel model in which two channels are *n*-type and the other is *p*-type:

$$\rho_{xx} = \frac{\sigma_{xx}}{\sigma_{xx}^2+\sigma_{xy}^2} t \tag{7.1}$$

$$\rho_{xy} = \frac{\sigma_{xy}}{\sigma_{xx}^2+\sigma_{xy}^2} t \tag{7.2}$$

$$\sigma_{xx} = \sum_{i=1}^{3} \frac{n_i e \mu_i}{1+(\mu_i \mu_0 H)^2} \tag{7.3}$$

$$\sigma_{xy} = \sum_{i=1}^{3} \frac{n_i e \mu_i^2 \mu_0 H}{1+(\mu_i \mu_0 H)^2} \tag{7.4}$$

where $\rho_{xx} = R_{xx}\frac{wt}{l}$ (thickness t=6 nm, width w=100 μm, length l=300 μm) and $\rho_{xy} = R_{xy}t$ denote the longitudinal and Hall resistivities, respectively; σ_{xx} and σ_{xy} are the two-dimensional (2D) longitudinal and Hall sheet conductivities, respectively; n_i is the 2D carrier density (positive); e and μ_i denote the carrier charge and mobility, respectively (negative for electrons and positive for holes); and $\mu_0 = 4\pi \times 10^{-7}$ H/m is the free-space permeability constant.

One can see that the two fits in Fig. 7.2(b) are both almost perfect. On the other hand, the fitting is poor if one considers either a two-channel model or a three-channel model with one *n*-type and the other two *p*-type. These results together indicate that the three-channel model used can appropriately describe the physical processes in the α-Sn film. Note that the fitting shown in Fig. 7.2(b) is for a field range from -40 kOe to 40 kOe, not for the entire field range, as Eqs. (7.1) and (7.2) are valid for weak fields only.

Table 7.2 lists the fitting-yielded results, together with the sheet resistance $R_{s,i} = (n_i e\, \mu_i)^{-1}$ values. The carriers in the first two channels have relatively high density and relatively low mobility. They can be assigned to holes and electrons activated thermally for the bulk states. As reported previously, due to the band crossing at the Fermi level, TDS materials can undergo thermal activation in which electrons in the valence band below the Dirac points can be thermally

activated to the conduction band above the Dirac points. These carriers can also be attributed to indirect inter-band thermal transitions in the α-Sn film, as discussed previously.[182] The third channel in Table 1 can be assigned to the TSS. The carriers are *n*-type, which is consistent with the fact that the Dirac point of the TSS is below the Fermi level;[49,50] the mobility is relatively high, which is expected because, unlike the bulk states, the TSS do not undergo backscattering.

Table 7.2. Carrier properties in a 6-nm α-Sn thin film, obtained through fitting the resistivity data shown in Fig. 7.2(b).

Channel	Carrier density (cm^{-2})	Mobility ($cm^2V^{-1}s^{-1}$)	Type	Sheet resistance (Ω)
1	$(8.53\pm0.05)\times10^{12}$	1113±4	*p*	658
2	$(3.31\pm0.05)\times10^{12}$	-1254±31	*n*	1506
3	$(1.83\pm0.04)\times10^{12}$	-3588±19	*n*	952

As presented above, three different models have been used to fit numerically the experimentally measured $R_{xx}(H)$ and $R_{xy}(H)$ data. Figure 7.3 presents more numerical fits. The black and blue circles show the experimentally measured $R_{xy}(H)$ (left axes) and $R_{xx}(H)$ (right axes) data, respectively, while the red curves present the numerical fits. The left, middle, and right columns show the fits to a three-channel model with two *n*-type and the other *p*-type, a three-channel model with one *n*-type and the other two *p*-type, and a two-channel model with one *n*-type and the other *p*-type, respectively. The first, second, and third rows show the fits of the data over different field (H) ranges, as indicated. The fitting-yielded carrier density and mobility values for the fits in Figs. 7.3(a) and 7.3(b) are listed in Table 7.3 and Table 7.4, respectively.

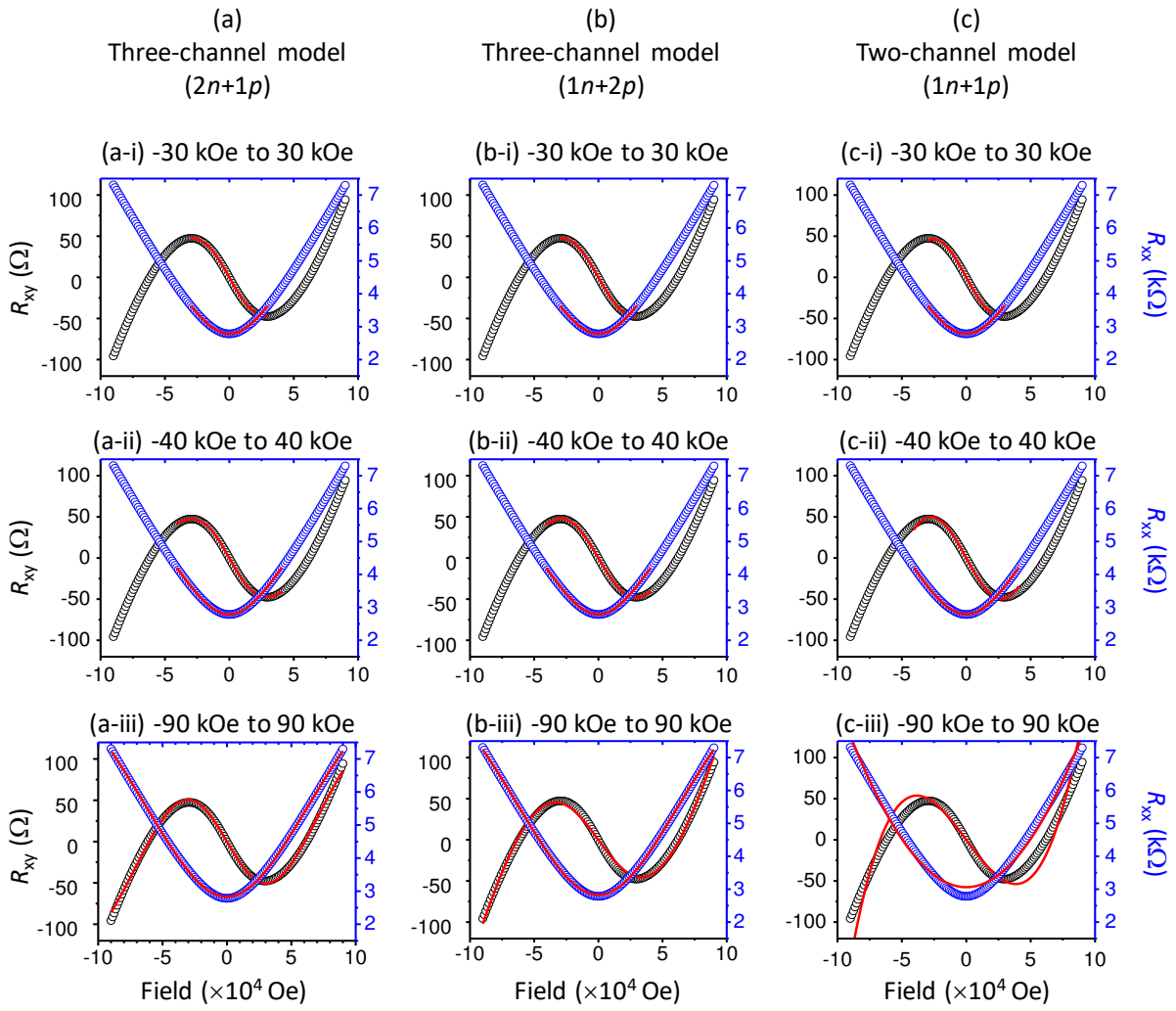

Figure 7.3. Hall resistance (R_{xy}, black circles, left axes) and longitudinal resistance (R_{xx}, blue circles, right axes) of a Si/α-Sn(6m)/Si_3N_4(3nm) sample measured as a function of an out-of-plane magnetic field (H) and fitted numerically to (a) a two-n-channel and one-p-channel model, (b) a two-p-channel and one-n-channel model, and (c) a one-n-channel and one-p-channel model. The three rows show the numerical fits (red curves) of the experimental data over different field ranges, as indicated.

Table 7.3. Carrier properties of a 6-nm-thick α-Sn thin film obtained through the numerical fitting of the experimentally measured resistance data to a two-*n*-channel, one-*p*-channel model. The numerical fits are shown in Fig. 7.3(a).

Channels	Field Range	-30 kOe to 30 kOe	-40 kOe to 40 kOe	-90 kOe to 90 kOe
Channel 1 *p*-type	2D carrier density (cm^{-2})	$(8.928\pm0.012)\times10^{12}$	$(8.538\pm0.054)\times10^{12}$	$(1.49\pm0.01)\times10^{12}$
	Carrier mobility ($cm^2V^{-1}s^{-1}$)	1091±8.2	1113±4.0	1736±11
Channel 2 *n*-type	2D carrier density (cm^{-2})	$(3.080\pm0.058)\times10^{12}$	$(3.319\pm0.046)\times10^{12}$	$(1.15\pm0.01)\times10^{12}$
	Carrier mobility ($cm^2V^{-1}s^{-1}$)	1586±8.0	1254±31	2336±13
Channel 3 *n*-type	2D carrier density (cm^{-2})	$(1.478\pm0.008)\times10^{12}$	$(1.826\pm0.036)\times10^{12}$	$(4.00\pm1.51)\times10^{13}$
	Carrier mobility ($cm^2V^{-1}s^{-1}$)	3781±53	3588±19	33±12

Table 7.4. Carrier properties of a 6-nm-thick α-Sn thin film obtained through the numerical fitting of the experimentally measured resistance data to a one-*n*-channel, two-*p*-channel model. The numerical fits are shown in Fig. 7.3(b).

Channels	Field Range	-30 kOe to 30 kOe	-40 kOe to 40 kOe	-90 kOe to 90 kOe
Channel 1 *p*-type	2D carrier density (cm^{-2})	$(4.67\pm1.44)\times10^{12}$	$(5.39\pm0.78)\times10^{12}$	$(5.43\pm0.49)\times10^{12}$
	Carrier mobility ($cm^2V^{-1}s^{-1}$)	1376±12	1320±62	1331±47
Channel 2 *n*-type	2D carrier density (cm^{-2})	$(2.49\pm0.084)\times10^{12}$	$(2.7\pm0.06)\times10^{12}$	$(3.57\pm0.05)\times10^{12}$
	Carrier mobility ($cm^2V^{-1}s^{-1}$)	3283±37	3149±29	2590±27
Channel 3 *p*-type	2D carrier density (cm^{-2})	$(2.208\pm18)\times10^{14}$	$(9.98\pm33)\times10^{14}$	$(1.31\pm0.22)\times10^{13}$
	Carrier mobility ($cm^2V^{-1}s^{-1}$)	27.5±25.6	4.56±15.2	258±70

The numerical fits presented in Fig. 7.3 and the fitting-yielded results listed in Tables 7.3 and 4 together show three important results:

1. The two-channel model cannot appropriately fit the data, as shown in Fig. 7.3(c), while the two "three-channel" models can fit the data much better, as shown in Figs. 7.3(a) and 7.3(b).

2. Among the two "three-channel" models, the "two-*n*-channel, one-*p*-channel" model can fit the data with reasonably small uncertainties or error bars, as shown in Table 7.3, while the other "three-channel" model does not, as can be seen from the bottom two rows in Table 7.4. This result suggests that the "two-*n*-channel, one-*p*-channel" model is more appropriate or accurate than the "one-*n*-channel, two-*p*-channel" model, in terms of describing the electric transport properties of the α-Sn thin film.
3. The results for the fitting of the data measured over relatively narrow fields are close to each other, but they are very different from the fitting results for the data measured over "-90 kOe to 90 kOe". This big difference is likely since Eqs. (7.3-7.4) are less valid or appropriate at high fields than at low fields. Because the fits over the field range of "-40 kOe to 40 kOe" capture more features of the experimental data than the field range of "-30 kOe to 30 kOe," only they are shown in Fig. 7.2(b) (red curves).

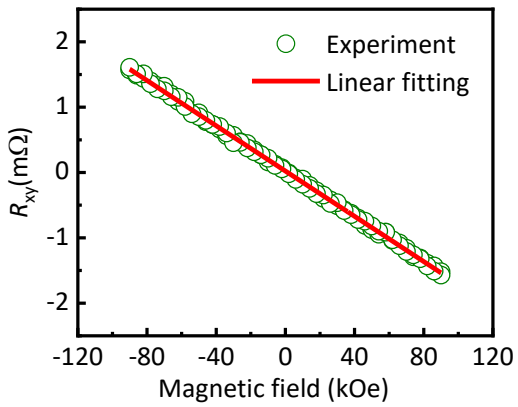

Figure 7.4. Hall resistance vs. field response of β-Sn film.

Figure 7.4 shows the Hall resistance of a 21-nm-thick β-Sn thin film measured as a function of an out-of-plane magnetic field. The film was grown on a Si substrate using the same growth conditions as for the α-Sn thin films. The green circles show the experimental data, while the red line is a linear fit. The negative slope shown in Fig. 7.4 indicates that the carrier in the β-Sn

thin film is *n*-type. Based on the slope, one can estimate the carrier density as 1.72 $\times 10^{22}$ cm^{-3}. This carrier density value is close to that in heavy metal Pt thin films (1.6×10^{22} cm^{-3})[192] and about 3-4 orders of magnitude higher than the values shown in Table 7.2 for the α-Sn thin film.

7.4 Magnetization switching using α-Sn

Turn now to the use of the TSS in the α-Sn film to switch a ferromagnet. The switching device was fabricated from a Si/Sn(6 nm)/Ag(2 nm)/CoFeB(2 nm) thin-film stack. A photo image of the device is presented in Fig. 7.6(a). The switching device was fabricated through the following steps:

1. A Sn(6 nm)/Ag(2 nm)/CoFeB(2 nm) thin-film stack was deposited via magnetron sputtering, where the Sn film has α phase as the dominant phase, and the CoFeB film is a $Co_{40}Fe_{40}B_{20}$ amorphous thin film with an in-plane easy anisotropy, as discussed shortly.
2. Photolithography and argon ion milling were used to fabricate an elliptical rectangle pitch of the Sn(6 nm)/Ag(2 nm)/CoFeB(2 nm) thin film stack (see the central part of the device photo image).
3. In order to make electric contacts, photolithography and argon ion milling were used to remove the CoFeB and Ag layers on the left and right portions of the elliptical rectangle pitch (the areas on the left and right sides of the red dashed rectangular in Fig. 7.6(a)). After that, a 50-nm-thick Au layer was deposited on top of the whole film structure.
4. The standard lift-off technique was used to form two Au pads for conducting electric currents.

As shown in Fig. 7.6(a), the central area of the Hall bar structure is 30 μm long (along the *y* axis) and 15 μm wide (along the *x* axis). The length is along the $[11\bar{2}]$ of the (111) Si substrate. The electrical connections were made using wire bonding with gold wires under a microscope.

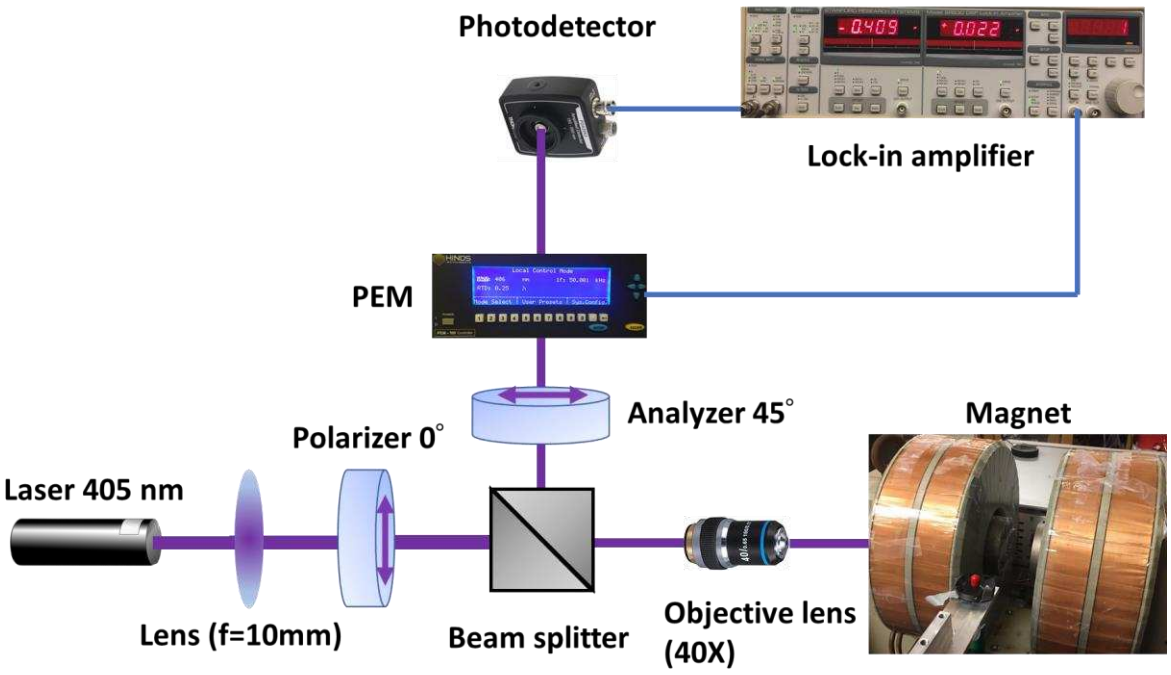

Figure 7.5. Longitudinal MOKE system.

In order to detect the magnetization of the CoFeB thin film, the magneto-optical Kerr effect (MOKE) technique was used. The MOKE measurements probe the change of the polarization direction of a linearly polarized light when it reflects from a magnetic material, which was observed first by John Kerr back in 1887. The MOKE response in magnetic materials arise due to the optical anisotropy of the materials. The source of this optical anisotropy is the magnetization **M** within the surface domains which can be influenced by external forces such as magnetic fields. The optical anisotropy alters the state of linearly polarized light which is reflected off the magnetic materials. The MOKE is characterized by the Kerr effect being proportional to the magnetization. This makes it particularly useful in the study of surface magnetism since it is highly sensitive to the magnetization within the skin depth region, typically 10-20 nm in most metals. The effect has been utilized to obtain hysteresis loops or domain images and is a relatively simple technique to implement. It has the ability to probe the magnetization in very small regions of a material, such

as wires or patterns, or in real device applications. The MOKE technique has been used extensively to characterize magnetic materials, especially magnetic thin films.

The longitudinal magneto-optical Kerr effect (MOKE) system build in the lab is shown schematically in Fig. 7.5. The MOKE system is equipped with a 405-nm laser with an output power of 10 mW; a temperature controller is embedded to enable steady output of the laser power. The beam from the laser is focused by a focal lens first and then goes to a polarizer and a beam splitter, as shown in Fig. 7.5. Before the laser beam hits the sample, an objective lens is used to further focus the beam down to about 8 μm in diameter. After hitting the sample, the laser beam is reflected, hits the beam splitter, and then goes to an analyzer. After that, the laser beam is modulated by a photon elastic modulator (PEM) and then goes to a photodetector. The modulation frequency is fixed at 50 kHz. A lock-in amplifier is used to detect the voltage signal from the photodetector.

Prior to each switching experiment, the laser beam is focused to the center of the switching device, with a laser spot size of about 8 μm in diameter. A MOKE hysteresis loop such as that shown in Fig. 7.6(b) is taken by sweeping the external magnetic field first; then current-induced magnetization switching is carried out.

Figure 7.6 shows the main data. Figure 7.6(a) shows the experimental configuration, with a picture of the switching device on the left and a diagram of the layered structure on the right. Figures 7.6(b) and 7.6(c) present the magneto-optical Kerr effect (MOKE) data for field- and current-induced switching, respectively, both measured at RT.

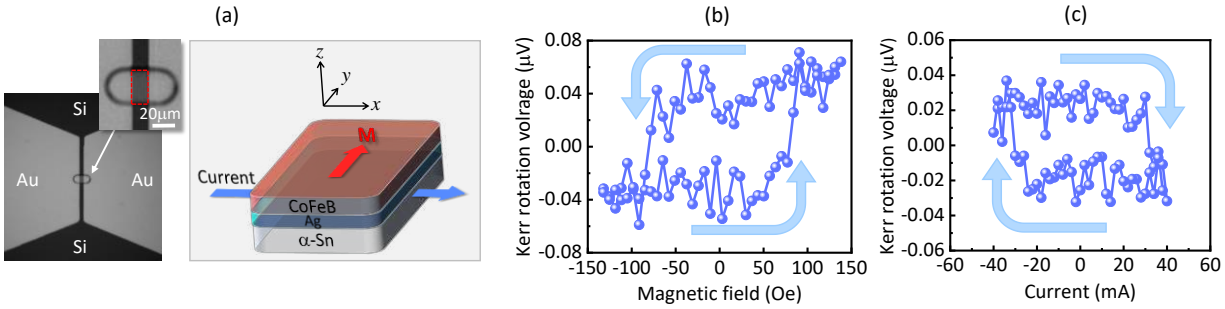

Figure 7.6. Magnetization switching in a Si/α-Sn(6nm)/Ag(2nm)/CoFeB(2nm) structure. (a) Experimental configuration. (b) Field-induced switching measured by a magneto-optical Kerr effect (MOKE) technique. (c) Field-free, current-induced switching measured by the MOKE technique.

As shown in Fig. 7.6(a), the core of the switching device is a 30 μm × 15 μm rectangle made of an α-Sn(6 nm)/Ag(2 nm)/CoFeB(2 nm) tri-layered structure. A 6-nm-thick α-Sn film was used for three reasons: (i) thicker films may have the β phase, not the α phase, as the dominant phase; (ii) in thinner films there may exist a quantum confinement effect that can turn the films into TI materials or quantum spin Hall insulators;[164,165,166,167] and (iii) the transport properties of the 6-nm α-Sn film are already known, as presented in Fig. 7.6 and Table 7.2. The CoFeB layer in the structure is a ferromagnetic amorphous alloy. The easy axis in the CoFeB film is along the rectangle length direction (the *y* axis), which facilitates the switching of the magnetization (**M**) between the ±*y* directions. The Ag layer works as a spacer to physically separate the α-Sn film from the CoFeB film. Previous works have shown that in a TI/ferromagnet bi-layered structure the TSS can be modified or even completely suppressed by the magnetic ordering in the ferromagnet.[155,156,157,158] Recent experiments demonstrated that this is actually the case in α-Sn/ferromagnet bilayers.[55] They also showed that an ultrathin Ag spacer could protect the TSS in the α-Sn film. Note that Ag is chosen because it has a long spin diffusion length (~700 nm) and a small spin Hall angle (0.0068).[154]

The data in Fig. 7.6(b) indicate that the CoFeB element can be switched with a modest

magnetic field of ~80 Oe. The data in Fig. 7.6(c) show that the same switching can be achieved by a current, in the absence of an external field. It is believed that this switching is induced by the spin current in the α-Sn film that is produced by the charge current along the *x* axis and has a spin polarization along the *y* axis; the spin current exerts an anti-damping torque on **M**, and the latter induces domain nucleation and drives domain walls to move in the CoFeB, giving rise to switching of **M** between the ±*y* directions. Note that the data shown in Fig. 7.6(c) were measured using current pulses with a duration (τ_p) of 0.1 ms. The switching current is about 31.1 mA, which corresponds to a switching current density (J_c) of 4.72×10^6 A/cm^2 in the α-Sn film.

Several notes should be made about the data shown in Fig. 7.6. First, prior to the collection of the data in both Figs. 7.6(b) and 7.6(c), an external field was applied to saturate **M** in the CoFeB film along the +*y* direction. Second, the two hysteresis loops in Figs. 7.6(b) and 7.6(c) evolve in opposite manners. This can be attributed to the definition of the sign of the charge current; a flip in the current sign would lead to two loops with the same evolution. Third, the overall change of the MOKE voltage in Fig. 7.6(c) is slightly smaller than that in Fig. 7.6(b). Possible reasons for this difference include: (i) there may be a difference in the position of the MOKE laser beam relative to the device center during the measurements and (ii) the current-induced switching may not be as complete as the field switching due to the use of a modest current.

The field-free, RT, current-induced switching demonstrated in Fig. 7.6 is very intriguing, yet it is possible that the switching is not associated with the TSS, but with other mechanisms — the switching may result from (1) the Oersted field produced by the current, (2) current-caused Joule heating, or (3) a SOT due to the bulk of the α-Sn film. The switching current cited above corresponds to an Oersted field of ~4.6 Oe, which is significantly smaller than the switching field shown in Fig. 7.6(b). Thus, one cannot attribute the current switching to the Oersted field and

can therefore rule out mechanism (1).

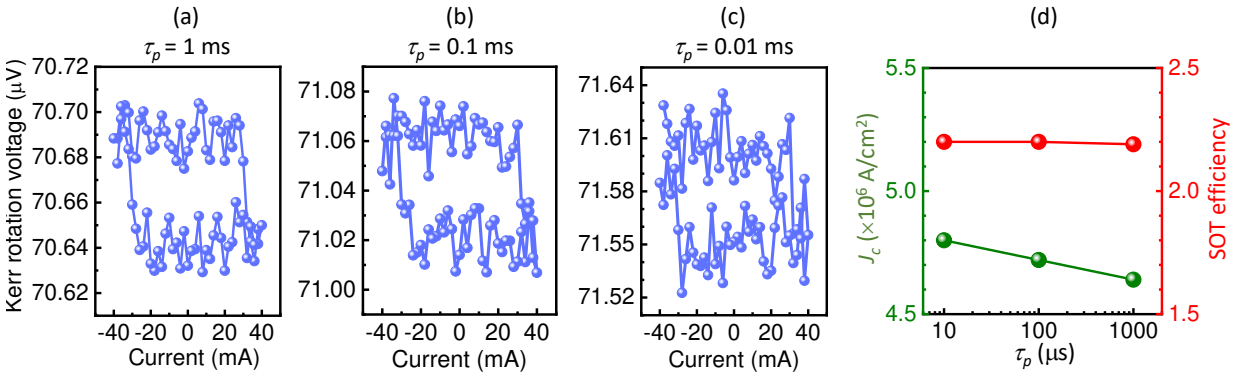

Figure 7.7. Effects of current pulse duration (τ_p) on switching in a Si/α-Sn(6nm)/Ag(2nm)/CoFeB(2nm) structure. (a), (b), and (c) present the switching responses for three different τ_p, as indicated. (d) presents the switching current density (J_c) and SOT efficiency (θ) as a function of τ_p.

To check the possibility of mechanism (2), current-induced switching measurements were carried out with different τ_p. Figure 7.7 presents the data. One can see that a decrease in τ_p gives rise to a slightly noisier loop, but no notable changes in the loop width. Specifically, as τ_p is reduced by two orders of magnitudes, J_c increases only about 3.4%. This result evidently indicates that the current switching cannot be attributed to the heating effects produced by the current.

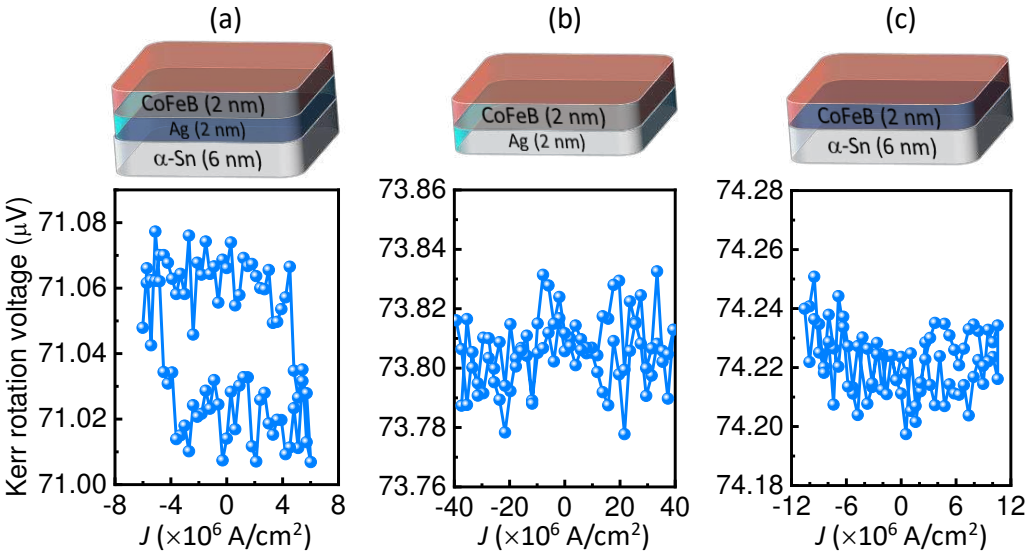

Figure. 7.8. Comparison of MOKE voltage vs. current responses in three different structures.

To further confirm the invalidity of mechanisms (1) and (2) and check the possibility of mechanism (3), two control samples were fabricated and measured, with the data shown in Fig. 7.8. Note that the control samples were prepared using the exact same substrates, targets, and sputtering conditions as the α-Sn/Ag/CoFeB sample. It is evident that no switching responses are observed in Figs. 7.8(b) and 7.8(c), even with larger currents. This supports the above conclusions, namely, that the switching cannot be attributed to the current-produced Oersted field or heating. What's more, the absence of a switching response in the α-Sn/CoFeB sample indicates that the SOT from the bulk of the α-Sn film alone is not strong enough to switch the CoFeB. Note that there are no TSS at the α-Sn/CoFeB interface, due to the reason mentioned above; any SOT effects, if present in the structure, would be mostly due to the bulk of the α-Sn film. As such, mechanism (3) can be ruled out.

7.5 Spin-orbit torque efficiency of α-Sn

7.5.1 Magnetic properties of CoFeB nano-device

The static magnetic properties of the CoFeB thin film in the Si/Sn(6 nm)/Ag(2 nm)/CoFeB(2 nm) layered structure were characterized via MOKE and vibrating sample magnetometer (VSM) measurements. Figure 7.9 gives the representative data, all measured at room temperature (RT). Figure 7.9(a) shows the magnetic hysteresis loops measured by a VSM with magnetic fields (H) applied along two different crystal-axis directions of the (111) Si substrate, as indicated. Figure 7.9(b) shows the remnant moments determined from the magnetic hysteresis loops, such as those shown in Fig. 7.9(a), that were measured by in-plane magnetic fields applied at different angles (θ_H) relative to the $[1\bar{1}0]$ direction of the Si substrate. Figure 7.9(c) presents a MOKE hysteresis loop measured on the same sample, with a magnetic field applied along the $[11\bar{2}]$ direction. Note that $[1\bar{1}0]$ and $[11\bar{2}]$ are both on the (111) plane and are perpendicular to each other.

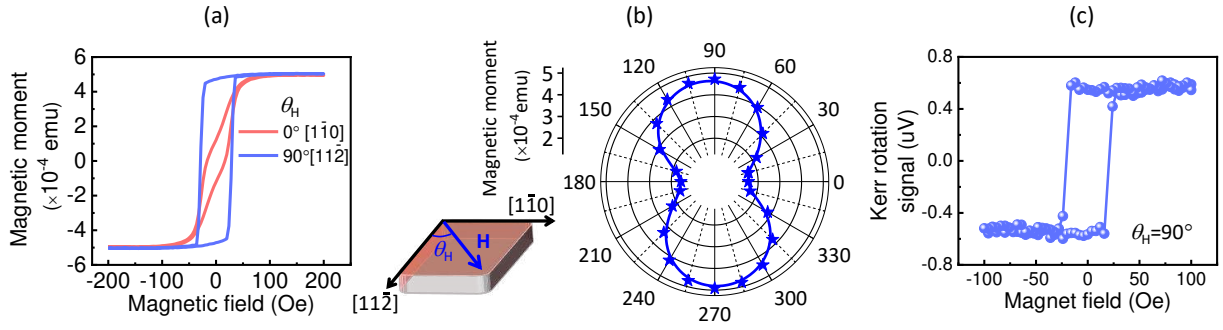

Figure 7.9. Static magnetic properties of the CoFeB thin film in a Si/Sn/Ag/CoFeB layered structure. (a) Magnetic hysteresis loops measured by a VSM for two different field directions, one along $[1\bar{1}0]$ and the other along $[11\bar{2}]$. (b) Angular dependence of remnant moments obtained from the VSM hysteresis loops. (c) Magnetic hysteresis loop measured by a MOKE system.

The data in Fig. 7.9 evidently show that there exists a weak in-plane uniaxial anisotropy in the CoFeB film, with its easy axis along the $[11\bar{2}]$ direction, despite the three-fold rotational symmetry of the (111) Si substrate. The presence of such an in-plane uniaxial anisotropy in

amorphous CoFeB thin films has been reported previously by a number of groups.[193,194,195,196] The formation of this anisotropy may be associated with the presence of a weak stress induced by the rotating substrate holder or the stray field of the CoFeB film during the deposition process, as discussed previously.[193,194,196] Besides, from the data in Fig. 7.9(a) one can also obtain the saturation induction ($4\pi M_s$) of the CoFeB film, which is about 11.6 kG.

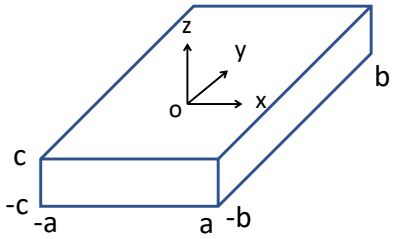

Figure 7.10. Geometry for demagnetization factor calculations.

In addition to the anisotropy described above, there also exists a weak shape anisotropy in the rectangular CoFeB thin film element in the switching device. Considering the geometry shown in Fig. 7.10 and taking $2a$=15 μm, $2b$=30 μm, and $2c$=2 nm, one can obtain the demagnetization factors along the three axes as $N_x = 2.1\times10^{-4}$, $N_y = 4.2\times10^{-5}$, and $N_z = 0.999$. The calculation of N_y used[197]

$$\pi N_y = \frac{b^2-c^2}{2bc}\ln\left(\frac{\sqrt{a^2+b^2+c^2}-a}{\sqrt{a^2+b^2+c^2}+a}\right) + \frac{a^2-c^2}{2ac}\ln\left(\frac{\sqrt{a^2+b^2+c^2}-b}{\sqrt{a^2+b^2+c^2}+b}\right) + \frac{b}{2c}\ln\left(\frac{\sqrt{a^2+b^2}+a}{\sqrt{a^2+b^2}-a}\right) + \frac{a}{2c}\ln\left(\frac{\sqrt{a^2+b^2}+b}{\sqrt{a^2+b^2}-b}\right) +$$
$$\frac{c}{2a}\ln\left(\frac{\sqrt{c^2+b^2}-b}{\sqrt{c^2+b^2}+b}\right) + \frac{c}{2b}\ln\left(\frac{\sqrt{a^2+c^2}-a}{\sqrt{a^2+c^2}+a}\right) + 2\arctan\left(\frac{ab}{c\sqrt{a^2+b^2+c^2}}\right) + \frac{a^3+b^3-2c^3}{3abc} +$$
$$\frac{a^3+b^3-2c^3}{3abc}\sqrt{a^2+b^2+c^2} + \frac{c}{ab}\left(\sqrt{a^2+c^2}+\sqrt{b^2+c^2}\right) - \frac{(a^2+b^2)^{\frac{3}{2}}+(b^2+c^2)^{\frac{3}{2}}+(a^2+c^2)^{\frac{3}{2}}}{3abc} \quad (7.5)$$

The calculation of N_x used a similar equation but with b and a exchanged. N_z was evaluated as $1 - N_x - N_x$. One can see that N_y is five times smaller than N_x, indicating that the y axis is a slightly more preferred axis for the magnetization than the x axis. The combination of this shape-associated anisotropy and the growth-associated anisotropy described in the last section makes the

length direction of the rectangular CoFeB element an easy axis.

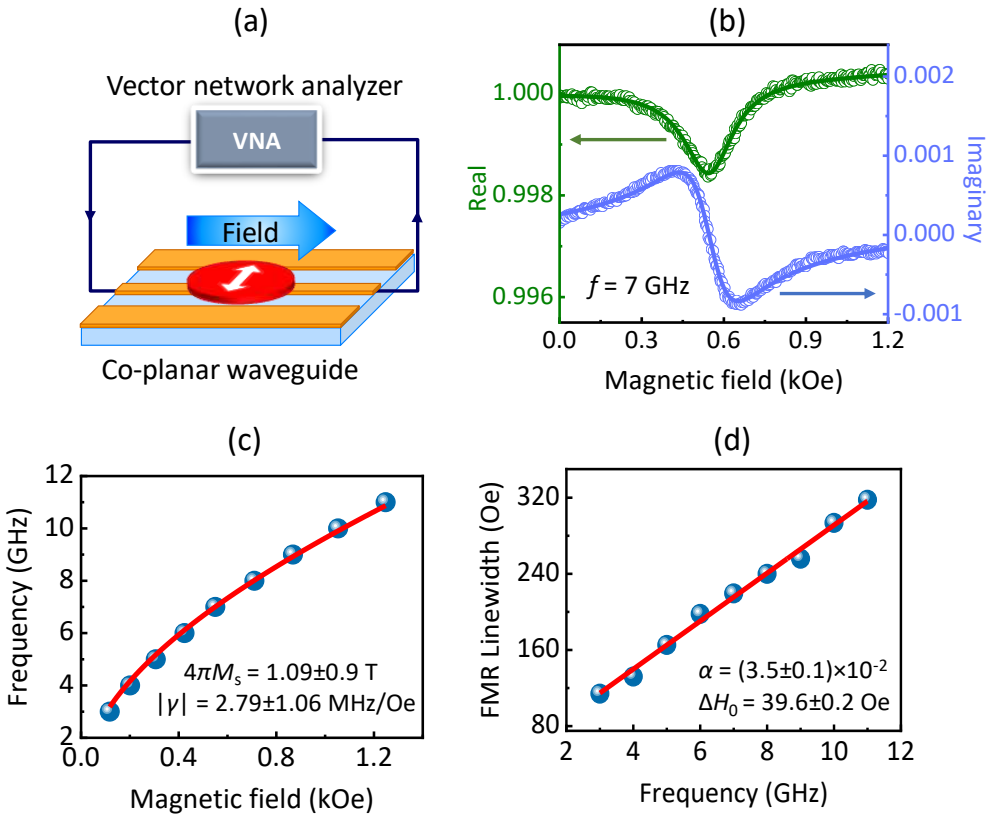

Figure 7.11. Vector network analyzer ferromagnetic resonance (FMR) measurements on a 2-nm-thick CoFeB thin film. (a) Experimental configuration. (b) Representative transmission coefficient (S_{21}) profiles. (c) FMR field as a function of microwave frequency (f). (d) FMR linewidth as a function of f. In (b)-(d), the symbols show the experimental data, while the curves and lines show numerical fits.

The magnetic damping constant of the CoFeB thin film was determined through broadband vector network analyzer (VNA)-based ferromagnetic resonance (FMR) measurements. Figure 7.11 shows the measurement and analysis approaches. Figure 7.11(a) sketches the experimental setup, which consists mainly of a VNA and a coplanar waveguide (CPW). The CPW structure has a 50-μm-wide signal line and a signal line-to-ground spacing of 25 μm; its nominal impedance is 50 Ω. The CoFeB sample, shown as a red disk in Fig. 7.11(a), is placed on the CPW with the CoFeB film side facing the CPW structure and the Si substrate side facing up. An external static magnetic field (H), shown as a blue arrow in Fig. 7.11(a), is applied along the CPW signal line to

either magnetize the film to saturation or enable VNA-FMR measurements. The major measurement and data analysis procedures are as follows:

(i) Magnetize the CoFeB film to saturation with a large in-plane magnetic field. For the data presented below, this field is 2 kOe.

(ii) Measure the transmission coefficient (S_{21}) of the CPW/CoFeB structure as a function of H at a fixed microwave frequency (f). Figure 7.11(b) presents representative S_{21} profiles measured at f = 7 GHz.

(iii) Fit the S_{21} data with the theoretical S_{21} profiles[121,122] to determine the FMR field (H_{FMR}) and the FMR linewidth (ΔH). The curves in Fig. 7.11(b) show such fits. Note that ΔH here refers to "full width at half maximum," rather than the peak-to-peak linewidth.

(iv) Repeat (i)-(iii) for different microwave frequencies over 3-11 GHz.

(v) Plot H_{FMR} vs. f and then numerically fit the data using the Kittel equation:

$$\omega = 2\pi|\gamma|\sqrt{H_{\mathrm{FMR}}(H_{\mathrm{FMR}} + 4\pi M_{\mathrm{S}})} \tag{7.6}$$

as shown in Fig. 7.11(c). Note that in Eq. (7.6), $\omega = 2\pi f$ is the angular frequency, $|\gamma|$ is the absolute gyromagnetic ratio, and $4\pi M_s$ is the saturation induction. In Fig. 7.11(c), the symbols show the data, while the line shows the fit. The fitting-yielded $|\gamma|$ and $4\pi M_s$ values are indicated in Fig. 7.11(c).

(vi) Plot ΔH vs. f and then numerically fit the data using

$$\Delta H = \frac{2\alpha}{|\gamma|} f + \Delta H_0 \tag{7.7}$$

as shown in Fig. 7.11(d). In Eq. (7.7), α is the effective damping constant, and ΔH_0 denotes line broadening due to the spatial inhomogeneity of the CoFeB thin film. Note that in Fig. 7.11(d), the symbols show the data, while the line shows the fit. The fitting yields α and ΔH_0, as indicated in Fig. 7.11(d).

The fitting in Fig. 7.11(d) gives α=0.035±0.001. This damping value is close to that reported previously for CoFeB thin films.[198] The fitting in Fig. 7.11(c) gives $4\pi M_s \approx 10.9$ kG, which is close to the value from the VSM measurements mentioned above (11.6 kG). Further, the fitting-yielded $|\gamma|$ value (2.79 MHz/Oe) almost perfectly agrees with the standard value (2.80 MHz/Oe).

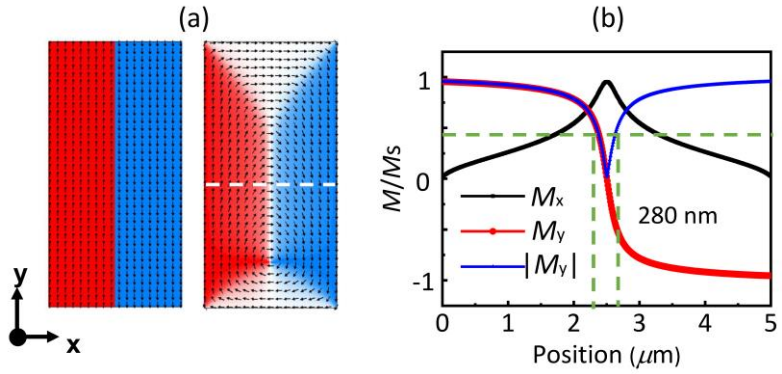

Figure 7.12. Micromagnetic simulations of magnetic domains in CoFeB thin films. (a) The initial (left) and final (right) states of magnetization distribution in a simulation. The black arrows indicate the spin direction. (b) Spatial profiles of different magnetization components along the white dashed line in (a).

The evaluation of the spin-orbit-torque (SOT) efficiency in this work needs to use the domain wall width d_w in the CoFeB thin film. To estimate d_w, micromagnetic simulations were performed using object-oriented-micromagnetic-framework (OOMMF).[199] The simulated film size was set to 10 μm × 5 μm × 2 nm. The mesh size of 5 nm × 5 nm × 2 nm was used. The magnetic material parameters are as follows: saturation induction $4\pi M_s \approx 12$ kG which was measured by a VSM, Gilbert damping constant $\alpha = 0.035$ which was measured by the VNA-FMR, exchange constant $A = 1.6\times10^{-11}$ J/m (or 1.6×10^{-6} erg/cm),[200] and absolute gyromagnetic ratio $|\gamma| = 2.211\times10^{5}$ m/(A·s) (or 2.8 MHz/Oe). No anisotropy was introduced in the simulation.

Figure 7.12(a) shows the two snapshots of the magnetization distribution in the micromagnetic simulation: the left one shows the initial state of the film which was set to two perfectly antiparallel domains with a head-to-tail boundary, while the right one shows the finalized state of the film which was obtained after the film had been relaxed freely for a sufficiently long

time. The black arrows represent the spin direction, and the colors of the pixels help to guide to different domains. The normalized magnetization profile along the white dash line in the right snapshot is shown in Fig. 7.12(b). The black, red, and blue dots present the in-plane magnetization component M_x, the in-plane component M_y, and the absolute value of M_y, respectively, along the white dash line. The spatial distance of half maximums of the $|M_y|$ profile shown in Fig. 7.12(b) is defined as the domain wall width, which is δ_w = 280 nm.

7.5.2 Spin-orbit torque efficiency

The above results together indicate that the current switching in the α-Sn/Ag/CoFeB sample is mostly associated with the TSS in the structure. This suggests that TSS in TDS materials can be utilized to manipulate magnets, just as TSS in TI materials. In order to compare the efficiencies of TDS α-Sn with TI materials as well as heavy metals in terms of producing SOT, one can define a dimensionless charge-to-spin conversion efficiency as

$$\theta = \frac{J_s}{J_c} \tag{7.8}$$

where J_s and J_c denote the nominal spin current density and the charge current density, respectively. This SOT efficiency can be estimated from the switching current measured experimentally;[175] it corresponds to the spin Hall angle of a material in which the same charge current density as in the α-Sn film could produce the same spin current density.

The red points in Fig. 7.7(d) represent the estimated efficiency θ values. The data in Fig. 7.7(d) show that as the current duration is reduced by two orders of magnitude, θ remains almost unchanged, as expected. Table 7.5 compares the θ values in several different materials used in recent SOT switching experiments.[33,178,201,202] It can be seen that the SOT efficiency in the α-Sn thin film in this work is comparable to that in TI thin films and is one order of magnitude higher

than that in heavy metals.

Table 7.5. Comparison of SOT efficiency in different materials.

Material	Efficiency θ	Temperature	Reference
Bi_2Se_3	2.0-3.5	4.2 K	173
Bi_xSe_{1-x}	1.7	RT	174
W	0.4	RT	201
Ta	0.15	RT	170
Pt	0.08	RT	202
α-Sn	2.2	RT	This work

The switching current density J_c values used in the SOT efficiency calculations (next section) were determined by considering the Sn, Ag, and CoFeB layers in the switching element as three resistors in parallel. They were evaluated by the use of the following equation

$$J_c = \frac{I_c}{w\rho_{Sn}}\left(\frac{t_{Sn}}{\rho_{Sn}} + \frac{t_{Ag}}{\rho_{Ag}} + \frac{t_{CoFeB}}{\rho_{CoFeB}}\right)^{-1} \tag{7.9}$$

where I_c is the switching current; w=30 μm is the width of the switching element; t_{Sn}=6 nm, t_{Ag}=2 nm, and t_{CoFeB}=2 nm are the thicknesses of the three layers; ρ_{Sn}=5.56×10^{-4} Ω·cm, ρ_{Ag}=1.18×10^{-4} Ω·cm,[203] and ρ_{CoFeB}=1.70×10^{-4} Ω·cm[136] are the resistivities of the three layers.

From the MOKE data in Figs. 7.7(a), 7.7(b), and 7.7(c), one can obtain the switching current I_c as 30.6 mA for τ_p=1 ms, 31.1 mA for τ_p=0.1 ms, and 31.6 mA for τ_p=0.01 ms. From these I_c values, one can then use the above equation to calculate the switching current density J_c as 4.64×10^6 A/cm^2 for τ_p=1 ms, 4.72×10^6 A/cm^2 for τ_p=0.1 ms, and 4.80×10^6 A/cm^2 for τ_p=0.01 ms. These values are presented in Fig. 7.7(d).

The switching relies on an anti-damping torque exerted by the spin current on the magnetization **M**. Specifically, if **M** is initially aligned along the +y direction and the spin current

has a polarization along the –*y* direction, the spin current exerts a torque on **M** that is anti-parallel to the damping torque. If the charge current density is increased to be beyond a threshold value so that the anti-damping torque is larger than the damping torque, **M** starts to precess about its equilibrium direction, with a precession angle increasing with time. As long as the current is on, the precession angle will increase continuously, and **M** will eventually reverse and align along the –*y* direction.

By considering a fine balance between the damping torque and the SOT-produced anti-damping torque in the Gilbert equation, one can derive the critical charge current density for the switching as[204,205]

$$J_{c0} = \frac{2e}{\hbar}\frac{1}{\theta}M_s d\alpha\mu_0\left(H_a + \frac{M_s}{2}\right) \tag{7.10}$$

where e is the electron charge, $\hbar$ is the reduced Planck constant, and θ is the dimensionless charge-to-spin conversion efficiency or the SOT efficiency; M_s, d, α, and H_a denote the saturation magnetization, thickness, Gilbert damping constant, effective anisotropy field (along the *y* axis) of the ferromagnetic film, respectively; and μ_0 is the free-space permeability constant.

Equation (7.5) is obtained in the absence of thermal fluctuations but switching in a real device is influenced by thermal activation processes and therefore requires a current density lower than J_{c0}. Specifically, at finite temperature, there exists a finite probability for the magnetization **M** in a small ferromagnet to flip and reverse its direction. The mean time between the two flips is often called the Néel relaxation time and is usually given by[206]

$$\tau_N = \frac{1}{f_0}e^{\frac{KV}{k_B T}} \tag{7.11}$$

where f_0 is the so-called attempt frequency associated with the precession frequency of **M**, K is the anisotropy constant, V is the volume of the ferromagnet, k_B is the Boltzmann constant, and T is the temperature. Note that KV in Eq. (7.11) denotes the energy barrier for thermally activated

magnetization switching. In the presence of a SOT, the effective energy barrier is lower but is difficult to define. However, Eq. (7.10) can still be approximately valid if one replaces T with an effective temperature defined as[175,207]

$$T_{eff} = \frac{T}{1-\frac{J}{J_{c0}}} \tag{7.12}$$

Based on Eqs. (7.11) and (7.12), one can see that as J is increased towards J_{c0}, T_{eff} increases and τ_N decreases. If τ_N is reduced to be as short as the duration τ_p of the current pulse used in the switching experiments, thermal agitation plays an important role in the magnetization switching. Note that Eq. (7.12) breaks down if $J \geq J_{c0}$. Thus, one can see that there exists a critical current density J_c for τ_N being comparable to τ_p. This J_c satisfies

$$\tau_p = \frac{1}{f_0} e^{\frac{KV}{k_B T}\left(1-\frac{J_c}{J_{c0}}\right)} \tag{7.13}$$

One can use Eq. (7.14) to estimate J_c as

$$J_c = J_{c0}\left[1 - \frac{k_B T}{KV}\ln\left(\tau_p f_0\right)\right] \tag{7.14}$$

Substituting Eq. (7.11) to Eq. (7.15), one then obtains

$$J_c = \frac{2e}{\hbar}\frac{1}{\theta} M_s d\alpha\mu_0 \left(H_a + \frac{M_s}{2}\right)\left[1 - \frac{k_B T}{KV}\ln\left(\tau_p f_0\right)\right] \tag{7.15}$$

This equation allows for the use of the experimentally measured J_c to evaluate the SOT efficiency θ in the switching device.

The switching element in this work is relatively large, so the magnetization switching is most likely realized through (1) domain nucleation and (2) domain wall motion. As the J_c value measured experimentally is mostly for the domain nucleation process, one can use Eq. (7.15) to evaluate θ by considering the localized nucleation of a reverse domain in an activation volume of $V_m \approx \delta_w^2 d$, where δ_w is the width or thickness of the domain wall in the CoFeB thin film. As such, one can rewrite Eq. (7.8) as

$$\theta = \frac{2e}{\hbar}\frac{1}{J_c}M_s d\alpha\mu_0\left(H_a + \frac{M_s}{2}\right)\left[1 - \frac{k_B T}{K(\delta_w^2 d)}\ln(\tau_p f_0)\right] \quad (7.16)$$

The calculations of the θ values presented in Fig. 7.6(d) and Table 7.6 assumed $H_a \approx H_c$ =76 Oe and $K \approx \frac{H_c M_s}{2}$. The calculations used M_s≈924 emu/cm^3 which was measured by a vibrating sample magnetometer, d=2 nm, α≈0.035 which was determined through vector network analyzer-based ferromagnetic resonance measurements, $\delta_w \approx$ 280 nm which was determined through micromagnetic simulations, and f_0=10 GHz. For τ_p=1 ms, one obtains J_{c0} = 5.28×10^6 A/cm^2 and θ = 2.19. For τ_p=0.1 ms, one obtains J_{c0} = 5.27×10^6 A/cm^2 and θ =2.20. For τ_p=0.01 ms, one has J_{c0} = 5.26×10^6 A/cm^2 and θ = 2.20.

7.5.3 Calculation of 2D efficiency of α-Sn

The parameter θ defined by Eq. (7.8) enables a straightforward comparison of the efficiency in this work with the efficiencies reported previously in the interpretation of charge-to-spin conversion in TIs and heavy metals, but strictly speaking it is inappropriate to use θ to characterize the efficiency in this work as the switching is mostly associated with the TSS, rather than the bulk states in the α-Sn. Instead, one can define a 2D efficiency as[33,208]

$$q = \frac{J_s}{j_c} \quad (7.17)$$

where J_s is the three-dimensional spin current density as in Eq. (7.5), while j_c is the 2D surface current density for the TSS. Using R_s in Table 1, one obtains $q \approx$ 2.3 nm^{-1} for the TSS in the α-Sn. This value is comparable to previously reported value (1.0 nm^{-1}) for Sb_2Te_3.[208] This result further shows that the SOT efficiency in the α-Sn in this work is comparable to that in TI thin films.

For the switching in this work, the j_c value for the TSS in the α-Sn can be evaluated by

considering the three parallel conduction channels described in Table 7.2. For each channel, the resistance can be written as

$$R_i = R_{s,i}\frac{l}{w} \quad (i = 1, 2, 3) \tag{7.18}$$

where l=15 μm is the dimension of the α-Sn film along the x axis (or along the current) and w=30 μm is the dimension along the y axis. From Eq. (7.18), one can then write the conductance for each channel as

$$G_i = \frac{w}{R_{s,i}l} \tag{7.19}$$

Then, the current in each channel can be evaluated as

$$I_i = G_i V = G_i \frac{I_{total}}{G_{total}} \tag{7.20}$$

where V is the electric voltage along the current direction, $I_{total} = J_c wt$ is the total current in the α-Sn film, $G_{total} = \sum_{i=1}^{3} G_i$ is the total conductance of the α-Sn film, and $t = 6$ nm is the thickness of the α-Sn film. Substituting I_{total} and G_{total} into Eq. (7.20), one obtains

$$I_i = \frac{G_i}{\sum_{i=1}^{3} G_i} J_c wt = \frac{\frac{1}{R_{s,i}}}{\sum_{i=1}^{3}\left(\frac{1}{R_{s,i}}\right)} J_c wt \tag{7.21}$$

By dividing both the sides of Eq. (7.21) with w, one then obtains the 2D charge current density for each channel as

$$j_{c,i} = \frac{\frac{1}{R_{s,i}}}{\sum_{i=1}^{3}\left(\frac{1}{R_{s,i}}\right)} J_c t \tag{7.22}$$

Note that $j_{c,1}$ and $j_{c,2}$ correspond to the first two channels in Table 1, which are for the bulk states; $j_{c,3}$ correspond to the third channel, which is for the TSS. Considering the coexistence of the top and bottom surfaces, one can use $j_{c,3}/2$ to represent the 2D charge current density for one of the two surfaces of the α-Sn thin film. Using the sheet resistance $R_{s,i}$ data in Table 2 and the J_c

values obtained, one can estimate the 2D charge current density j_c for each surface as 0.453 A/cm for τ_p=1 ms, 0.460 A/cm for τ_p=0.1 ms, and 0.468 A/cm for τ_p=0.01 ms.

With the j_c values for the 2D TSS on each surface, one can now use Eq. (7.9) to estimate the 2D efficiencies (q) for different τ_p values. One obtains q=2.25 nm^{-1} for τ_p=1 ms, q=2.26 nm^{-1} for τ_p=0.1 ms, and q=2.26 nm^{-1} for τ_p=0.01 ms. These results indicate that 2D efficiency q does not vary with the current duration τ_p, which is expected.

7.6 Conclusions and outlook

Four final remarks are as follows. (1) This work demonstrates α-Sn TSS-induced field-free RT switching of a ferromagnet with in-plane magnetization; future studies using ferromagnets with perpendicular anisotropy are important from the perspectives of high-density memory and logic applications. Note that the SOT memory concept is very attractive currently as it allows for low-current switching and also enables the separation of the writing and reading channels. (2) The switching in this work is believed to be realized through domain nucleation and domain wall motion; future work is of great interest, particularly for racetrack memory applications,[99] that makes use of time- and spatial-resolved techniques[139,140] to directly probe such switching processes. (3) Further work is also of great interest that makes use of strain engineering to modify the band structure[49,50] or voltage gating to tune the Fermi level in α-Sn, to explore the possibilities of realizing α-Sn thin films with an even higher SOT efficiency. (4) TDSs should also host topological Fermi arc surface states;[39,168] in the case of TDS α-Sn, such states are expected to exist on surfaces parallel to the uniaxial tensile axis,[49] namely, the four side surfaces of the α-Sn film in this work. It is interesting to explore how to use such Fermi arc states for SOT switching in the future.

This work has been presented in a manuscript entitled “Switching of a Ferromagnet by Spin-Orbit Torque from a Topological Dirac Semimetal”. The full author list is Jinjun Ding, Chuanpu Liu, Vijaysankar Kalappattil, Yuejie Zhang, Oleksandr Mosendz, Uppalaiah Erugu, Rui Yu, Jifa Tian, August DeMann, Stuart B. Field, Xiaofei Yang, Haifeng Ding, Jinke Tang, Bruce Terris, Albert Fert, Hua Chen and Mingzhong Wu. Jinjun Ding, prepared the samples, performed electrical transport measurements, built the MOKE system and performed switching experiments. Chuanpu Liu performed FMR measurements. Vijaysankar Kalappattil helped with data analysis. Rui Yu helped with sputtering growth of α-Sn films. Uppalaiah Erugu helped with XRD measurements. Oleksandr Mosendz helped with valuable discussions. August DeMann helped with photolithography.

CHAPTER 8 TOPOLOGICAL HALL EFFECT IN A TOPOLOGICAL INSULATOR INTERFACED WITH A MAGNETIC INSULATOR

8.1 Introduction

A topological insulator (TI) is a material that is electrically insulating in its interior but hosts conducting states on its surfaces. The surface states in a TI are topologically protected by time-reversal symmetry; in momentum space, such topological surface states (TSS) manifest themselves as a linear Dirac cone with spin-momentum locking in the bulk band gap. One can break the time-reversal symmetry of the TSS and thereby open a gap at the Dirac point by interfacing the TI with a magnetic insulator (MI) with perpendicular magnetization. It is expected that such manipulation of the TSS can give rise to exotic, emergent quantum effects. In fact, previous experiments have already demonstrated the presence of the quantum anomalous Hall effect (QAHE) and axion insulator states in the region where the Fermi level is within the magnetic gap opened by the MI,[209,210,211] and the presence of the anomalous Hall effect (AHE) in the TI in the case where the Fermi level is not located in the magnetic gap.[180,212,213,214,215] Since these effects have both fundamental and potential technological implications, they have attracted considerable interest in recent years.

In the region where the Fermi level is not in the magnetic gap, a topological Hall effect (THE) has also been reported, adding a new member to the "Hall" family of the TI.[216,217] The experiments were carried out by interfacing a TI film with a magnetic TI film[216] or sandwiching a TI film with

two magnetic TI layers,[217] and the THE was measured as an "excess" Hall signal on top of the AHE signal. In contrast to the AHE and the QAHE that arise from the Berry-phase curvature in momentum space,[218,212,213] the THE originates from the Berry-phase curvature of topological spin textures in real space.[219,220,221,222,223] A very recent experiment,[224] however, offered an alternative interpretation of the reported THE — it attributes the THE signals to the overlapping of two AHE signals with opposite signs arising either from coexisting surface and bulk magnetic phases in the magnetic TI layer in the TI/MI bi-layer case, or two interfaces in the MI/TI/MI tri-layer case, rather than a genuine THE phenomenon arising from real-space topological texture. It is thus important to study THE with a sample structure that can readily distinguish these two scenarios.

This chapter reports the observation of THE responses in a bi-layered structure that consists of a topological insulator Bi_2Se_3 thin film grown on top of a magnetic insulator $BaFe_{12}O_{19}$ thin film. As opposed to the structures in previous experiments, this bi-layer facilitates the demonstration of *bona fide* THE phenomena in TI materials: On one hand, the $BaFe_{12}O_{19}$ film is a well-characterized, insulating, single-phase material; on the other hand, only one of the Bi_2Se_3 film surfaces is interfaced with a MI. These two facts together exclude the possibility of the coexistence of two AHE signals[224] and thereby establish the $Bi_2Se_3/BaFe_{12}O_{19}$ bilayer as a model structure for THE studies.

The magnetization in $BaFe_{12}O_{19}$ is perpendicular to the film plane, thanks to intrinsic magneto-crystalline anisotropy.[225] The Fermi level in Bi_2Se_3 is in the bulk conduction band, not in the gap opened by $BaFe_{12}O_{19}$, setting the bilayer to the AHE region, rather than the QAHE or axion insulator region. The structure showed pure AHE responses over a temperature (T) range of 80–300 K but pure THE responses at T = 2–3 K. In the temperature range of 3–80 K, the two

effects coexist, but exhibit totally opposite T dependences — as T is decreased, the AHE becomes notably weaker but the THE becomes significantly stronger. The strongest THE responses were observed for a certain narrow range of a perpendicular field ($H_\perp$). The application of an in-plane field ($H_\parallel$) can result in a substantial decrease in $H_\perp$ needed for the presence of the strong THE, but yields very weak effects on the THE strength.

Theoretical analyses show that the observed THE originates from the presence of a Dzyaloshinskii–Moriya interaction (DMI) at the interface due to strong spin-orbit coupling in Bi_2Se_3 and broken spatial inversion symmetry of the bilayer. The DMI induces a skyrmion-like topological spin texture in $BaFe_{12}O_{19}$, while the latter gives rise to the THE in Bi_2Se_3 via spin-dependent scattering at the interface. The T dependence of the THE signal is related to that of the DMI strength and the carrier density, while the T dependence of the AHE signal is associated mainly with that of the conductivity of the TSS. The weak correlation of the THE strength with $H_\parallel$ indicates the robustness of the skyrmions.

These results have important implications, as highlighted below. From a fundamental point of view, they demonstrate for the first time a genuine THE in TI materials.[224] The results are also of great technological interest in view of potential applications of skyrmions as information carriers. First, they demonstrate a new proof-of-concept approach for skyrmion realization that uses a robust TI/MI structure in a geometry that can in principle be appropriately engineered to work at technologically relevant temperatures. As discussed shortly, the spin-momentum locking of the TSS enables the presence of an interfacial DMI that is substantially stronger than in heavy metal-based structures, while strong DMI is essential for the realization of small-size skyrmions. Second, the insulating nature of MI films in general precludes direct, electrical detection of chiral spin textures in the films; this work demonstrates the feasibility of electrical reading of skyrmions

in MI thin films, thus providing a route toward proof-of-concept demonstrations of MI-based skyrmion devices.

8.2 Growth of $Bi_2Se_3/BaFe_{12}O_{19}$ heterostructure

The data presented in this article were obtained mainly on a sample that consisted of a 6-nm-thick Bi_2Se_3 film grown on the top of a 5-nm-thick $BaFe_{12}O_{19}$ film. The $BaFe_{12}O_{19}$ thin films were grown on (0001)-oriented Al_2O_3 substrates (Crystal-GMBH) using a pulsed laser deposition (PLD) system with a base pressure of 2×10^{-7} Torr. The deposition used a 248 nm KrF excimer laser, and the energy fluence of the laser beam was 1.7 J/cm^2. The target-to-substrate distance was set to 5 cm. The $BaFe_{12}O_{19}$ target was pre-ablated while the temperature was ramped up to 800 ºC. During the deposition, the oxygen pressure was kept at 75 mTorr. The laser pulse rate ramped from 1 to 5 pulse per second with equal steps during the initial 5 minutes, and it was kept at 5 pulse per second for the rest, which corresponds to a film growth rate of about 2.5 Å/min. The film was annealed in-situ at 800 ºC in 400 Torr oxygen for 10 minutes and was then cooled to room temperature at a rate of 2 ºC/min. Atomic force microscopy was used to measure the roughness of the film. As shown in Fig. 8.1, the root-mean-square (RMS) surface roughness for a 5-nm-thick $BaFe_{12}O_{19}$ thin film is 0.14±0.07 nm.

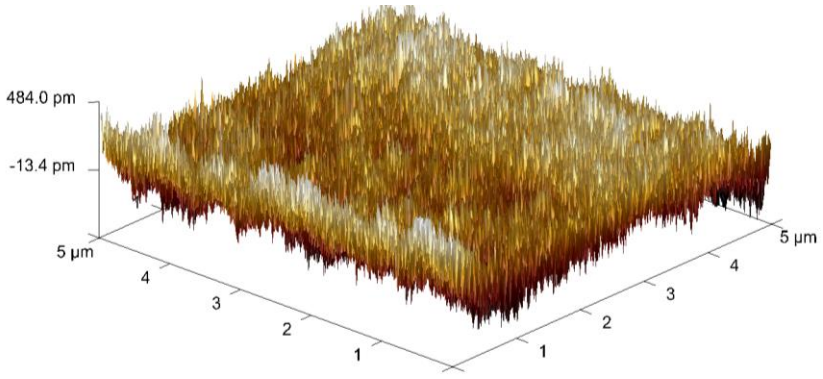

Figure 8.1. Atomic force microscopy of a 5-nm-thick $BaFe_{12}O_{19}$ film. The root-mean-square surface roughness is 0.14±0.07 nm.

A Microsense EV7 vibrating sample magnetometer (VSM) and a Quantum Design Dynacool VSM were used to measure the magnetization curves at different temperatures (T). The saturation magnetization (M_s) vs. temperature data shown in Fig. 8.2 were fitted by the Bloch law $M_s(T) = M_{s0}\left[1 - (T/T_c)^{3/2}\right]$, where M_{s0} denotes the value of M_s at T=0 K and T_c is the Curie temperature. As shown in Fig. 2, the Block law fits the data points reasonably well. The $T^{3/2}$ dependence of $M_s(T)$ indicates a three-dimensional nature of the $BaFe_{12}O_{19}$ film, as opposed to the two-dimensional nature of ultrathin films with linear T dependence. The fitting yielded T_c=767 K and M_{s0}=5.29 kG. The fitted T_c is close to the bulk value (725 K) and was used in the calculations which are described shortly.

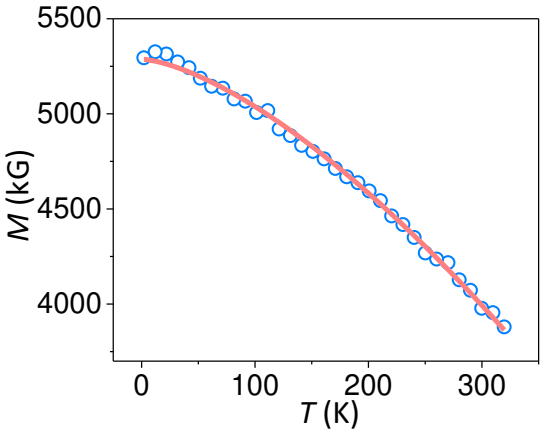

Figure 8.2. $BaFe_{12}O_{19}$ magnetization vs. temperature fitted with the Block law.

The growth of the Bi_2Se_3 film was performed by Dr. Nitin Samarth's group in Penn State, in a molecular beam epitaxy (MBE) system with a base pressure of 2×10^{-10} Torr or lower. High-purity Se (99.999%) and Bi (99.999%) targets were supplied from solid sources in Knudsen cells to maintain a flux ratio of 16.8:1.0. Prior to the growth, the $BaFe_{12}O_{19}$ film was heated to 340 °C first. The temperature was subsequently reduced to 225 °C, and at this temperature a Bi_2Se_3 buffer layer (<1 nm) was deposited for 90 seconds to facilitate growth. The film temperature was

then increased to 290 °C. Once at this temperature, Bi_2Se_3 deposition continued at 2.34 Å/min while the temperature was continually ramped to an ultimate temperature of 320 °C. After cooling the film to room temperature, a thin Te capping layer (~2 nm) was deposited, using Te (99.9999%) also from a Knudsen cell, to prevent the oxidization of the Bi_2Se_3 film.

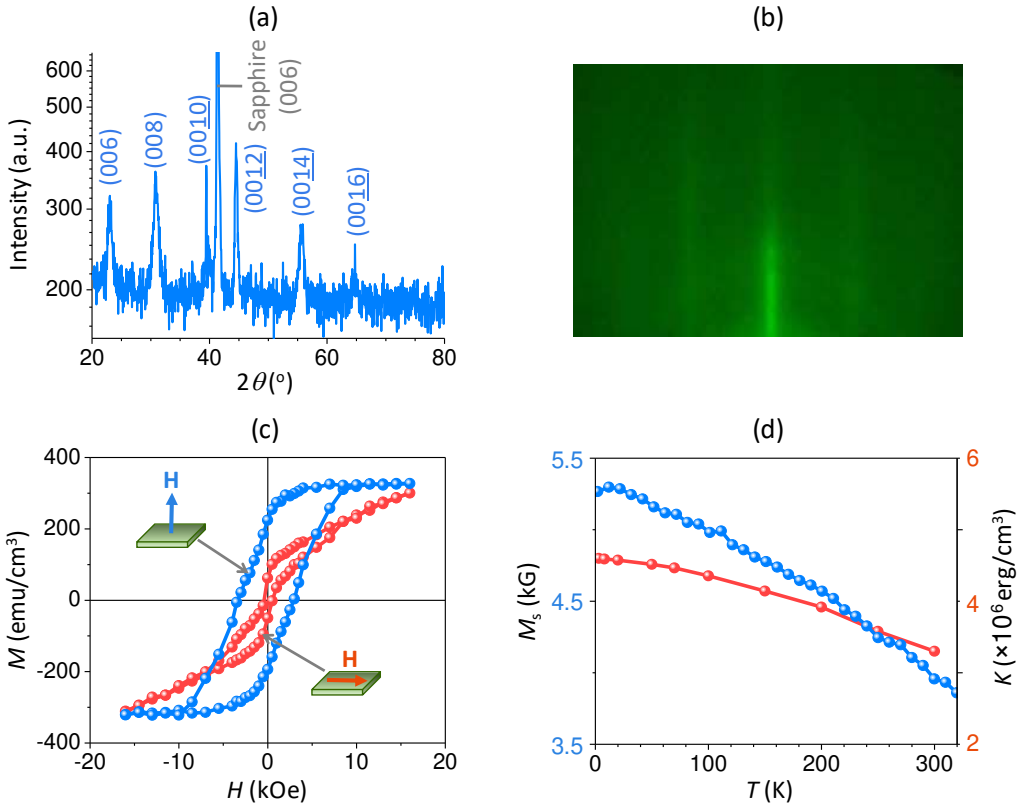

Figure 8.3. Properties of a Bi_2Se_3(6 nm)/$BaFe_{12}O_{19}$ (5 nm) sample. (a) X-ray diffraction spectrum of the $BaFe_{12}O_{19}$ film. (b) A reflection high-energy electron diffraction image obtained right after the growth of Bi_2Se_3 on $BaFe_{12}O_{19}$. (c) Magnetization (M) vs. magnetic field (H) loops measured on the $BaFe_{12}O_{19}$ film. (d) Saturation magnetization (M_s, left axis) and anisotropy constant (K, right axis) as a function of temperature (T).

Figure 8.3(a) presents an X-ray diffraction spectrum measured on the $BaFe_{12}O_{19}$ film prior to the growth of the Bi_2Se_3 film. The spectrum indicates c-axis orientation in the film, and this orientation gives rise to perpendicular magnetic anisotropy (PMA).[225,134] Figure 8.3(b) gives a reflection high-energy electron diffraction image obtained in situ right after the growth of the

Bi_2Se_3 film on the $BaFe_{12}O_{19}$ film. The image shows notable streaks that confirm the epitaxial growth of the Bi_2Se_3 film. Figure 8.3(c) presents the magnetic hysteresis loops of the sample measured under different fields, as indicated. The comparison of the two loops clearly confirms PMA in the $BaFe_{12}O_{19}$ film. For the field-in-plane configuration, the magnetization (M) reaches its saturation value (M_s) at

$$H_s = H_a - 4\pi M_s = \frac{2K}{M_s} - 4\pi M_s \tag{8.1}$$

where H_s denotes the saturation field, H_a is the effective PMA field, and K is the anisotropy constant. We determine H_s and M_s from the data in Fig. 8.3(c) and further determine H_a and K via Eq. (8.1). Figure 8.3(d) presents the $4\pi M_s$ and K values obtained for different temperatures (T). We find $4\pi M_s$=4.0 kG at T=300 K, which is slightly smaller than the bulk value (4.7 kG),[225] and K=4.6×10^6 ergs/cm^3 (or 4.6×10^5 J/m^3) at T=2 K, which is very close to the bulk value (4.4×10^6 ergs/cm^3 at T≈0 K).[226]

8.3 Device fabrication and characterization

Standard nano-fabrication procedures were used to pattern the $Bi_2Se_3/BaFe_{12}O_{19}$ bi-layers. The samples were patterned into 1000 μm×500 μm Hall bars in a photolithography system first and were then etched in an argon ion milling system. Contact pads of Ti(5 nm)/Au(150 nm) were deposited for electrical measurements.

In our previous work,[180] we calculated the sheet carrier density (n_{2D}) from the experimentally measured Hall coefficients. It was found that the Bi_2Se_3 film in the sample has a conductive bulk. The Fermi level (E_F) is in the bulk conduction band and moves towards the bottom of the conduction band with a decrease in temperature from room temperature to 2 K. Figure 8.4 presents the resistivity (ρ_{xx}) data of the sample. The data show that ρ_{xx} decreases with a decrease

in T from 300 K to about 50 K, but then increases slightly with a further decrease in T. This response indicates that in the high-T range the electron-phonon scattering overwhelms the Fermi level shifting effect, but in the low-T range the Fermi level shifting plays a major role. This result can be understood in terms of the change of phonon density with T.

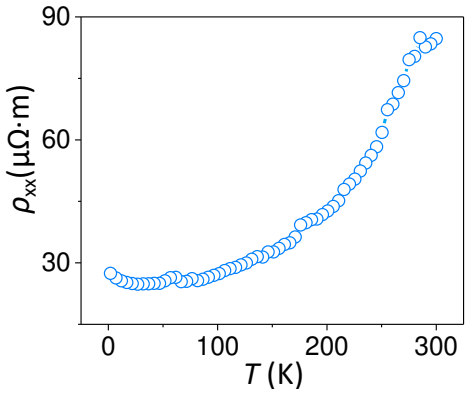

Figure 8.4. Resistivity as a function of temperature (T) for Bi_2Se_3/ $BaFe_{12}O_{19}$.

Hall measurements were conducted in two Quantum Design PPMS systems. A Keithley 6221 current source was used to generate alternating currents, and two SR830 lock-in amplifiers were used to measure the Hall voltage of the Hall bars. The alternating current with an RMS amplitude of 0.1 mA and a frequency of 186 Hz was used to measure the Hall responses.

Due to the misalignment of the contact electrodes, the longitudinal resistance R_{xx} was mixed in the Hall resistance R_{xy}, leading to an offset in the resistance axis. To remove this offset, we have performed the anti-symmetrization[216] for all the Hall curves by taking $R_{xy}^{net}(H) = \left[R_{xy}^{Raw\downarrow}(H) - R_{xy}^{Raw\uparrow}(-H)\right]/2$, where $R_{xy}^{Raw\downarrow}(H)$ and $R_{xy}^{Raw\uparrow}(H)$ are the raw Hall resistances measured by a down-swept field and an up-swept field, respectively. Similar to the data in Ref. [227], the non-monotonous THE components are obvious in our Hall data. Thus, one can see that the anti-symmetrization process is helpful in removing the resistivity offset but does not affect our results and conclusions.

8.4 THE in $Bi_2Se_3/BaFe_{12}O_{19}$ heterostructure

8.4.1 Experimental observation of THE responses

Figure 8.5 presents the main data of this work. Figure 8.5(a) illustrates the experimental configuration, while Fig. 8.5(b) gives representative Hall resistivity (ρ_H) vs. field (H) responses measured at different T, as indicated. In general, the Hall resistivity is expressed as[219,220]

$$\rho_H = \rho_{OHE} + \rho_{AHE} + \rho_{THE} = R_0 H + R_a M + \rho_{THE} \quad (8.2)$$

where ρ_{OHE}, ρ_{AHE}, and ρ_{THE} denote the OHE, AHE, and THE resistivities, respectively, and R_0 and R_a are constants. For the data in Fig. 8.5(b), the ρ_{OHE} component has already been subtracted, and the vertical axis shows the sum of the ρ_{AHE} and ρ_{THE} contributions. At T=100 K, the data show a nearly-square hysteresis loop response that is similar to the corresponding loop in Fig. 8.3(c) and is typical for the AHE.[212-214] With a decrease in T, however, a hump-like structure develops on the top of the loop, indicating the coexistence of the AHE and the THE. [223] As T is further decreased to 3 K and then 2 K, the square loop response disappears, and we observe only peak- and dip-like responses expected for the THE, [223] indicating the presence of a pure THE in the Bi_2Se_3 film.

The above-presented THE results can be attributed to the formation of skyrmions created are created by the DMI at the $Bi_2Se_3/BaFe_{12}O_{19}$ interface. The DMI in our heterostructures can arise from the combined presence of strong spin-orbit coupling in the Bi_2Se_3 film and broken inversion symmetry of the $Bi_2Se_3/BaFe_{12}O_{19}$ bilayer. This DMI competes with exchange interaction and, under certain conditions, can produce a skyrmion lattice in the $BaFe_{12}O_{19}$ film. As electrons in the Bi_2Se_3 film move along the surface at the interface and across through regions right above the skyrmions, they interact with the magnetic moments in the skyrmions and thereby experience a

fictitious magnetic field (b) from them. This fictitious field is associated with the Berry phase of the skyrmions.[219,220,227] It deflects the electrons from their otherwise straight course and results in a Hall voltage, just as an external magnetic field deflects electrons in the OHE. Note that the interaction of the conduction electrons in Bi_2Se_3 with the magnetic moments in $BaFe_{12}O_{19}$ may be achieved through spin-dependent scattering at the interface,[108] which is a non-equilibrium proximity effect, or direct coupling to the moments induced in the Bi_2Se_3 atomic layers near the interface[212,213,214,228,229] which is an equilibrium proximity effect, or both. Note also that "topology" in the topological Hall context manifests itself in the real space, as opposed to that in topological insulators which manifests itself in the momentum space.

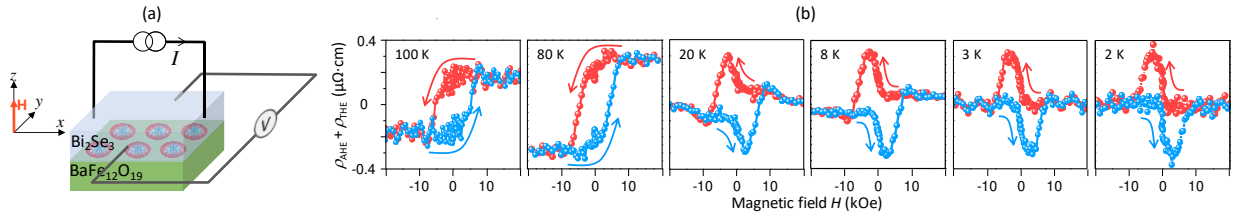

Figure 8.5. Hall properties of the Bi_2Se_3(6 nm)/$BaFe_{12}O_{19}$(5 nm) sample described in Fig. 3. (a) Experimental configuration. (b) Hall resistivity measured as a function of a perpendicular field (H) at different temperatures, as indicated. The vertical axis shows the sum of the AHE resistivity (ρ_{AHE}) and the THE resistivity (ρ_{THE}).

The physical scenario described above would naturally give rise to four important expectations. First, the THE should be present only in a certain field range. Previous work showed that the formation of skyrmions involves a fine balance between different energies, thus usually requiring an external perpendicular field of appropriate strength: if the field is too weak, one generally has a helical state; if the field is too strong, one has a usual ferromagnetic state.[230,231] Second, the strength of the THE should not be affected by a moderate in-plane field, because skyrmions, once formed, are topologically protected and are therefore expected to be robust against in-plane fields. Third, the THE should be absent above a critical or threshold temperature (T_{th}).

This expectation results from the T dependence of the DMI constant D. In general, the formation of highly packed skyrmions requires[230,231]

$$D \geq \frac{4}{\pi}\sqrt{AK} \tag{8.3}$$

where A is the exchange constant. Consider first that Eq. (8.3) is satisfied at low T. With an increase in T, both D and K decrease, but D can decrease more significantly than K and Eq. (8.3) can be violated at a certain temperature, resulting in the disappearance of the THE.

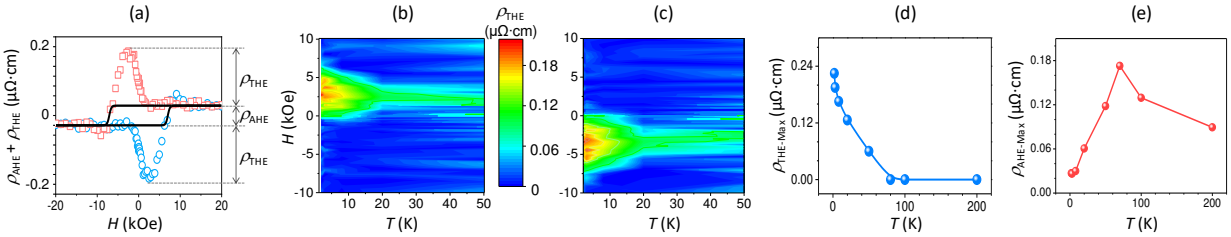

Figure 8.6. THE and AHE properties of Bi_2Se_3(6 nm)/$BaFe_{12}O_{19}$(5 nm). (a) Diagram illustrating how ρ_{THE} and ρ_{AHE} are separated. The black curves show fits to Eq. (5). (b) and (c) color maps showing ρ_{THE} (color) as a function of temperature (T, horizontal axis) and field (H, vertical axis). During the measurements, the field was swept up for (b) and swept down for (c). (d) ρ_{THE} vs. T. (e) Maximum or saturated ρ_{AHE} vs. T.

Previous experiments, for example, have found $D \propto M_S^{4.9}$ and $K \propto M_S^{2.1}$ for Pt/Co bi-layered structures, where M_s decreases with T according to Bloch's law.[232] Fourth, the THE strength is expected to decrease when T is increased towards T_{th}. This is because ρ_{THE} can be evaluated as[219,220,227]

$$\rho_{THE} = \frac{P}{en_{2D}}b = \frac{P}{en_{2D}}\frac{\Phi_0}{d^2} \tag{8.4}$$

where P is the dimensionless spin polarization rate of the Bi_2Se_3 film, e is the electron charge, n_{2D} the two-dimensional sheet carrier density in the Bi_2Se_3 film, Φ_0 is the magnetic flux quantum, and d is the average distances between the centers of two neighboring skyrmions and scales with $\frac{2\pi A}{D}$.[230] ρ_{THE} decreases with an increase in T for two reasons: (i) an increase in T leads to a decrease in D and a corresponding increase in d, and (ii) an increase in T also gives rise to an

increase in n_{2D} as shown in Ref. [239].

8.4.2 THE phase diagrams

To check the above-described expectations, we carried out several control measurements whose main features are presented in Figs. 8.6 and 8.7. Figures 8.6(b) and 8.7(c) give ρ_{THE} as a function of T and H, where ρ_{THE} is separated from ρ_{AHE} by assuming[223]

$$\rho_{AHE}(H) = \rho_{AHE-Max} \tanh \frac{H \pm H_c}{H_0} \tag{8.5}$$

for a given T, as illustrated in Fig. 8.6(a). In Eq. (8.5), H_c is the coercivity, while H_0 and $\rho_{AHE-Max}$ are fitting parameters. The red-yellow pockets in Figs. 8.6(b) and 8.6(c) indicate that the strongest THE occurs in a field range of about 2-5 kOe over T=2-10 K. Over T=30-50 K, the THE exists only in a narrow field range from about 2.5 kOe to about 5 kOe. These results evidently support the first expectation.

Figure 8.6(d) presents $\rho_{THE-Max}$ over T=2-200 K. The data in Fig. 8.6(d), together with the color maps in Figs. 8.6(b) and 8.6(c), show two important results: (i) there exists T_{th} for the onset of the THE, which is about 80 K, and (ii) as T is decreased from 80 K to 2 K, the THE strength evidently increases. These results confirm the third and fourth expectations described above.

Figure 8.7(a) shows the data measured at different field angles (θ) relative to the film normal direction. Figures 8.7(b) and 8.7(c) present $\rho_{THE-Max}$ and the perpendicular component of the field ($H_\perp = H\cos\theta$) at which $\rho_{THE-Max}$ occurs, as a function of the in-plane component of the field ($H_\parallel = H\sin\theta$). One can clearly see that an increase in $H_\parallel$ leads to a notable decrease in $H_\perp$, but only a minor change in $\rho_{THE-Max}$. The former result is consistent with the fact that skyrmion formation requires a fine balance between different energies, and a change in one energy should be accompanied by a change in another so that an energy balance is maintained; the latter indicates

the robustness of the skyrmions and thereby supports the second expectation.

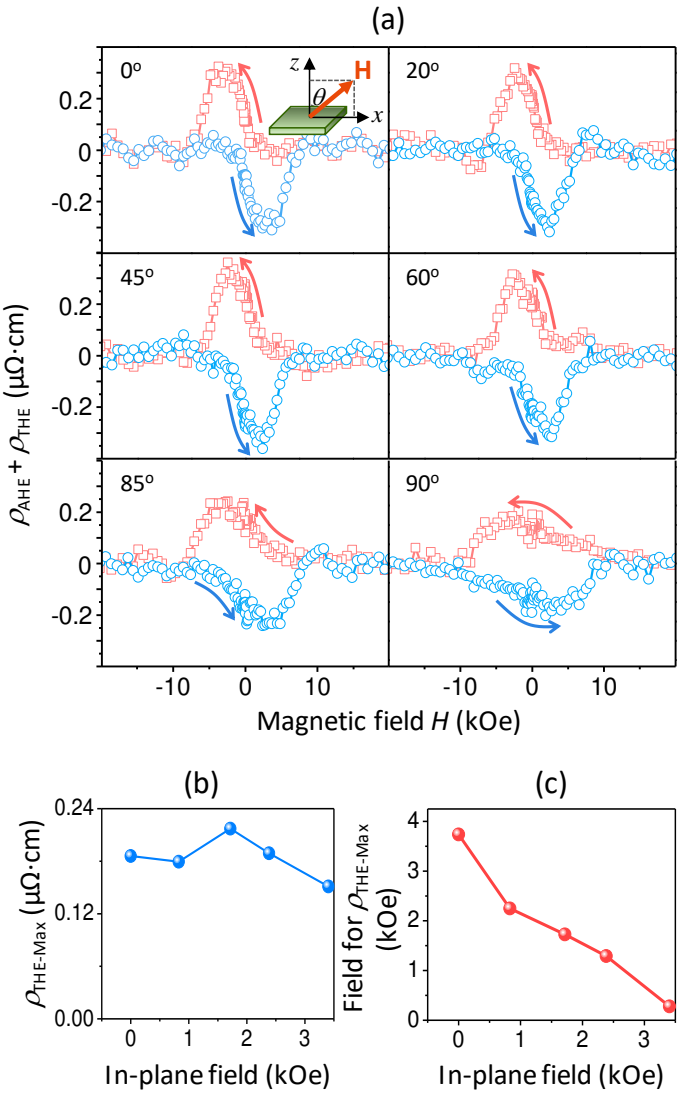

Figure 8.7. Effects of in-plane fields on the THE properties of Bi_2Se_3(6 nm)/$BaFe_{12}O_{19}$(5 nm). (a) $\rho_{AHE}+\rho_{THE}$ measured as a function of a field (H) for different field angles (θ), as indicated. (b) and (c) show $\rho_{THE\text{-}Max}$ and the corresponding perpendicular field as a function of the in-plane field.

To further support the above conjecture about the origin of the observed THE, our collaborator Dr. Shulei Zhang calculated the magnetic phase diagrams using experimentally measured M_s and K values, taking A from the literature,[84,233] and considering T-dependent D as[232]

$$D(T) = D_0 \left(\frac{M_S}{M_{S0}}\right)^n = D_0 \left[1 - \left(\frac{T}{T_c}\right)^{\frac{3}{2}}\right]^n \quad (8.6)$$

where D_0 and M_{s0} are the values of D and M_s, respectively, at T=0 K, T_c is the Curie temperature of $BaFe_{12}O_{19}$, and n equals 5 according to Ref. [232]. The calculations were based on a Ginzburg-Landau model.[230,234,235] Figure 8.8 shows one representative phase diagram that was obtained with D_0=2.0 × 10^{-3} J/m^2. This D_0 value is purposely chosen to let T_{th} in the calculated phase diagram roughly match T_{th} measured experimentally [see Fig. 8.6(b)]. The main features of the calculated diagram are very similar to the experimental diagram given in Fig. 8.6(b); this similarity evidently supports the above interpretation of the THE responses. Further, since D_0 is the only free parameter in the calculation, we expect that the actual D_0 value at the $Bi_2Se_3/BaFe_{12}O_{19}$ interface is close to 2.0×10^{-3} J/m^2. Besides, the skyrmion region in Fig. 8.8 is present at fields higher than that for the THE region in Fig. 8.6(b). The reason for this inconsistency is currently unknown; possible causes for the experimental observation of THE behavior at lower fields include heating due to the charge currents used for Hall measurements and likely contributions to the THE from skyrmion bubbles.[236]

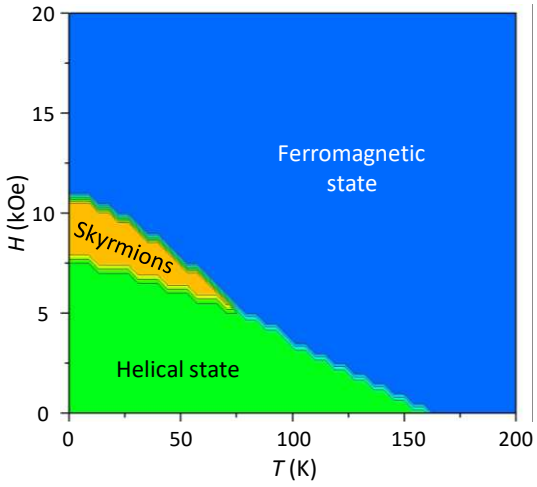

Figure 8.8. A magnetic phase diagram calculated for a $Bi_2Se_3/BaFe_{12}O_{19}$ bi-layered structure. The horizontal and vertical axes show the temperature (T) and the perpendicular field (H), respectively.

Figure 8.6(e) shows the T-dependence of $\rho_{\text{AHE-Max}}$. In general, express ρ_{AHE} can be expressed as[218]

$$\rho_{AHE} \approx \frac{\sigma_{xy}}{\sigma_{xx}^2} = \rho_{xx}^2\sigma_{xy}^{Int} + \rho_{xx}^2\sigma_{xy}^{Skew} + \rho_{xx}^2\sigma_{xy}^{SJ} \tag{8.7}$$

where $\sigma_{xx} = \frac{1}{\rho_{xx}}$ and σ_{xy} denote the longitudinal and transverse conductivities, respectively. σ_{xy}^{Int} describes the intrinsic contribution from the Berry-phase curvature in the momentum space; it depends on the band structure and is largely independent of scattering. Thus, the first term on the right side of Eq. (8.7) scales with ρ_{xx}^2. σ_{xy}^{Skew} is an extrinsic contribution due to asymmetric, skew scattering of electrons from impurities caused by spin-orbit coupling. As σ_{xy}^{Skew} is proportional to $\frac{1}{\rho_{xx}}$, the second term scales with ρ_{xx}. σ_{xy}^{SJ} is associated with side-jump scattering from impurities; it is extrinsic as σ_{xy}^{Skew}, but is independent of ρ_{xx} as σ_{xy}^{Int}. Thus, the third term scales with ρ_{xx}^2. As T is varied from 80 K to 2 K, the conductivity of the TSS increases due to weaker electron-phonon scattering, ρ_{xx} decreases, and ρ_{AHE} also decreases as shown in Fig. 8.6(e). The data in Fig. 8.6(e) also show that ρ_{AHE} decreases when T is increased from 80 K. The actual reason for this is currently unknown, and possible reasons include that the AHE in Bi_2Se_3 depends on the gap opening at the Dirac point or the presence of induced moments near the interface due to the perpendicular magnetization in $BaFe_{12}O_{19}$, while the magnetization in $BaFe_{12}O_{19}$ decreases as T is increased, as shown in Fig. 8.3(d).

Previous work shows that a bipolar pulse was able to generate and eliminate (or suppress) skyrmions.[237] In our work, we found that DC currents can change the THE magnitude in the Bi_2Se_3/ $BaFe_{12}O_{19}$ samples. Figure 8.9 shows the THE magnitude as a function of a perpendicular magnetic field measured with opposite current polarities in Bi_2Se_3(6 nm)/$BaFe_{12}O_{19}$(5 nm) at T=5K and θ=20°. A 0.8-mA DC current leads to a stronger THE response, while a -0.8mA DC

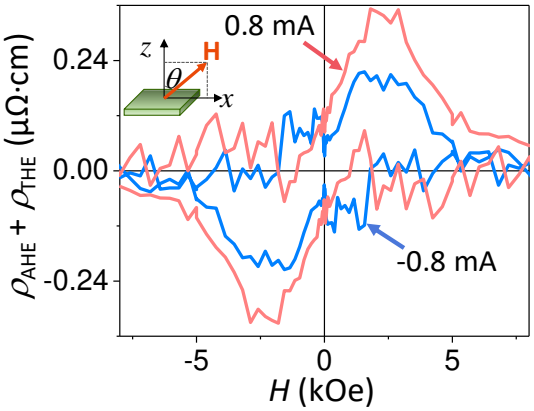

Figure 8.9. Effects of DC current polarities on the THE properties of Bi_2Se_3(6 nm)/$BaFe_{12}O_{19}$(5 nm), measured at T=5 K and θ=20°.

current leads to a weaker response. If we normalize the change of the resistivity to the current density, we can produce a THE response of about 2.4 μΩ·cm for a current density of 1 MA/cm, which is more efficient than the previous method with 0.005 μΩ·cm for a current density of 1 MA/cm. At variance with the nonlinear Hall resistivity discovered recently in a single Bi_2Se_3 layer which is linearly proportional to the external field,[238] the nonlinear Hall effect shown in Fig. 8.9 exhibits a different field dependence which may be associated with the presence of the skyrmions.

8.5 Calculation of magnetic phase diagrams

The phase diagram calculations were performed by Dr. Shulei Zhang. The calculations assume that the film lies in the *xy* plane, and the magnetization **M** is uniform along the *z* direction and is therefore a function of only *x* and *y*, i.e., **M**=**M**(*x*,*y*). In a Ginzburg-Landau theory,[230,234,235] the magnetic free energy density functional of the ferromagnetic thin film with perpendicular uniaxial anisotropy can be written as

$$f[\mathbf{m}] = A(\nabla \mathbf{m})^2 - K\mathrm{m}_z^2 + f_{demag}[\mathbf{m}] + f_{DMI}[\mathbf{m}] + f_0 \qquad (8.8)$$

where A and K are the exchange stiffness and the uniaxial anisotropy constant, respectively; $\mathbf{m} = \mathbf{M}/M_0$ with M_0 the saturation magnetization at T=0 K; and f_0 determines the magnitude of $\mathbf{m}$ which is confined to the saturation magnetization $M_s(T)$. In the thin film approximation,[239] the demagnetization energy density is given by $f_{demag} = K_d \mathrm{m}_z^2$ where $K_d = \frac{1}{2}\mu_0 M_0^2$ with μ_0 the magnetic permeability. In the continuum model, the energy density of the interfacial Dzyaloshinskii-Moriya interaction (DMI) is given by[239]

$$f_{DMI}[\mathbf{m}] = Dt \sum_{u=x,y} (\hat{\boldsymbol{z}} \times \hat{\boldsymbol{u}}) \cdot (\mathbf{m} \times \partial_u \mathbf{m}) \tag{8.9}$$

where D is a constant coefficient characterizing the strength of the DMI and t is the film thickness. We also take into account the temperature (T) dependence of the interfacial DMI by letting[232]

$$D(T) = D_0 \left(\frac{M_S}{M_{S0}}\right)^n = D_0 \left[1 - \left(\frac{T}{T_c}\right)^{\frac{3}{2}}\right]^n \tag{8.10}$$

where D_0 and M_{S0} are the values of D and M_S, respectively, at T=0 K, T_c is the Curie temperature of $BaFe_{12}O_{19}$, and n takes 5 according to Ref. [232].

To simplify the calculation, we restrict ourselves to several typical magnetic states including helices, stripe domains, a non-chiral bubble lattice, and a hexagonal skyrmion lattice (SkX). Mathematically, these magnetic states can be approximately described by the following spatial profile of the magnetization (a superposition of three helices)

$$\mathbf{m}(\boldsymbol{r}) = \sum_{i=1,2,3} m_{i,\perp} \hat{\boldsymbol{z}} cos(\boldsymbol{k}_i \cdot \boldsymbol{r}) + m_{i,\parallel} \left(\hat{\boldsymbol{z}} \times \hat{\boldsymbol{k}}_i\right) sin(\boldsymbol{k}_i \cdot \boldsymbol{r}) \tag{8.11}$$

where the wave vectors of the three helices $\boldsymbol{k}_i$ (i=1,2,3) are all in the plane of the layer and form an angle of 120 degrees with each other, and $m_{i,\perp}$ and $m_{i,\parallel}$ are the perpendicular and in-plane magnetization components, respectively, of the i-th helix.

Based on the Ginzurg-Landau formulation described, we can compute the magnetic phase diagrams with the materials parameters pertaining to the BaM/Bi_2Se_3 bilayer. The results are

summarized in Fig. 8.10. They clearly show that the DMI constant D play important roles in the formation of a highly packed skyrmion lattice (SkX). For example, the upper temperature (T) limit of the SkX region increases with an increase in D. This result is generally consistent with the condition for SkX formation, namely, $D \geq \frac{4}{\pi}\sqrt{AK}$, which is discussed in detail previously. Figure 8.10. shows magnetic phase diagrams in the plane of the out-of-plane magnetic field H_z and temperature T for varying materials parameters. Materials parameters used in the calculation are as follows (unless otherwise stated): the zero-temperature saturation magnetization $M_0 = 421\ \mathrm{emu \cdot cm^{-3}}$, the Curie temperature of $BaFe_{12}O_{19}$ $T_c = 767\ \mathrm{K}$, the exchange coupling constant of $BaFe_{12}O_{19}$ $A = 6.4 \times 10^{-7}\ \mathrm{erg/cm}$, the perpendicular anisotropy constant of $BaFe_{12}O_{19}$ $K = 3.4 \times 10^5\ \mathrm{J \cdot m^{-3}}$, and $n_D = 5.0$. Note that M_0, T_c, and K were determined experimentally; A is from literatures,[84,233] and n is from a previous experimental study.[244]

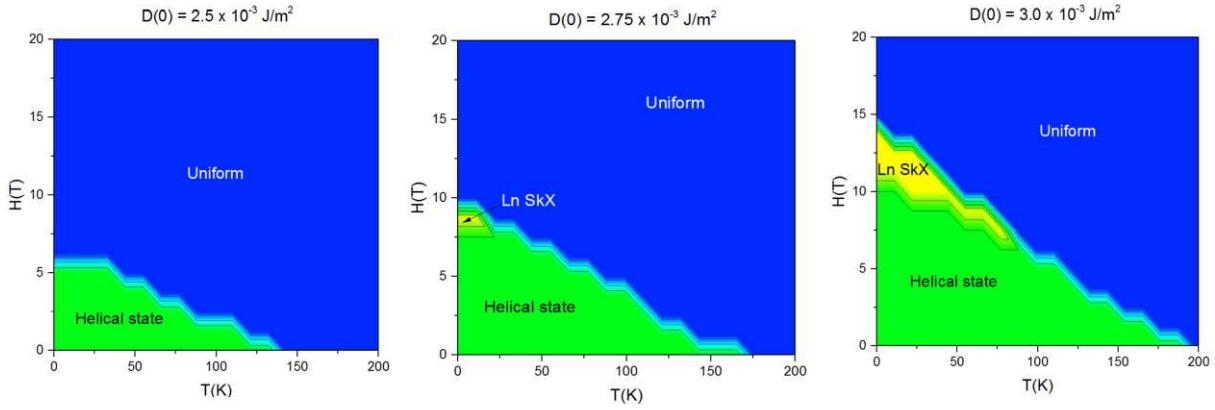

Figure 8.10. Magnetic phase diagrams in the plane of the out-of-plane magnetic field H_z and temperature T for varying materials parameters.

Reference [224] investigated the anomalous Hall effect in the magnetically doped topological insulator $(V,Bi,Sb)_2Te_3$, in which they concluded that the "topological Hall effect"-like curves are

due to two ferromagnetic components originating from the surface and bulk of the magnetic topological insulator, respectively. Thus, a careful examination of "topological Hall effect"-like curves is necessary.

In our experiment, this mechanism however does not work in our case because (1) BaM is insulating and the anomalous Hall effect and topological Hall effect signals are only from the interface, and (2) we have only one interface, not two interfaces.

The interfacial diffusion is also very unlikely in our structures because $BaFe_{12}O_{19}$ is a stable oxide and the growth of Bi_2Se_3 was done at relatively low temperatures. Further, the BaM film itself does not have two phases, as confirmed by the magnetization vs. temperature data as shown in Fig. 8.2 which can be fitted with the Block law. The gradual change of the anisotropy constant K with temperature (Fig. 8.6(d)) also confirms that there is only one magnetic phase in the $BaFe_{12}O_{19}$ sample.

8.6 Conclusions and outlook

In closing, four important remarks should be made about the results presented above. First, since the DMI strength directly dictates the skyrmion size, it is interesting to compare the DMI strength in the material system concerned in this work with that in previous work. In consideration of the interfacial nature of the DMI and the bulk nature of the skyrmions (i.e. being uniform across the entire thickness of the $BaFe_{12}O_{19}$ film), one can evaluate the DMI strength by defining a DMI energy parameter as[240]

$$E_{DMI} = Dt \tag{8.12}$$

where t is the thickness of the MI layer. Based on previously reported D and t values, one obtains E_{DMI}≈1.17 pJ/m for Pt/Co/Ta,[241] 0.96 pJ/m for Ir/Co/Pt,[242] 2.17 pJ/m for Pt/Co/MgO,[240] 0.44 pJ/m for W/CoFeB/Mgo,[243] and 0.02 pJ/m for $Pt/Tm_3Fe_5O_{12}$.[222] In contrast, one has E_{DMI}≈10.0

pJ/m in this work. Thus, one can clearly see that the DMI strength in $Bi_2Se_3/BaFe_{12}O_{19}$ is about one or two orders of magnitude higher than that in heavy metal-based systems. Such a strong effect most likely originates from the intrinsic spin-momentum locking of the TSS in Bi_2Se_3. Second, although $\rho_{THE\text{-}Max}$ occurs at a non-zero field, there are still THE responses at zero field. For example, ρ_{THE} at H=0 is about 50% of $\rho_{THE\text{-}Max}$ at T=2 K, as shown in Fig. 8.5(b). Such zero-field THE responses are of practical significance. Third, although the THE has been widely accepted as a unique signature of magnetic skyrmions, future work is of great interest that directly probes chiral spin textures in skyrmions in TI/MI bi-layers via the use of Lorentz transmission electron microscopy, [244] magnetic force microscopy, [245] or scanning transmission X-ray microscopy.[241] Finally, the threshold temperature shown in Fig. 8.6 is about 80 K, but one can likely extend it to room temperature by reducing K of the $BaFe_{12}O_{19}$ film via doping, for example, scandium.[246]

This work has been presented in a manuscript entitled "Topological Hall Effect in a Topological Insulator Interfaced with a Magnetic Insulator". The full author list is Peng Li, Jinjun Ding, Steven S.-L. Zhang, James Kally, Timothy Pillsbury, Olle G. Heinonen, Gaurab Rimal, Chong Bi, August DeMann, Stuart B. Field, Weigang Wang, Jinke Tang, J. S. Jiang, Axel Hoffmann, Nitin Samarth and Mingzhong Wu. Peng Li prepared $BaFe_{12}O_{19}$ thin film and performed electrical transport measurements. Jinjun Ding performed electrical transport measurements and analyzed the data. Steven Steven S.-L. Zhang performed numerical calculations. James Kally and Timothy Pillsbury prepared the Bi_2Se_3 thin film. Olle G. Heinonen, Gaurab Rimal and Chong Bi helped with electrical transport measurements. August DeMann helped with photolithography.

CHAPTER 9 SUMMARY AND OUTLOOK

9.1 Summary

This dissertation presents comprehensive, systematic studies on yttrium iron garnet thin film development by magnetron sputtering techniques, including control parameter optimization, thin film characterization, and development of yttrium iron garnet films with perpendicular anisotropy. Demonstrations of spintronics-related experiments and research, such as spin-orbit torque-induced magnetization switching are presented and discussed.

This dissertation also presents comprehensive, pioneering studies on α-Sn thin films grown on InSb substrates as well as on Si substrates using magnetron sputtering techniques. The dynamic properties of NiFe/α-Sn is studied and the effects of the topological surface states of Dirac semimetal α-Sn are discussed. Electric transport properties of topological Dirac semimetal α -Sn, the mechanism of current-induced magnetization switching, and the switching efficiency are analyzed and discussed in detail. Current-induced switching is achieved in a rectangular structure consisting of a 6-nm-thick film of topological Dirac semimetal α-Sn and a 2-nm-thick ferromagnetic CoFeB film.

A topological Hall effect is observed in a bi-layered structure that consists of a topological insulator Bi_2Se_3 thin film grown on top of a magnetic insulator $BaFe_{12}O_{19}$ thin film. Details about the growth of $BaFe_{12}O_{19}$ thin films, the temperature dependence of topological Hall effect, the calculation of topological Hall effect phase diagrams are presented and discussed.

9.2 Outlook

The last decade witnessed the increasing interest of utilizing yttrium iron garnet thin films as well as topological materials in spintronics–related fundamental studies and applications. The research topics and arguments in this dissertation provide a good reference for yttrium iron garnet and topological Dirac semimetal α-Sn thin film development with magnetron sputtering techniques. Topics that are relevant to the studies in this dissertation and are of great interest for future study may include the following:

(1) Optimization of the sputtering growth processes for the realization of nm-thick PMA YIG films with even lower damping;

(2) Measurements of speed of SOT-induced domain wall motion in PMA YIG thin films;

(3) Angle-resolved photoemission spectroscopy study of topological Dirac semimetal α-Sn thin films to gain more insights on the electronic structure;

(4) Study of spin pumping effects associated with Fermi arc states in topological Dirac semimetal α-Sn thin films;

(5) Exploration of the possibilities of realizing α-Sn thin films with an even higher SOT efficiency by the use of strain engineering to modify the band structure and voltage gating to tune the Fermi level in α-Sn thin films;

(6) Lorentz transmission electron microscopy imaging of possible magnetic skyrmions in magnetic insulator/topological insulator heterostructures;

(7) Extending the Topological Hall effect phase diagram to room temperature by reducing anisotropy of the $BaFe_{12}O_{19}$ film via doping, which is important for potential applications of magnetic skyrmions.

REFERENCES

[1] Y. Kajiwara, K. Harii, S. Takahashi, J. Ohe, K. Uchida, M. Mizuguchi, H. Umezawa, H. Kawai, K. Ando, K. Takanashi, S. Maekawa, and E. Saitoh, Transmission of electrical signals by spin-wave interconversion in a magnetic insulator. *Nature* **464**, 262 (2010).

[2] K. Uchida, J. Xiao, H. Adachi, J. Ohe, S. Takahashi, J. Ieda, T. Ota, Y. Kajiwara, H. Umezawa, H. Kawai, G. E. W. Bauer, S. Maekawa, and E. Saitoh, Spin Seebeck insulator. *Nat. Mater.* **9**, 894 (2010).

[3] J. Xiao, G. E. W. Bauer, K. Uchida, E. Saitoh, and S. Maekawa, Theory of magnon-driven spin Seebeck effect. *Phys. Rev. B* **81**, 214418 (2010).

[4] C. W. Sandweg, Y. Kajiwara, A. V. Chumak, A. A. Serga, V. I. Vasyuchka, and M. B. Jungfleisch, Saitoh, and B. Hillebands, Spin Pumping by Parametrically Excited Exchange Magnons. *Phys. Rev. Lett.* **106**, 216601 (2011).

[5] B. Heinrich, C. Burrowes, E. Montoya, B. Kardasz, E. Girt, Y. -Y. Song, Y. Sun, and M. Wu, Spin Pumping at the Magnetic Insulator (YIG)/Normal Metal (Au) Interfaces. *Phys. Rev. Lett.* **107**, 066604 (2011).

[6] H. Kurebayashi. O, Dzyapko, V. E. Demidov, D. Fang, A. J. Ferguson, and S. O. Demokritov, Controlled enhancement of spin-current emission by three-magnon splitting. *Nat. Mater.* **10**, 660 (2011).

[7] S. Y. Huang, X. Fan, D. Qu, Y. P. Chen, W. G. Wang, J. Wu, T. Y. Chen, J. Q. Xiao, and C. L. Chien, Transport Magnetic Proximity Effects in Platinum. *Phys. Rev. Lett.* **109**, 107204 (2012).

[8] H. Nakayama, M. Althammer, Y. -T. Chen, K. Uchida, Y. Kajiwara, D. Kikuchi, T. Ohtani, S. Geprags, M. Opel S. Takahashi, R. Gross, G. E. W. Bauer, S. T. B. Goennenwein, and E. Saitoh, Spin Hall Magnetoresistance Induced by a Nonequilibrium Proximity Effect. *Phys. Rev. Lett.* **110**, 206601 (2013).

[9] Y. Sun and M. Wu, Yttrium iron garnet nano films: epitaxial growth, spin-pumping efficiency, and Pt-capping-caused damping. *Solid State Phys.* **64**, 157-191 Academic Press, Burlington (2013).

[10] Y. Sun, H. Song, Y-Y. Chang, M. Kabatek, M. Jantz, W. Schneider, M. Wu, H. Schultheiss, and A. Hoffmann, Growth and ferromagnetic resonance properties of nanometer-thick yttrium iron

garnet films. *Appl. Phys. Lett.* **101**, 152405 (2012).

[11] J. Ding, T. Liu, H. Chang, and M. Wu, Sputtering Growth of Low-Damping Yttrium Iron Garnet Thin Films. *IEEE Magn. Lett.* **11**, 5502305 (2020).

[12] Y. Chen, E. Cogulu, D. Roy, J. Ding, J. B. Mohammadi, P. G. Kotula, N. A. Missert, M. Wu, and A. D. Kent, Spin transport in an insulating ferrimagnetic-antiferromagnetic-ferrimagnetic trilayer as a function of temperature. *AIP Adv.* **9**, 105319 (2019).

[13] R. Freeman, R. Lemasters, T. Kalejaiye, F. Wang, G. Chen, J. Ding, M. Wu, V.E. Demidov, S. O. Demokritov, H. Harutyunyan, and S. Urazhdin, Brillouin Light Scattering of Spin Waves Inaccessible with Free-Space Light. arXiv:2004.05314 (2020).

[14] J. Ding, C. Liu, Y. Zhang, U. Erugu, Z. Quan, R. Yu, E. McCollum, S. Mo, S. Yang, H. Ding, X. Xu, J. Tang, X. Yang, and M. Wu, Nanometer-Thick Yttrium Iron Garnet Films with Perpendicular Anisotropy and Low Damping. *Phys. Rev. Appl.* **14**, 014017 (2020).

[15] B. Heinrich and J. A. C. Bland, Ultrathin Magnetic Structures: Fundamentals of Nanomagnetism, Springer, Berlin (2005).

[16] R. Urban, G. Woltersdorf, and B. Heinrich, Gilbert damping in single and multilayer ultrathin films: Role of interfaces in nonlocal spin dynamics. *Phys. Rev. Lett.* **87**, 217204 (2001).

[17] Y. Tserkovnyak, A. Brataas, and G. E.W. Bauer, Enhanced Gilbert damping in thin ferromagnetic films. *Phys. Rev. Lett.* **88**, 117601 (2002).

[18] J. Ding, C. Liu, R. Yu, U. Erugu, J. Tang, H. Ding, H. Chen, and M. Wu, Topological surface states-caused large damping enhancement in Dirac semimetal-ferromagnetic metal layered structures. *Phys. Rev. Lett.*, under review (2020).

[19] J. Ding, C. Liu, V. Kalappattil, Y. Zhang, O. Mosendz, U. Erugu, R. Yu, J. Tian, A. DeMann, S. B. Field, X. Yang, H. Ding, J. Tang, B. Terris, A. Fert, H. Chen, and M. Wu, Magnetization Switching using Surface States in a Topological Dirac Semimetal. *Science Advances*, under review (2020).

[20] J. Ding, P. Li, S. S.-L. Zhang, J. Kally, T. Pillsbury, G. Rimal, C. Bi, A. DeMann, S. B. Field, W. Wang, J. Tang, J. S. Jiang, O. G. Heinonen, A. Hoffmann, N. Samarth, and M. Wu, Magnetization Switching using Surface States in a Topological Dirac Semimetal. *Phys. Rev. Lett.*, under review (2020).

[21] F. M. Penning, Optogalvanic effects in the obstructed glow discharge. *Physica* **8**, 137 (1928).

[22] F. M. Penning, Kinetic Ejection of Electrons from Solids. *Proc. Roy. Soc. Amst.* **31**, 14 (1928).

[23] F. M. Penning, über die Zusammenstōße zwischen positiven Ionen und Atomen. *Proc. Roy. Soc. Amst.* **33**, 841 (1930).

[24] I. I. Aksenov, V. A. Belous, V. G. Padalka, and V. M. Khoroshikh, Vapor Deposition Processing. *Phys. Chem. Mater. Process.* **6**, 89 (1977).

[25] M. S. P. Lucas, J. H. A. Owen, W. C. Stewart, and C. R. Vail, Cathodic Arcs: From Fractal Spots to Energetic Condensation. *Rev. Sci. Instrum.* **32**, 203 (1961).

[26] A. A. Snaper, Arc deposition process and apparatus. US **3**,625,848 (1971).

[27] F. Paschen, Annalen der Physik und Chemie. *Annalen der Physik.* **273**, 69 (1889).

[28] C. Poole Jr., Electron Spin Resonance: A Comprehensive Treatise on Experimental Techniqus. Interscience Publishers, New York (1967).

[29] M. Weissbluth, Atoms and Molecules, Elsevier (2012).

[30] M. Z. Hasan and C. L. Kane, Colloquium: Topological insulators. *Rev. Mod. Phys.* **82**, 3045 (2010).

[31] X.-L. Qi and S.-C. Zhang, Topological insulators and superconductors. *Rev. Mod. Phys.* **83**, 1057 (2011).

[32] J. Moore, The birth of topological insulators. *Nature* **464**, 194–198 (2010).

[33] A. R. Mellnik, J. S. Lee, A. Richardella, J. L. Grab, P. J. Mintun, M. H. Fischer, A. Vaezi, A. Manchon, E.-A. Kim, N. Samarth, and D. C. Ralph, Spin-transfer torque generated by a topological insulator. *Nature* **511**, 449-451 (2014).

[34] C.-Z. Xu, Y.-H. Chan, Y. Chen, P. Chen, X. Wang, C. Dejoie, M.-H. Wong, J. A. Hlevyack, H. Ryu, H.-Y. Kee, N. Tamura, M.-Y. Chou, Z. Hussain, S.-K. Mo, and T.-C. Chiang, Elemental Topological Dirac Semimetal: α-Sn on InSb (111). *Phys. Rev. Lett*. **118**, 146402 (2017).

[35] S. M. Young, S. Zaheer, J. C. Y. Teo, C. L. Kane, E. J. Mele, and A. M. Rappe, Dirac semimetal in three dimensions. *Phys. Rev. Lett.* **108**, 140405 (2012).

[36] Z. Wang, Y. Sun, X.-Q. Chen, C. Franchini, G. Xu, H. Weng, X. Dai, and Z. Fang, Dirac semimetal and topological phase transitions in A_3Bi(A= Na, K, Rb). *Phys. Rev. B* 85, 195320 (2012).

[37] Z. Wang, H. Weng, Q. Wu, X. Dai, and Z. Fang, Three-dimensional Dirac semimetal and quantum transport in CdAs. *Phys. Rev. B* **88**, 125427 (2013).

[38] B. Yang and N. Nagaosa, Classification of stable three-dimensional Dirac semimetals with nontrivial topology. *Nat. Commun.* **5**, 4898 (2014).

[39] S.-Y. Xu, C. Liu, S. K. Kushwaha, R. Sankar, J. W. Krizan, I. Belopolski, M. Neupane, G. Bian, N. Alidoust, T.-R. Chang, H.-T. Jeng, C.-Y. Huang, W.-F. Tsai, H. Lin, P. P. Shibayev, F.-C. Chou, R. J. Cava, and M. Z. Hasan, Discovery of a Weyl fermion semimetal and topological Fermi arcs. *Science* **347**, 294 (2015).

[40] J. Feng, Y. Pang, D. Wu, Z. Wang, H. Weng, J. Li, X. Dai, Z. Fang, Y. Shi, and L. Lu, Large linear magnetoresistance in Dirac semimetal with Fermi surfaces close to the Dirac points. *Phys. Rev. B* **92**, 081306(R) (2015).

[41] T. Liang, Q. Gibson, M. N. Ali, M. Liu, R. J. Cava, and N. P. Ong, Ultrahigh mobility and giant magnetoresistance in the Dirac semimetal Cd_3As_2. *Nat. Mater.* **14**, 280 (2014).

[42] J. Xiong, S. K. Kushwaha, T. Liang, J. W. Krizan, M. Hirschberger, W. Wang, R. J. Cava, and N. P. Ong, Evidence for the chiral anomaly in the Dirac semimetal Na_3Bi. *Science* **350**, 413 (2015).

[43] P. J. W. Moll, N. L. Nair, T. Helm, A. C. Potter, I. Kimchi, A. Vishwanath, and J. G. Analytis, Transport evidence for Fermi-arc-mediated chirality transfer in the Dirac semimetal Cd_3As_2. *Nature* **535**, 266 (2016).

[44] S. Borisenko, Q. Gibson, D. Evtushinsky, V. Zabolotnyy, B. Büchner, and R. J. Cava, Experimental realization of a three-dimensional Dirac semimetal. *Phys. Rev. Lett.* **113**, 27603 (2014).

[45] Z. K. Liu, J. Jiang, B. Zhou, Z. J. Wang, Y. Zhang, H. M. Weng, D. Prabhakaran, S.-K. Mo, H. Peng, P. Dudin, T. Kim, M. Hoesch, Z. Fang, X. Dai, Z. X. Shen, D. L. Feng, Z. Hussain, and Y. L. Chen, A stable three-dimensional topological Dirac semimetal Cd_3As_2. *Nat. Mater.* **13**, 677 (2014).

[46] H. Huang and F. Liu, Tensile strained gray tin: Dirac semimetal for observing negative magnetoresistance with Shubnikov–de Haas oscillations. *Phys. Rev. B* **95**, (2017).

[47] K. Ojima and Y. Taneda, Gray tin observed by high-resolution electron microscopy. *J. Mater. Sci. Lett.* **10**, 9 (1991).

[48] T. Osaka, H. Omi, K. Yamamoto, and A. Ohtake, Surface phase transition and interface interaction in the α-Sn/InSb{111} system. *Phys. Rev. B* **50**, 7567 (1994).

[49] H. Huang, and F. Liu, Tensile strained gray tin: Dirac semimetal for observing negative magnetoresistance with Shubnikov-de Haas oscillations. *Phys. Rev. B* **95**, 201101(R) (2017).

[50] D. Zhang, H. Wang, J. Ruan, G. Yao, and H. Zhang, Engineering topological phases in the

Luttinger semimetal α-Sn. *Phys. Rev. B* **97**, 195139 (2018).

[51] S. C. Zhang, and X. L. Qi, A fine point on topological insulators. *Phys. Today* **63**, 12 (2010).

[52] Z. Zhu, Y. Cheng, and U. Schwingenschlögl, Band inversion mechanism in topological insulators: A guideline for materials design, *Phys. Rev. B* **85**, 235401 (2012).

[53] A. Barfuss, L. Dudy, M. R. Scholz, H. Roth, P. Höpfner, C. Blumenstein, G. Landolt, J. H. Di, N. C. Plumb, M. Radovic, A. Bostwick, E. Rotenberg, A. Fleszar, G. Bihlmayer, D. Wortmann, G. Li, W. Hanke, R. Claessen, and J. Schäfer, Elemental topological insulator with tunable Fermi level: strained α-Sn on InSb (001), *Phys. Rev. Lett.* **111**, 157205 (2013).

[54] Yoshiyuki Ohtsubo, Patrick Le Fèvre, Francois Bertran, and Amina Taleb-Ibrahimi, Dirac cone with helical spin polarization in ultrathin α-Sn (001) films, *Phys. Rev. Lett.* **111**, 216401 (2013).

[55] J.-C. Rojas-Sánchez, S. Oyarzún, Y. Fu, A. Marty, C. Vergnaud, S. Gambarelli, L. Vila, M. Jamet, Y. Ohtsubo, A. Taleb-Ibrahimi, P. Le Fèvre, F. Bertran, N. Reyren, J.-M. George, and A. Fert, Spin to charge conversion at room temperature by spin pumping into a new type of topological insulator: *α*-Sn films. *Phys. Rev. Lett*. **116**, 096602 (2016).

[56] M. P. Horvath, Microwave applications of soft ferrites. *J. Magn. Magn. Mater.* **215**, 171-183 (2000).

[57] V. G. Harris, A. Geilerab, Y. Chen, S. D. Yoon, M. Wu, A. Yang, Z. Chen, P. He, P. V. Parimi, X. Zuo, C. E. Patton, M. Abe, O. Acher, and C. Vittoriaab, Recent advances in processing and applications of microwave ferrites. *J. Magn. Magn. Mater.* **321**, 2035-2047 (2009).

[58] B. Arkook, C. Safranski, R. Rodriguez, I. N. Krivorotov, T. Schneider, K. Lenz, J. Lindner, H. Chang, M. Wu, Y. Tserkovnyak, and I. Barsukov, Thermally driven two-magnet nano-oscillator with large spin-charge conversion. arXiv:1909.12445 (2019).

[59] T. Goto, T. Yoshimoto, B. Iwamoto, K. Shimada, C. A. Ross, K. Sekiguchi, A. B. Granovsky, Y. Nakamura, H. Uchida, and M. Inoue, Three port logic gate using forward volume spin wave interference in a thin yttrium iron garnet film. *Sci. Rep.* **9**, 16472 (2019).

[60] K. O. d'Allivy, A. Anane, R. Bernard, Y. J. Ben, C. Hahn, A-H. Molpeceres, C. Carretero, E. Jacquet, C. Deranlot, P. Bortolotti, R. Lebourgois, J-C. Mage, G. de Loubens, O. Klein, V. Cros, and A. Fert, Inverse spin Hall effect in nanometer-thick yttrium iron garnet/Pt system *Appl. Phys. Lett.* **103**, 082408 (2013).

[61] T. Liu, H. Chang, V. Vlaminck, Y. Sun, M. Kabatek, A. Hoffmann, L. Deng, and M. Wu, Ferromagnetic resonance of sputtered yttrium iron garnet nanometer films. *J. Appl. Phys.* 115,

17A501 (2014).

[62] P. Pirro, T. Brächer, A. V. Chumak, B. Lägel, C. Dubs, O. Surzhenko, P. Görnert, B. Leven, and B. Hillebrands, Spin-wave excitation and propagation in microstructured waveguides of yttrium iron garnet/Pt bilayers. *Appl. Phys. Lett.* **104**, 012402 (2014).

[63] J. Lustikova, Y. Shiomi, Z. Qiu, T. Kikkawa, R. Iguchi, K. Uchida, and E. Saitoh, Spin current generation from sputtered $Y_3Fe_5O_{12}$ films. *J. Appl. Phys.* **116**, 153902 (2014).

[64] H. Chang, P. Li, W. Zhang, T. Liu, A. Hoffmann, L. Deng, and M. Wu, Nanometer-Thick Yttrium Iron Garnet Films With Extremely Low Damping. *IEEE Magn. Lett.* **5**, 2350958 (2014).

[65] H. Wang, C. Du, P. C. Hammel, and F. Yang, Strain-tunable magnetocrystalline anisotropy in epitaxial $Y_3Fe_5O_{12}$ thin films. *Phys. Rev. B* **89**, 134404 (2014).

[66] B. M. Howe, S. Emori, H. M. Jeon, T. M. Oxholm, J. G. Jones, K. Mahalingam, Y. Zhuang, N. X. Sun, and G. J. Brown, Pseudomorphic Yttrium Iron Garnet Thin Films with Low Damping and Inhomogeneous Linewidth Broadening. *IEEE Magn. Lett.* **6**, 2449260 (2015).

[67] C. Hauser, T. Richter, N. Homonnay, C. Eisenschmidt, M. Qaid, H. Deniz, D. Hesse, M. Sawicki, S. G. Ebbinghaus, and G. Schmidt, Yttrium Iron Garnet Thin Films with Very Low Damping Obtained by Recrystallization of Amorphous Material. *Sci. Rep.* **6**, 20827 (2016).

[68] M. C. Onbasli, A. Kehlberger, D. H. Kim, G. Jakob, M. Kläui, A. V. Chumak, B. Hillebrands, and C. A. Ross, Pulsed laser deposition of epitaxial yttrium iron garnet films with low Gilbert damping and bulk-like magnetization. *APL Mater.* **2**, 106102 (2014).

[69] C. Tang, M. Aldosary, Z. Jiang, H. Chang, B. Madon, K. Chan, and M. Wu, J. E. Garay, and J. Shi, Exquisite growth control and magnetic properties of yttrium iron garnet thin films. *Appl. Phys. Lett.* **108**, 102403 (2016).

[70] C. Dubs C, O. Surzhenko, R. Linke, A. Danilewsky, U. Brückner, and J. Dellith, Sub-micrometer yttrium iron garnet LPE films with low ferromagnetic resonance losses. *J. Phys. D: Appl. Phys.* **50**, 204005 (2017).

[71] N. Beaulieu, N. Kervarec, N. Thiery, O. Klein, V. Naletov, H. Hurdequint, G. de Loubens, J. B. Youssef, and N. Vukadinovic, Temperature dependence of magnetic properties of a ultrathin yttrium-iron garnet film grown by liquid phase epitaxy: Effect of a Pt overlayer. *IEEE Magn. Lett.* **9**, 2868700 (2018).

[72] R. Yu, K. He, Q. Liu, X. Gan, B. Miao, L. Sun, J. Du, H. Cai, X. Wu, M. Wu, and H. Ding,

Nonvolatile Electric-Field Control of Ferromagnetic Resonance and Spin Pumping in Pt/YIG at Room Temperature. *Adv. Electron. Mater.* **5**, 1800663 (2019).

[73] C. Dubs, O. Surzhenko, R. Thomas, J. Osten, T. Schneider, K. Lenz, J. Grenzer, R. Hübner, and E. Wendler, Low damping and microstructural perfection of sub-40nm-thin yttrium iron garnet films grown by liquid phase epitaxy. *Phys. Rev. Mater.* **4**, 024416 (2020).

[74] F. Bertaut and F. Forrat, Structure of ferrimagnetic rare-earth ferrites. *Compt. Rend.* **242**, 382 (1956).

[75] M. A. Gilleo and S Geller, Magnetic and Crystallographic Properties of Substituted Yttrium-Iron Garnet, $3Y_2O_3{\cdot}xM_2O_3{\cdot}(5-x)Fe_2O_3$. *Phys. Rev.* **110**, 73 (1958).

[76] G. Winkler, Magnetic Garnets. Friedr. Vieweg and Sohn Verlagsgesellschaft GmbH: Braunschweig (1981).

[77] H. A. Kramers, L'interaction entre les atomes magnétogènes dans un cristal paramagnétique. *Physica* **1**, 182 (1934).

[78] P. W. Anderson, Antiferromagnetism. Theory of superexchange interaction. *Phys. Rev.* **79**, 350 (1950).

[79] B. Lax and K. J. Button, Microwave Ferrites and Ferrimagnetics. McGraw-Hill, New York (1962).

[80] H. A. Algra and P. Hansen, Temperature dependence of the saturation magnetization of ion-implanted YIG films. *Appl. Phys. A* **29**, 83 (1982).

[81] D. Stancil and A. Prahakar, Spin Waves – Theory and Applications. Springer, New York (2009).

[82] M. Sparks, Ferromagnetic-Relaxation Theory. McGraw Hill, New York (1964).

[83] A. G. Gurevich and G. A. Melkov, Magnetization Oscillations. CRC Press, Boca Raton (2000).

[84] Y. Y. Song, S. Kalarickal, and C. E. Patton, Optimized pulsed laser deposited barium ferrite thin films with narrow ferromagnetic resonance linewidths. *J. Appl. Phys.* **94**, 5103 (2003).

[85] H. How, P. Shi, C. Vittoria, L. C. Kempel, and K. D. Trott, Single-crystal YIG phase shifter using composite stripline structure at X band. *J. Appl. Phys.* **87**, 4966 (2000).

[86] R. D. McMichael, and P. Krivosik, Classical model of extrinsic ferromagnetic resonance linewidth in ultrathin films. *IEEE Trans. on Magn.* **40**, 2-11 (2004).

[87] P. Krivosika, N. Mo, S. Kalarickalb, and C. E. Patton, Hamiltonian formalism for two magnon scattering microwave relaxation: Theory and applications. *J. Appl. Phys.* **101**, 083901 (2007).

[88] L. Lu, J. Young, M. Wu, C. Mathieu, M. Hadley, P. Krivosik, and N. Mo, Tuning of

magnetization relaxation in ferromagnetic thin films through seed layers. *Appl. Phys. Lett.* **100**, 022403 (2012).

[89] S. Kalarickal, P. Krivosik, J. Das, K. Kim, C. E. Patton, Microwave damping in polycrystalline Fe-Ti-N films: Physical mechanisms and correlations with composition and structure. *Phys. Rev. B* **77**, 054427 (2008).

[90] H. Makino, and Y. Hidaka, Determination of magnetic anisotropy constants for bubble garnet epitaxial films using field orientation dependence in ferromagnetic resonances. *Mater. Res. Bull.* **16**, 957 (1981).

[91] S. Bhatti, R. Sbiaa, A. Hirohata, H. Ohno, S. Fukami, and S. N. Piramanayagam, Spintronics based random access memory: a review. *Mater. Today* **20**, 530-548 (2017).

[92] S. Vélez, J. Schaab, M. S. Wörnle, M. Müller,E. Gradauskaite, P. Welter, C. Gutgsell, C. Nistor, C. L. Degen, M. Trassin, M. Fiebig, and P. Gambardella, High-speed domain wall racetracks in a magnetic insulator. *Nature Comm.* **10**, 4750 (2019).

[93] L. Soumah, N. Beaulieu, L. Qassym, C. Carrétéro, E. Jacquet, R. Lebourgeois, J. B. Youssef, P. Bortolotti,V. Cros, and A. Anane. Ultra-low damping insulating magnetic thin films get perpendicular. *Nat. Comm.* **9**, 1 (2018).

[94] Y. Lin, L. Jin, H. Zhang, Z. Zhong, Q. Yang, Y. Rao, M. Li, Bi-YIG ferrimagnetic insulator nanometer films with large perpendicular magnetic anisotropy and narrow ferromagnetic resonance linewidth. *J. Magn. Magn. Mater.* **496**, 165886 (2020).

[95] R. Skomski, P. Manchanda, P. Kumar, B. Balamurugan, A. Kashyap, and D. J. Sellmyer, Predicting the future of permanent-magnet materials. *IEEE Trans. Magn*. 49, 3215 (2013).

[96] Z. Chao, K. Zhu, S. C. De Freitas, J. Y. Chang, J. E. Davies, P. Eames, P. P. Freitas, O. Kazakova, C. Kim, C. W. Leung, and S. H. Liou, Magnetoresistive sensor development roadmap (non-recording applications). *IEEE Trans. Magn*. 55, 30 (2019).

[97] A. Silva, D. Leitao, M. Silva, P. Ribeiro, F. Franco, P. P. Freitas, and S. Cardoso, Advances in Spintronic Sensor Materials and Architectures. *Condensed Matter Physics National Conference* 18, (2019).

[98] T. Endoh, H. Koike, S. Ikeda, T. Hanyu, and Hideo Ohno, An overview of nonvolatile emerging memories—Spintronics for working memories. *IEEE J. Emerg. and Select. Topics in Circ. and Sys.* 6, 109 (2016).

[99] S. Parkin, and S. H. Yang, Memory on the racetrack. *Nat. Nanotech.* 10, 195 (2015).

[100] T. Chen, R. K. Dumas, A. Eklund, P. K. Muduli, A. Houshang, A. A. Awad, P. Dürrenfeld, B. G. Malm, A. Rusu, and J. Åkerman, Spin-torque and spin-Hall nano-oscillators. *Proceed. of the IEEE* 104, 1919 (2016).

[101] A. Hirohata, H. Sukegawa, H. Yanagihara, I. Žutić, T. Seki, S. Mizukami, and R. Swaminathan, Roadmap for emerging materials for spintronic device applications. *IEEE Trans. Magn*. 51, 1 (2015).

[102] D. Sander, S. O. Valenzuela, D. Makarov, C. H. Marrows, E. E. Fullerton, P. Fischer, J. McCord, P. Vavassori, S. Mangin, P. Pirro, B. Hillebrands, A. D. Kent, T. Jungwirth, O. Gutfleisch, C. G. Kim, and A. Berger, The 2017 magnetism roadmap. *J. Phys. D: Appl. Phys*. 50, 363001 (2017).

[103] J. Fu, M. Hua, X. Wen, M. Xue, S. Ding, M. Wang, P. Yu, S. Liu, J. Han, C. Wang, H. Du, Y. Yang, and J. Yang, Epitaxial growth of $Y_3Fe_5O_{12}$ thin films with perpendicular magnetic anisotropy. *Appl. Phys. Lett*. **110**, 202403 (2017).

[104] G. Li, H. Bai, J. Su, Z. Z. Zhu, Y. Zhang, and J. W. Cai, Tunable perpendicular magnetic anisotropy in epitaxial $Y_3Fe_5O_{12}$ films. *APL Mater*. **7**, 041104 (2019).

[105] C. Y. Guo, C. H. Wan, M. K. Zhao, H. Wu, C. Fang, Z. R. Yan, J. F. Feng, H. F. Liu, and X. F. Han, Spin-orbit torque switching in perpendicular $Y_3Fe_5O_{12}$/Pt bilayer. *Appl. Phys. Lett.* **114**, 192409 (2019).

[106] Y. M. Lu, Y. Choi, C. M. Ortega, X. M. Cheng, J. W. Cai, S. Y. Huang, L. Sun, and C. L. Chien, Pt magnetic polarization on $Y_3Fe_5O_{12}$ and magnetotransport characteristics. *Phys. Rev. Lett.* **110**, 147207 (2013).

[107] Y. T. Chen, S. Takahashi, H. Nakayama, M. Althammer, S. T. B. Goennenwein, E. Saitoh, G. E. W. Bauer, Theory of spin Hall magnetoresistance. *Phys. Rev. B* **87**, 144411 (2013).

[108] S. S. L. Zhang, G. Vignale, Nonlocal anomalous Hall effect. *Phys. Rev. Lett.* **116**, 136601 (2016).

[109] S. Meyer, R. Schlitz, S. Geprägs, M. Opel, H. Huebl, R. Gross, and S. T. Goennenwein, Anomalous Hall effect in YIG|Pt bilayers. *Appl. Phys. Lett.* **106**, 132402 (2015).

[110] C. O. Avci, A. Quindeau, C. F. Pai, M. Mann, L. Caretta, A. S. Tang, M. C. Onbasli, C. A. Ross, and G. S. Beach, Current-induced switching in a magnetic insulator. *Nat. Mater*. **16**, 309-314 (2017).

[111] C. Tang, P. Sellappan, Y. Liu, Y. Xu, J. E. Garay, and J. Shi, Anomalous Hall hysteresis in

$Tm_3Fe_5O_{12}$/Pt with strain-induced perpendicular magnetic anisotropy. *Phys. Rev. B* **94**, 140403 (2016).

[112] E. L. Jakubisova, S. Visnovsky, H. Chang, and M. Wu, Interface effects in nanometer-thick yttrium iron garnet films studied by magneto-optical spectroscopy. *Appl. Phys. Lett*., **108**, 082403 (2016).

[113] A. Mitra, O. Cespedes, Q. Ramasse, M. Ali, S. Marmion, M. Ward, R. M. D. Brydson, C. J. Kinane, J. F. K. Cooper, S. Langridge, and B. J. Hickey, Interfacial origin of the magnetisation suppression of thin film yttrium iron garnet. *Sci. Rep*., **7**, 1-8 (2017).

[114] J. F. K. Cooper, C. J. Kinane, S. Langridge, M. Ali, B. J. Hickey, T. Niizeki, K. Uchida, E. Saitoh, H. Ambaye, and A. Glavic, Unexpected structural and magnetic depth dependence of YIG thin films, *Phys. Rev. B* 96, 104404 (2017).

[115] J. M. Gomez-Perez, S. Vélez, L. McKenzie-Sell, M. Amado, J. Herrero-Martín, J. López-López, S. Blanco-Canosa, L. E. Hueso, A. Chuvilin, J. W. Robinson, and F. Casanova, Synthetic antiferromagnetic coupling between ultrathin insulating garnets. *Phys. Rev. Appl*. **10**, 044046 (2018).

[116] The polarized neutron reflectometry measurements on YIG thin films grown under the same conditions indicate an interfacial layer of about 5 nm thick. At room temperature, the magnetization across the thickness of this interfacial layer increases from about zero (at the interface with the substrate) to the bulk value of the YIG in the presence of a magnetic field of about 5 kOe. The detailed results will be reported in a separate paper.

[117] L. Lu, Z. Wang, G. Mead, C. Kaiser, Q. Leng, and M. Wu, Damping in free layers of tunnel magneto-resistance readers. *Appl. Phys. Lett.* **105**, 012405 (2014).

[118] D. Richardson, S. Katz, J. Wang, Y. K. Takahashi, K. Srinivasan, A. Kalitsov, K. Hono, A. Ajan, and M. Wu, Near-T_c Ferromagnetic Resonance and Damping in Fe Pt-Based Heat-Assisted Magnetic Recording Media, *Phys. Rev*. *Appl.* 10, 054046 (2018).

[119] K. M. Krishnan, Fundamentals and applications of magnetic materials. Oxford University Press (2016).

[120] W. H. Von Aulock, Handbook of Microwave Ferrite Materials. Academic (1965).

[121] Y. Ding, T. J. Klemmer, and T. M. Crawford, A coplanar waveguide permeameter for studying high-frequency properties of soft magnetic materials. *J. Appl. Phys*. **96**, 2969 (2004).

[122] H. T. Nembach, T. J. Silva, J. M. Shaw, M. L. Schneider, M. J. Carey, S. Maat, and J. R.

Childress, Perpendicular ferromagnetic resonance measurements of damping and Landé g-factor in sputtered $(Co_2Mn)_{1-x}Ge_x$ thin films. *Phys. Rev. B* **84**, 054424 (2011).

[123] D. Polder and J. Smit, Resonance phenomena in ferrites, *Rev. Mod. Phys.* **25**, 89 (1953).

[124] E. Schloemann, Low-frequency losses in ferrite microwave devices, unpublished.

[125] Sangita S. Kalarickal, Nan Mo, Pavol Krivosik, and Carl E. Patton, Ferromagnetic resonance linewidth mechanisms in polycrystalline ferrites: Role of grain-to-grain and grain-boundary two-magnon scattering processes, *Phys. Rev. B* **79**, 094427 (2009).

[126] A. J. Schellekens, L. Deen, D. Wang, J. T. Kohlhepp, H. J. M. Swagten, and B. Koopmans, Determining the Gilbert damping in perpendicularly magnetized Pt/Co/AlOx films, *Appl. Phys. Lett.* **102**, 082405 (2013).

[127] Y. Cui, B. Khodadadi, S. Schäfer, T. Mewes, J. Lu, and S. A. Wolf, Interfacial perpendicular magnetic anisotropy and damping parameter in ultra thin Co_2FeAl films, *Appl. Phys. Lett*. **102**, 162403 (2013).

[128] H. S. Song, K. D. Lee, J. W. Sohn, S. H Yang, S. S. P. Parkin, C. Y. You, and S. C. Shin, Observation of the intrinsic Gilbert damping constant in Co/Ni multilayers independent of the stack number with perpendicular anisotropy. *Appl. Phys. Lett.* 102, 102401 (2013).

[129] D. S. Wang, S. Y. Lai, T. Y. Lin, C. W. Chien, D. Ellsworth, L. W. Wang, J. W. Liao, L. Lu, Y. H. Wang, M. Wu, and C. H. Lai, High thermal stability and low Gilbert damping constant of CoFeB/MgO bilayer with perpendicular magnetic anisotropy by Al capping and rapid thermal annealing. *Appl. Phys. Lett*. **104**, 142402 (2014).

[130] C. N. Wu, C. C. Tseng, Y. T. Fanchiang, C. K. Cheng, K. Y. Lin, S. L. Yeh, S. R. Yang, C. T. Wu, T. Liu, M. Wu, and M. Hong, High-quality thulium iron garnet films with tunable perpendicular magnetic anisotropy by off-axis sputtering–correlation between magnetic properties and film strain. *Sci. Rep.* **8**, 11087 (2018).

[131] O. Ciubotariu, A. Semisalova, K. Lenz, and M. Albrecht, Strain-induced perpendicular magnetic anisotropy and Gilbert damping of $Tm_3Fe_5O_{12}$ thin films. *Sci. Rep*. **9**, 17474 (2019).

[132] J. J. Bauer, E. R. Rosenberg, S. Kundu, K. A. Mkhoyan, P. Quarterman, A. J. Grutter, B. J. Kirby, J. A. Borchers, and C. A. Ross, Dysprosium iron garnet thin films with perpendicular magnetic anisotropy on silicon. *Adv. Electron. Mater*. **6**, 1900820 (2020).

[133] E. R. Rosenberg, L. Beran, C. O. Avci, C. Zeledon, B. Song, C. Gonzalez-Fuentes, J. Mendil, P. Gambardella, M. Veis, C. Garcia, and G. S. Beach, Magnetism and spin transport in rare-

earth-rich epitaxial terbium and europium iron garnet films. *Phys. Rev. Mater*. **2**, 094405 (2018).

[134] P. Li, T. Liu, H. Chang, A. Kalitsov, W. Zhang, G. Csaba, W. Li, D. Richardson, A. DeMann, G. Rimal, and H. Dey, Spin–orbit torque-assisted switching in magnetic insulator thin films with perpendicular magnetic anisotropy. *Nat. Comm*. **7**, 1-8 (2016).

[135] I. M. Miron, K. Garello, G. Gaudin, P. J. Zermatten, M. V. Costache, S. Auffret, S. Bandiera, B. Rodmacq, A. Schuhl, and P. Gambardella, Perpendicular switching of a single ferromagnetic layer induced by in-plane current injection. *Nature*, **476**, 189-193 (2011).

[136] L. Liu, C. F. Pai, Y. Li, H. W. Tseng, D. C. Ralph, and R. A.Buhrman, Spin-torque switching with the giant spin Hall effect of tantalum. *Science* **336**, 555-558 (2012).

[137] J. E. Hirsch, Spin hall effect. *Phys. Rev. Lett*. **83**,1834 (1999).

[138] A. Hoffmann, Spin Hall effects in metals. *IEEE Trans. Magn*. **49**, 5172 (2013).

[139] S. A. Siddiqui, J. Han, J. T. Finley, C. A. Ross, and L. Liu, Current-induced domain wall motion in a compensated ferrimagnet. *Phys. Rev. Lett.* **121**, 057701 (2018).

[140] C. O. Avci, E. Rosenberg, L. Caretta, F. Büttner, M. Mann, C. Marcus, D. Bono, D., C. A. Ross, and G. S. Beach, Interface-driven chiral magnetism and current-driven domain walls in insulating magnetic garnets. *Nat. Nanotech.* **14**, 561-566 (2019).

[141] R. Wieser, E. Y. Vedmedenko, P. Weinberger, and R. Wiesendanger, Current-driven domain wall motion in cylindrical nanowires. *Phys. Rev. B* **82**, 144430 (2010).

[142] C. W. Sandweg, Y. Kajiwara, K. Ando, E. Saitoh, and B. Hillebrands, Enhancement of the spin pumping efficiency by spin wave mode selection. *Appl. Phys. Lett.* **97**, 252504 (2010).

[143] Z. Duan, C. T. Boone, X. Cheng, and I. N. Krivorotov, Spin-wave modes in permalloy/platinum wires and tuning of the mode damping by spin Hall current. *Phys. Rev. B* **90**, 024427 (2014).

[144] Q. Song, J. Mi, D. Zhao, T. Su1, W. Yuan, W. Xing, Y. Chen, T. Wang, T. Wu, X. H. Chen, X. C. Xie, C. Zhang, J. Shi and W. Han, Spin injection and inverse Edelstein effect in the surface states of topological Kondo insulator SmB_6, *Nat. Comm.* **7**, 13485 (2016).

[145] C. Tang, Q. Song, C.-Z. Chang, Y. Xu, Y. Ohnuma, M. Matsuo, Y. Liu, W. Yuan, Y. Yao, J. S. Moodera, S. Maekawa, W. Han and J. Shi, Dirac surface state–modulated spin dynamics in a ferrimagnetic insulator at room temperature. *Sci. Adv.* **4**, 8660 (2018).

[146] Y. T. Fanchiang, K. H. M. Chen, C. C. Tseng, C. C. Chen, C. K. Cheng, C. N. Wu, S. F. Lee, M. Hong, J. Kwo, Strongly exchange-coupled and surface-state-modulated magnetization

dynamics in Bi_2Se_3/YIG heterostructures. *Nat. Comm.* **9**, 223 (2018).

[147] H. Wang, J. Kally, C. Şahin, T. Liu, W. Yanez, E. J. Kamp, A. Richardella, M. Wu, M. E. Flatté, and Nitin Samarth, Fermi Level Dependent Spin Pumping from a Magnetic Insulator into a Topological Insulator. *Phys. Rev. Res.* **1**, 012014(R) (2019).

[148] H. Song, J. Yao, Y. Ding, Y. Gu, Y. Deng, M.-H. Lu, H. Lu, and Y.-F. Chen, Thermal Stability Enhancement in Epitaxial Alpha Tin Films by Strain Engineering. *Adv. Eng. Mater.* **21**, 1900410 (2019).

[149] I. Madarevic, U. Thupakula, G. Lippertz, N. Claessens, P.-C. Lin, H. Bana, S. Gonzalez, G. D. Santo, L. Petaccia, M. N. Nair, L. M. C. Pereira, C. V. Haesendonck, and M. J. Van Bael. Structural and electronic properties of the pure and stable elemental 3D topological Dirac semimetal α-Sn. *APL Mater.* **8**, 031114 (2020).

[150] C.-Z. Li, L.-X. Wang, H. Liu, J. Wang, Z.-M. Liao, and D.-P. Yu, Giant negative magnetoresistance induced by the chiral anomaly in individual Cd_3As_2 nanowires. *Nat. Comm.* **6**, 10137 (2015).

[151] H. Li, H. He, H.-Z. Lu, H. Zhang, H. Liu, R. Ma, Z. Fan, S.-Q. Shen, J. Wang, Negative magnetoresistance in Dirac semimetal Cd_3As_2. *Nat. Comm.* **7**, 10301 (2016).

[152] C. Zhang, E. Zhang, W. Wang, Y. Liu, Z.-G. Chen, S. Lu, S. Liang, J. Cao, X. Yuan, L. Tang, Q. Li, C. Zhou, T. Gu, Y. Wu, J. Zou, F. Xiu, Room-temperature chiral charge pumping in Dirac semimetals. *Nat. Comm.* **8**, 13741 (2017).

[153] Y. Zhang, C. Wang, L. Yu, G. Liu, A. Liang, J. Huang, S. Nie, X. Sun, Y. Zhang, B. Shen, J. Liu, H. Weng, L. Zhao, G. Chen, X. Jia, C. Hu, Y. Ding, W. Zhao, Q. Gao, C. Li, S. He, L. Zhao, F. Zhang, S. Zhang, F. Yang, Z. Wang, Q. Peng, X. Dai, Z. Fang, Z. Xu, C. Chen, and X. J. Zhou, Electronic evidence of temperature-induced Lifshitz transition and topological nature in $ZrTe_5$. *Nat. Comm.* **8**, 15512 (2017).

[154] H. L. Wang, C. H. Du, Y. Pu, R. Adur, P. C. Hammel, and F. Y. Yang, Scaling of spin Hall angle in 3d, 4d, and 5d metals from $Y_3Fe_5O_{12}$/metal spin pumping. *Phys. Rev. Lett.* **112**, 197201 (2014).

[155] L. A. Wray, S.-Y. Xu, Y. Xia, D. Hsieh, A. V. Fedorov, Y. S. Hor, R. J. Cava, A. Bansil, H. Lin, and M. Z. Hasan, A topological insulator surface under strong Coulomb, magnetic and disorder perturbations. *Nat. Phys.* **7**, 32 (2011).

[156] J. Zhang, J. P. Velev, X. Dang, E. Y. Tsymbal, Band structure and spin texture of Bi_2Se_3 3*d*

ferromagnetic metal interface. *Phys. Rev. B* **94**, 014435 (2016).

[157] J. M. Marmolejo-Tejada, K. Dolui, P. Lazic, P.-H. Chang, S. Smidstrup, D. Stradi, K. Stokbro, B. K. Nikolic, Proximity band structure and spin textures on both sides of topological-insulator/ferromagnetic-metal interface and their charge transport probes. *Nano Lett.* **17**, 5626 (2017).

[158] Y. T. Hsu, K. Park, E. A. Kim, Hybridization-induced interface states in a topological insulator-magnetic metal heterostructure. *Phys. Rev. B* **96**, 235433 (2017).

[159] T. G. Pedersen, P. Modak, K. Pedersen, N. E. Christensen, M. M. Kjeldsen and A. N. Larsen, Ab initio calculation of electronic and optical properties of metallic tin. *J. Phys.: Cond. Mater.* **21**, 11 (2019).

[160] B. Kardasza, O. Mosendz, and B. Heinrich, Z. Liu and M. Freeman, Spin current studies in by Fe/Ag, Au/Fe by ferromagnetic resonance and time-resolved magneto-optics. *J. Appl. Phys.* **103**, 07C509 (2008).

[161] J. C. Rojas Sánchez, L. Vila, G. Desfonds, S. Gambarelli, J. P. Attané, J. M. De Teresa, C. Magén, and A. Fert, Spin-to-charge conversion using Rashba coupling at the interface between non-magnetic materials. *Nat. Comm.* **4**, 2944 (2013).

[162] J. M. Shaw, T. J. Silva, M. L. Schneider, and R. D. McMichael, Spin dynamics and mode structure in nanomagnet arrays: Effects of size and thickness on linewidth and damping. *Phys. Rev. B* **79**, 184404 (2009).

[163] T. J. Silva, C. S. Lee, T. M. Crawford, and C. T. Rogers, Inductive measurement of ultrafast magnetization dynamics in thin-film Permalloy. *J. Appl. Phys.* **85**, 7849 (1999).

[164] Y. Xu, B. Yan, H.-J. Zhang, J. Wang, G. Xu, P. Tang, W. Duan, and S.-C. Zhang, Large-Gap Quantum Spin Hall Insulators in Tin Films. *Phys. Rev. Lett.* **111**, 136804 (2013).

[165] C.-Z. Xu, Y.-H. Chan, P. Chen, X. Wang, D. Flötotto, J. A. Hlevyack, G. Bian, S.-K. Mo, M.-Y. Chou, and T.-C. Chiang, Gapped electronic structure of epitaxial stanene on InSb(111). *Phys. Rev. B* **97**, 035122 (2018).

[166] G. J. de Coster, P. A. Folkes, P. J. Taylor, and O. A. Vail, Effects of orientation and strain on the topological characteristics of CdTe/α-Sn quantum wells. *Phys. Rev. B* **98**, 115153 (2018).

[167] V. A. Rogalev, F. Reis, F. Adler, M. Bauernfeind, J. Erhardt, A. Kowalewski, M. R. Scholz, L. Dudy, L. B. Duffy, T. Hesjedal, M. Hoesch, G. Bihlmayer, J. Schäfer, and R. Claessen, Tailoring the topological surface state in ultrathin α-Sn(111) films. *Phys. Rev. B* **100**, 245144

(2019).

[168] M. Kargarian, M. Randeria, and Y.-M. Lu, Are the surface Fermi arcs in Dirac semimetals topologically protected? *Proc. Nat. Acad. Sci.* **113**, 8648-8652 (2016).

[169] I. M. Miron, G. Gaudin, S. Auffret, B. Rodmacq, A. Schuhl, S. Pizzini, J. Vogel, and P. Gambardella, Current-driven spin torque induced by the Rashba effect in a ferromagnetic metal layer. *Nat. Mater.* **9**, 230-234 (2010).

[170] L. Liu, O. J. Lee, T. J. Gudmundsen, D. C. Ralph, and R. A. Buhrman, Current-Induced Switching of Perpendicularly Magnetized Magnetic Layers Using Spin Torque from the Spin Hall Effect. *Phys. Rev. Lett.* **109**, 096602 (2012).

[171] S. Emori, U. Bauer, S.-M. Ahn, E. Martinez, and G. S. D. Beach, Current-driven dynamics of chiral ferromagnetic domain walls. *Nat. Mater*. **12**, 611-616 (2013).

[172] Z. Duan, A. Smith, L. Yang, B. Youngblood, J. Lindner, V. E. Demidov, S. O. Demokritov, and I. N. Krivorotov, Nanowire spin torque oscillator driven by spin orbit torques. *Nat. Comm*. **5**, 5616 (2014).

[173] Y. Fan, P. Upadhyaya, X. Kou, M. Lang, S. Takei, Z. Wang, J. Tang, L. He, L.-T. Chang, M. Montazeri, G. Yu, W. Jiang, T. Nie, R. N. Schwartz, Y. Tserkovnyak, and K. L. Wang, Magnetization switching through giant spin–orbit torque in a magnetically doped topological insulator heterostructure. *Nat. Mater.* **13**, 699-704 (2014).

[174] J. Han, A. Richardella, S. A. Siddiqui, J. Finley, N. Samarth, and L. Liu, Room-temperature spin-orbit torque switching induced by a topological insulator. *Phys. Rev. Lett.* **119**, 077702 (2017).

[175] Y. Wang, D. Zhu, Y. Wu, Y. Yang, J. Yu, R. Ramaswamy, R. Mishra, S. Shi, M. Elyasi, K.-L. Teo, Y. Wu, and H. Yang, Room temperature magnetization switching in topological insulator-ferromagnet heterostructures by spin-orbit torques. *Nat. Comm*. **8**, 1364 (2017).

[176] K. Yasuda, A. Tsukazaki, R. Yoshimi, K. Kondou, K. S. Takahashi, Y. Otani, M. Kawasaki, and Y. Tokura, Current-nonlinear Hall effect and spin-orbit torque magnetization switching in a magnetic topological insulator. *Phys. Rev. Lett.* **119**, 137204 (2017).

[177] Y. Li, Q. Ma, S. X. Huang, and C. L. Chien, Thin films of topological Kondo insulator candidate SmB_6: Strong spin-orbit torque without exclusive surface conduction. *Sci. Adv*. **4**, 8294 (2018).

[178] M. Dc, R. Grassi, J.-Y. Chen, M. Jamali, D. R. Hickey, D. Zhang, Z. Zhao, H. Li, P. Quarterman,

Y. Lv, M. Li, A. Manchon, K. A. Mkhoyan, T. Low, and J.-P. Wang, Room-temperature high spin–orbit torque due to quantum confinement in sputtered $Bi_xSe_{(1-x)}$ films. *Nat. Mater*. **17**, 800-807 (2018).

[179] N. H. D. Khang, Y. Ueda, and P. N. Hai, A conductive topological insulator with large spin Hall effect for ultralow power spin–orbit torque switching. *Nat. Mater*. **17**, 808-813 (2018).

[180] P. Li, J. Kally, S. S.-L. Zhang, T. Pillsbury, J. Ding, G. Csaba, J. Ding, J.S. Jiang, Y. Liu, R. Sinclair, C. Bi, A. DeMann, G. Rimal, W. Zhang, S. B. Field, J.Tang, W. Wang, O. G. Heinonen, V. Novosad, A.Hoffmann, N. Samarth, and M. Wu, Magnetization switching using topological surface states. *Sci. Adv*. **5**, eaaw3415 (2019).

[181] https://www.mtixtl.com/Si-U-c-101005S1.aspx

[182] O. Vail, P. Taylor, P. Folkes, B. Nichols, B. Haidet, K. Mukherjee, and G. de Coster, Growth and Magnetotransport in Thin-Film α-Sn on CdTe. *physica status solidi (b)* **257**, 1800513 (2020).

[183] M. N. Ali, J. Xiong, S. Flynn, J. Tao, Q. D. Gibson, L. M. Schoop, T. Liang, N. Haldolaarachchige, M. Hirschberger, N. P. Ong, and R. J. Cava, Large, Non-Saturating Magnetoresistance in WTe_2. *Nature* **514**, 205 (2014).

[184] P. L. Cai, J. Hu, L. P. He, J. Pan, X. C. Hong, Z. Zhang, J. Zhang, J. Wei, Z. Q. Mao, and S. Y. Li, Drastic Pressure Effect on the Extremely Large Magnetoresistance in WTe_2. *Phys. Rev. Lett*. **115**, 057202 (2015)

[185] P. He, C.-H. Hsu, S. Shi, K. Cai, J. Wang, Q. Wang, G. Eda, H. Lin, V. M. Pereira, and H. Yang, Nonlinear magnetotransport shaped by Fermi surface topology and convexity. *Nat. Comm*. **10**, 1290 (2019).

[186] L. P. He, X. C. Hong, J. K. Dong, J. Pan, Z. Zhang, J. Zhang, and S. Y. Li, Quantum Transport Evidence for the Three-Dimensional Dirac Semimetal Phase in Cd_3As_2. *Phys. Rev. Lett*. **113**, 246402 (2014).

[187] Y. Zhao, H. Liu, C. Zhang, H. Wang, J. Wang, Z. Lin, Y. Xing, H. Lu, J. Liu, Y. Wang, S. M. Brombosz, Z. Xiao, S. Jia, X. C. Xie, and J. Wang, Anisotropic Fermi Surface and Quantum Limit Transport in High Mobility Three-Dimensional Dirac Semimetal Cd_3As_2. *Phys. Rev. X* **5**, 031037 (2015).

[188] J. Cao, S. Liang, C. Zhang, Y. Liu, J. Huang, Z. Jin, Z.-G. Chen, Z. Wang, Q. Wang, J. Zhao, S. Li, X. Dai, J. Zou, Z. Xia, L. Li, and F. Xiu, Landau level splitting in Cd_3As_2 under high

magnetic fields. *Nat. Comm*. **6**, 7779 (2015).

[189] A. Narayanan, M. D. Watson, S. F. Blake, N. Bruyant, L. Drigo, Y. L. Chen, D. Prabhakaran, B. Yan, C. Felser, T. Kong, P. C. Canfield, and A. I. Coldea, Linear Magnetoresistance Caused by Mobility Fluctuations in n-Doped Cd_3As_2. *Phys. Rev. Lett*. **114**, 117201 (2015).

[190] N. Bansal, Y. S. Kim, M. Brahlek, and E. Edrey, S. Oh, Thickness-Independent Transport Channels in Topological Insulator Bi_2Se_3 Thin Films. *Phys. Rev. Lett*. **109**, 116804 (2012).

[191] Q. Barbedienne, J. Varignon, N. Reyren, A. Marty, C. Vergnaud, M. Jamet, C. G.-Carbonell, A. Lemaître, P. L. Fèvre, F. Bertran, A. T.-Ibrahimi, H. Jaffrès, J.-M. George, and A. Fert, Angular-resolved photoemission electron spectroscopy and transport studies of the elemental topological insulator α-Sn. *Phys. Rev. B* **98**, 195445 (2018).

[192] S. Dushenko, M. Hokazono, K. Nakamura, Y. Ando, T. Shinjo, and M. Shiraishi, Tunable inverse spin Hall effect in nanometer-thick platinum films by ionic gating. *Nat. Comm.* **9**, 3118 (2018).

[193] L. Kipgen, H. Fulara, M. Raju, and S. Chaudhary, In-plane magnetic anisotropy and coercive field dependence upon thickness of CoFeB. *J. Magn. Magn. Mater.* **324**, 3118 (2012).

[194] B. Cui, C. Song, Y. Y. Wang, W. S. Yan, F. Zeng, and F. Pan, Tuning of uniaxial magnetic anisotropy in amorphous CoFeB films. *J. Phys. Condens. Matter* **25**, 106003 (2013).

[195] X. Y. Qiao, B. M. Wang, Z. H. Tang, Y. Shen, H. L. Yang, J. L. Wang, Q. F. Zhan, S. N. Mao, X. H. Xu, and R. W. Li, Tuning magnetic anisotropy of amorphous CoFeB film by depositing on convex flexible substrates. *AIP Adv.* **6**, 056106 (2016).

[196] X. C. Wen, B. M. Wang, P. Sheng, S. Hu, H. L. Yang, K. Pei, Q. F. Zhan, W. X. Xia, H. Xu, and R. W. Li, Determination of stress-coefficient of magnetoelastic anisotropy in flexible amorphous CoFeB film by anisotropic magnetoresistance. *Appl. Phys. Lett.* **111**, 142403 (2017).

[197] A. Aharoni, Demagnetizing factors for rectangular ferromagnetic prisms. *J. Appl. Phys.* **83**, 3432 (1998).

[198] D. M. Lattery, D. Zhang, J. Zhu, X.Hang, J.-P. Wang, and X. Wang, Low Gilbert damping constant in perpendicularly magnetized W/CoFeB/MgO films with high thermal stability. *Sci. Rep.* **8**, 13395 (2018).

[199] Object Oriented MicroMagnetic Framework (OOMMF): https://math.nist.gov/oommf/

[200] S.-h. C. Baek, V. P. Amin, Y.-W. Oh, G. Go, S.-J. Lee, G.-H. Lee, K.-J. Kim, M. D. Stiles, B.-

G. Park, and K.-J. Lee, Spin currents and spin–orbit torques in ferromagnetic trilayers. *Nat. Mater.* **17**, 509-513 (2018).

[201] C.-F. Pai, L. Liu, Y. Li, H. W. Tseng, D. C. Ralph, and R. A. Buhrman, Spin transfer torque devices utilizing the giant spin Hall effect of tungsten. *Appl. Phys. Lett*. **101**, 122404 (2012).

[202] L. Liu, T. Moriyama, D. C. Ralph, and R. A. Buhrman, Spin-Torque Ferromagnetic Resonance Induced by the Spin Hall Effect. *Phys. Rev. Lett*. **106**, 036601 (2011).

[203] D. R. Sahu, S.-Y. Lin, and J.-L. Huang, ZnO/Ag/ZnO multilayer films for the application of a very low resistance transparent electrode. *Appl. Surf. Sci*. **252** 7509-7514 (2006).

[204] J. Z. Sun, Spin-current interaction with a monodomain magnetic body: A model study. *Phys. Rev. B* **62**, 570 (2000).

[205] S. Fukami, T. Anekawa, C. Zhang, and H. Ohno, A spin–orbit torque switching scheme with collinear magnetic easy axis and current configuration. *Nat. Nanotech*. **11**, 621-625 (2016).

[206] W. T. Coffey, and Y. P. Kalmykov, Thermal fluctuations of magnetic nanoparticles: Fifty years after Brown. *J. Appl. Phys.* **112**, 121301 (2012).

[207] Z. Diao, Z. Li, S. Wang, Y. Ding, A. Panchula, E. Chen, L.-C. Wang, and Y. Huai, Spin-transfer torque switching in magnetic tunnel junctions and spin-transfer torque random access memory. *J. Phys.: Cond. Mat.* **19**, 16 (2007).

[208] J.-C. Rojas-Sánchez, and A. Fert, Compared Efficiencies of Conversions between Charge and Spin Current by Spin-Orbit Interactions in Two- and Three-Dimensional Systems. *Phys. Rev. Appl.* **11**, 054049 (2019).

[209] M. Mogi, M. Kawamura, R. Yoshimi, A. Tsukazaki, Y. Kozuka, N. Shirakawa, K. S. Takahashi, M. Kawasaki, and Y. Tokura, A magnetic heterostructure of topological insulators as a candidate for an axion insulator. *Nat. Mater.* **16**, 516-521 (2017).

[210] M. Mogi, M. Kawamura, A. Tsukazaki, R. Yoshimi, K. S. Takahashi, M. Kawasaki, and Y. Tokura, Tailoring tricolor structure of magnetic topological insulator for robust axion insulator. *Sci. Adv.* **3**, 1669 (2017).

[211] D. Xiao, J. Jiang, J. H. Shin, W. Wang, F. Wang, Y. F. Zhao, C. Liu, W. Wu, M. H. W. Chan, N. Samarth, and C. Z. Chang, Realization of the Axion Insulator State in Quantum Anomalous Hall Sandwich Heterostructures. *Phys. Rev. Lett.* 120, 056801 (2018).

[212] P. Wei, F. Katmis, B. A. Assaf, H. Steinberg, P. J. Herrero, D. Heiman, and J. S. Moodera, Exchange-Coupling-Induced Symmetry Breaking in Topological Insulators. *Phys. Rev.*

Lett. **110**, 186807 (2013).

[213] C. Tang, C. Z. Chang, G. Zhao, Y. Liu, Z. Jiang, C. X. Liu, M. R. McCartney, D. J. Smith, T. Chen, J. S. Moodera, and J. Shi, Above 400-K robust perpendicular ferromagnetic phase in a topological insulator. *Sci. Adv.* **3**, 1700307 (2017).

[214] M. Mogi, T. Nakajima, V. Ukleev, A. Tsukazaki, R. Yoshimi, M. Kawamura, K. S. Takahashi, T. Hanashima, K. Kakurai, T. Arima, M. Kawasaki, and Y. Tokura, Large anomalous Hall effect in topological insulators with proximitized ferromagnetic insulators, *Phys. Rev. Lett.* **123**, 016804 (2019).

[215] J. S. Lee, A. Richardella, R. D. F., C.-X. Liu, W. Zhao, and N. Samarth, Engineering the breaking of time-reversal symmetry in gate-tunable hybrid ferromagnet/topological insulator heterostructures, *npj Quant. Mater.* **3**, 51 (2018).

[216] K. Yasuda, R. Wakatsuki, T. Morimoto, R. Yoshimi, A. Tsukazaki, K. S. Takahashi, M. Ezawa, M. Kawasaki, N. Nagaosa, and Y. Tokura, Geometric Hall Effects in Topological Insulator Heterostructures. *Nat. Phys.* **12**, 555-559 (2016).

[217] J. Jiang, D. Xiao, F. Wang, J.-H. Shin, D. Andreoli, J. Zhang, R. Xiao, Y.-F. Zhao, M. Kayyalha, Ling Zhang, K. Wang, J. Zang, C. Liu, N. Samarth, M. H. W. Chan, and Cui-Zu Chang, Crossover of Quantum Anomalous Hall to Topological Hall Effect in Magnetic Topological Insulator Sandwich Heterostructures. *Nat. Mater.* **19**, 732–737 (2020).

[218] N. Nagaosa, J. Sinova, S. Onoda, A. H. MacDonald, and N. P. Ong, Anomalous Hall effect. *Rev. Mod. Phys.* **82**, 1539 (2010).

[219] J. Matsuno, N. Ogawa, K. Yasuda, F. Kagawa, W. Koshibae, N. Nagaosa, Y. Tokura, and M. Kawasaki, Interface-driven topological Hall effect in $SrRuO_3$-$SrIrO_3$ bilayer. *Sci. Adv.* **2**, e1600304 (2016).

[220] Q. He, G. Yin, A. J. Grutter, L. Pan, X. Che, G. Yu, D. A. Gilbert, S. M. Disseler, Y. Liu, P. Shafer, B. Zhang, Y. Wu, B. J. Kirby, E. Arenholz, R. K. Lake, X. Han, and K. L. Wang, Exchange-biasing topological charges by antiferromagnetism, *Nat. Comm.* **9**, 2767 (2018).

[221] L. Vistoli, W. Wang, A. Sander, Q. Zhu, B. Casals, R. Cichelero, A. Barthélémy, S. Fusil, G. Herranz, S. Valencia, R. Abrudan, E. Weschke, K. Nakazawa, H. Kohno, J. Santamaria, W. Wu, V. Garcia, and M. Bibes, Giant topological Hall effect in correlated oxide thin films. *Nat. Phys.* **15**, 67-72 (2019).

[222] Q. Shao, Y. Liu, G. Yu, S. Kim, X. Che, C. Tang, Q. He, Y. Tserkovnyak, J. Shi, and K. L.

Wang, Topological Hall effect at above room temperature in heterostructures composed of a magnetic insulator and a heavy metal. *Nat. Elect.* **2**, 182-186 (2019).

[223] A. S. Ahmed, A. J. Lee, N. Bagués, B. A. McCullian, A. M. A. Thabt, A. Perrine, J. R. Rowland, M. Randeria, P. C. Hammel, D. W. McComb, and F. Yang, Spin-Hall Topological Hall Effect in Highly Tunable Pt/Ferrimagnetic-Insulator Bilayers. *Nano Lett.* **8**, 5683-5688 (2019).

[224] K. M. Fijalkowski, M. Hartl, M. Winnerlein, P. Mandal, S. Schreyeck, K. Brunner, C. Gould, and L. W. Molenkamp, Coexistence of surface and bulk ferromagnetism mimics skyrmion Hall effect in a topological insulator. *Phys. Rev. X* **10**, 011012 (2020).

[225] M. Wu, M-Type Barium Hexagonal Ferrite Films, in *Advanced Magnetic Materials Edited by L. Malkinski* (InTech, 2012).

[226] G. T. Rado, and H. Suhl, *Magnetism Volume I* (Academic Press, 1963).

[227] P. Bruno, V. K. Dugaev, and M. Taillefumier, Topological Hall Effect and Berry Phase in Magnetic Nanostructures. *Phys. Rev. Lett*. **93**, 096806 (2004).

[228] M. Lang, M. Montazeri, M. C. Onbasli, X. Kou, Y. Fan, P. Upadhyaya, K. Yao, F. Liu, Y. Jiang, W. Jiang, K. L. Wong, G. Yu, J. Tang, T. Nie, L. He, R. N. Schwartz, Y. Wang, C. A. Ross, and Kang L. Wang, Proximity induced high-temperature magnetic order in topological insulator-ferrimagnetic insulator heterostructure. *Nano Lett*. **14**, 3459-3465 (2014).

[229] F. Katmis, V. Lauter, F. S. Nogueira, B. A. Assaf, M. E. Jamer, P. Wei, B. Satpati, J. W. Freeland, I. Eremin, D. Heiman, P. Jarillo-Herrero, and J. S. Moodera, A high-temperature ferromagnetic topological insulating phase by proximity coupling. *Nature* **533**, 513 (2016).

[230] S. Banerjee, J. Rowland, O. Erten, and M. Randeria, Enhanced Stability of Skyrmions in Two-Dimensional Chiral Magnets with Rashba Spin-Orbit Coupling. *Phys. Rev. X* **4**, 031045 (2014).

[231] A. Fert, N. Reyren, and Vincent Cros, Magnetic skyrmions: advances in physics and potential applications. *Nat. Rev. Mater.* **2**, 17031 (2017).

[232] S. Schlotter, P. Agrawal, and G. S. D. Beach, Temperature dependence of the Dzyaloshinskii-Moriya interaction in Pt/Co/Cu thin film heterostructures. *Appl. Phys. Lett.* **113**, 092402 (2018).

[233] Y. Liu, D. J. Sellmyer, and D. Shindo, *Handbook of Advanced Magnetic Materials, Vol 1. Nanostructural Effects* (Springer, 2016).

[234] T. Garel, and S. Doniach, Phase transitions with spontaneous modulation-the dipolar Ising ferromagnet. *Phys. Rev. B* **26**, 325 (1982).

[235] Steven S.-L. Zhang, C. Phatak, A.-K Petford-Long, and O.-G Heinonen, Tailoring magnetic

skyrmions by geometric confinement of magnetic structures. *Appl. Phys. Lett*. **111**, 242405 (2017).

[236] W. Jiang, P. Upadhyaya, W. Zhang, G. Yu, M. B. Jungfleisch, F. Y. Fradi, J. E. Pearson, Y. Tserkovnyak, K. L. Wang, O. Heinonen, S. G. E. te Velthuis, and A. Hoffmann, Blowing magnetic skyrmion bubbles. *Science*, **349**, 283-286 (2015).

[237] S. Woo, K. M. Song, H.-S. Han, M. -S. Jung, M. -Y. Im, K.-S. Lee, K. S. Song, P. Fischer, J. -I. Hong, J. W. Choi, B. -C. Min, H. C. Koo, and J. Chang. Spin-orbit torque-driven skyrmion dynamics revealed by time-resolved X-ray microscopy. *Nat. Commun.* **8**, 15573 (2017).

[238] P. He, S. S.-L. Zhang, D. Zhu, S. Shi, O. G. Heinonen, G. Vignale, and H. Yang, Nonlinear Planar Hall Effect, *Phys. Rev. Lett.* **123**, 016801 (2019).

[239] S. Rohart, and A. Thiaville, Skyrmion confinement in ultrathin film nanostructures in the presence of Dzyaloshinskii-Moriya interaction. *Phys. Rev. B* **88**, 184422 (2013).

[240] O. Boulle, J. Vogel, H. Yang, S. Pizzini, D. de S. Chaves, A. Locatelli, T. O. Menteş, A. Sala, L. D. Buda-Prejbeanu, O. Klein, M. Belmeguenai, Y. Roussigné, A. Stashkevich, S. M. Chérif, L. Aballe, M. Foerster, M. Chshiev, S. Auffret, I. M. Miron, and G. Gaudin, Room-temperature chiral magnetic skyrmions in ultrathin magnetic nanostructures. *Nat. Nano.* **11**, 449-454 (2016).

[241] S. Woo, K. Litzius, B. Krüger, M. Y. Im, L. Caretta, K. Richter, M. Mann, A. Krone, R. M. Reeve, M. Weigand, P. Agrawal, I. Lemesh, M. A. Mawass, P. Fischer, M. Kläui, and G. S. D. Beach, Observation of room-temperature magnetic skyrmions and their current-driven dynamics in ultrathin metallic ferromagnets. *Nat. Mater.* **15**, 501-506 (2016).

[242] C. M. Luchaire, C. Moutafis, N. Reyren, J. Sampaio, C. A. F. Vaz, N. Van Horne, K. Bouzehouane, K. Garcia, C. Deranlot, P. Warnicke, P. Wohlhüter, J.-M. George, M. Weigand, J. Raabe, V. Cros, and A. Fert, Additive interfacial chiral interaction in multilayers for stabilization of small individual skyrmions at room temperature. *Nat. Nano.* **11**, 444-448 (2016).

[243] S. Jaiswal, K. Litzius, I. Lemesh, F. Büttner, S. Finizio, J. Raabe, M. Weigand, K. Lee, J. Langer, B. Ocker, G. Jakob, G. S. D. Beach, and M. Kläui, Investigation of the Dzyaloshinskii-Moriya interaction and room temperature skyrmions in W/CoFeB/MgO thin films and microwires. *Appl. Phys. Lett*. **111**, 022409 (2017).

[244] X. Z. Yu, Y. Onose, N. Kanazawa, J. H. Park, J. H. Han, Y. Matsui, N. Nagaosa, and Y. Tokura, Real-space observation of a two-dimensional skyrmion crystal. *Nature* **465**, 901-904 (2010).

[245] A. Soumyanarayanan, M. Raju, A. L. Gonzalez Oyarce, Anthony K. C. Tan, Mi-Young Im, A. P. Petrović, Pin Ho, K. H. Khoo, M. Tran, C. K. Gan, F. Ernult, and C. Panagopoulos, Tunable room-temperature magnetic skyrmions in Ir/Fe/Co/Pt multilayers. *Nat. Mater.* **16**, 898-904 (2017).

[246] X. Zuo, P. Shi, S. A. Oliver, and C. Vittoria, Single crystal hexaferrite phase shifter at K_a band. *J. Appl. Phys*. **91**, 7622 (2002).